THESIS FOR THE DEGREE OF DOCTOR OF PHILOSOPHY

Development of high performance aluminium alloys tailored for powder bed fusion-laser beam

BHARAT MEHTA

Department of Industrial and Materials Science

CHALMERS UNIVERSITY OF TECHNOLOGY

Gothenburg, Sweden 2023

Development of high performance aluminium alloys tailored for powder bed fusion-laser beam

BHARAT MEHTA
ISBN 978-91-7905-909-5

Doktorsavhandlingar vid Chalmers tekniska högskola
Ny serie nr 5375
ISSN 0346-718X

Department of Industrial and Materials Science
Chalmers University of Technology
SE-412 96 Gothenburg
Sweden
Telephone + 46 (0)31-772 1000

Cover: Effect of different zirconium precipitates on general grain structure of aluminium shown with two electron backscatter images. Both materials produced by powder bed fusion-laser beam. More information can be found on page 29 of the thesis

Printed by Chalmers digitaltryck
Gothenburg, Sweden 2023

Development of high performance aluminium alloys tailored for powder bed fusion-laser beam

BHARAT MEHTA

Department of Industrial and Materials Science
Chalmers University of Technology

ABSTRACT

The powder bed fusion-laser beam (PBF-LB) process has lately been regarded as a top choice for creating complicated structures which are not possible via conventional manufacturing. Nevertheless, the pace of alloys for PBF-LB has been slower. Commercially available alloys are derived from cast/ wrought counterparts with limited knowledge of their suitability to PBF-LB. To fully exploit the inherent advantages of PBF-LB process, there is thus a growing need to develop alloy compositions with help from computational tools. This research work focused on the development of aluminium alloy systems tailored for the PBF-LB process. Leveraging the possibilities and limitations of PBF-LB process and with the help of CALPHAD tools, two types of alloying approaches were investigated namely in-situ alloying and ex-situ mixing. The key alloy design objectives were to avoid solidification cracking while attaining higher solid solubilities combined with a refined microstructure. The mechanical property objective was >450 MPa strength and high-temperature strength up to 573 K combined with general corrosion resistance.

Al-Mn-Cr-Zr based alloy system resulting from this thesis study include several variants with different amounts of alloying elements. Gas-atomised powder was used, and fully dense samples were processed using optimised PBF-LB process. This was followed by post-processing heat treatments to optimise mechanical properties. This created an alloy system with mechanical properties including yield strengths 250-500 MPa, elongation to failure 5-25% and bending fatigue 140-200 MPa. In as-printed state, strengthening was caused by a combination of solid solution strengthening and grain size effect. The strengthening from precipitates was observed after direct ageing heat treatments. The microstructure was characterised by SEM, TEM and in-situ synchrotron measurements. Long-term isothermal testing at 623 K for >1000 h showed a superior performance (-17 HV or 12% drop). High-temperature tensile testing at 573 K showed yield strengths >150 MPa, surpassing most commercially available Al-alloys.

These novel high performance alloys expand the available material performance envelope and create an edge over currently available systems while completely avoiding critical or rare earth elements. Such tailored alloy systems are shown to better utilise PBF-LB processing conditions to enhance material properties thus increasing the potential applications.

Keywords: Additive manufacturing; Powder bed fusion-laser beam; Alloy design; Aluminium alloys; Precipitation kinetics; Heat treatments; Integrated computational materials engineering

Preface

The work in this doctoral thesis was conducted at the Department of Industrial and Materials Science at Chalmers University of Technology, Göteborg, Sweden from June 2019 to August 2023. The work was conducted within the framework of Centre for Additive Manufacturing – Metal (CAM^2) supported by the Swedish Governmental Agency of Innovation Systems (VINNOVA) grant number 2016-05175, ALL-Light a part of SIP LIGHTer supported by VINNOVA grant number 2018-02844, European Union's Horizon 2020 research and innovation programme under grant agreement number 820774, through project MANUELA-Additive Manufacturing using Metal Pilot Line and Vetenskapsrådet (Swedish research council) grant number 2020-06159. The support from Chalmers Production Area of Advance is also acknowledged.

The research was conducted under the academic supervision of Professor Lars Nyborg who also acted as the examiner together with Docent Karin Frisk and Professor Eduard Hryha who were co-supervisors for this thesis work. Adjunct Professor Sven Bengtsson was the industrial supervisor from Höganäs AB, Sweden for this thesis work. This thesis is based on the work contained in the following papers. One patent application was generated during this work.

List of appended papers

I Al–Mn–Cr–Zr-based alloys tailored for powder bed fusion-laser beam process: Alloy design, printability, resulting microstructure and alloy properties
B.Mehta, L.Nyborg, K.Frisk, E.Hryha
Journal of Materials Research 37, pp 1256-1268 (2022)
DOI: https://doi.org/10.1557/s43578-022-00533-1

II Advancing Novel Al-Mn-Cr-Zr Based Family of Alloys Tailored for Powder Bed Fusion-Laser Beam Process
B.Mehta, K.Frisk, L.Nyborg
Journal of Alloys and Compounds 967 (2023)
DOI: https://doi.org/10.1016/j.jallcom.2023.171685

III Microstructure, mechanical properties and fracture mechanisms in a 7017 aluminium alloy tailored for powder bed fusion – laser beam
B.Mehta, T.Mishurova, S.Evsevleev, H.Markötter, G.Bruno, E.Hryha, L.Nyborg, E.Virtanen
Materials & Design 226, 111602 (2023)
DOI: https://doi.org/10.1016/j.matdes.2023.111602

IV The Influence of Processing Parameters on the Al-Mn Enriched Nano-Precipitates Formation in a Novel Al-Mn-Cr-Zr Alloy Tailored for Power Bed Fusion-Laser Beam Process
A.Martucci, **B.Mehta**, M.Lombardi, L.Nyborg
Metals 12(8), 1387 (2022)
DOI: https://doi.org/10.3390/met12081387

V Laser Powder Bed Fusion of an Al-Mg-Sc-Zr Alloy: Manufacturing, Peak Hardening Response and Thermal Stability at Peak Hardness
B.Mehta, A.Svanberg, L.Nyborg
Metals 12(1), 57 (2022)
DOI: https://doi.org/10.3390/met12010057

VI Effect of precipitation kinetics on microstructure and properties of novel Al-Mn-Cr-Zr based alloys developed for powder bed fusion – laser beam process
B.Mehta, K.Frisk, L.Nyborg
Journal of Alloys and Compounds 920(5), pp 1-12 (2022)
DOI: https://doi.org/10.1016/j.jallcom.2022.165870

VII In-situ observation of precipitate formation using scanning X-ray fluorescence in novel Al-alloy tailored for additive manufacturing
I.Lazar, **B.Mehta**, V.Bertschová, S.B.A.Malladi, R. Zhe Tu, S.Das, J.Hagemann, G.Falkenberg, K.Frisk, A.Mikkelsen, L.Nyborg
Manuscript

VIII Role of Cr in Mn-rich precipitates for Al-Mn-Cr-Zr family of alloys tailored for additive manufacturing
B.Mehta, K.Frisk, R.Naraghi, L.Nyborg
Manuscript

IX Thermal Stability In Al-Mn-Cr-Zr Based Aluminium Alloys Tailored For Powder Bed Fusion – Laser Beam
B.Mehta, K.Frisk, L.Nyborg, S.Bengtsson, E.Hryha
Conference Proceedings of WorldPM 2022, Lyon, France

X Mechanical properties of Al-Mn-Cr-Zr based alloys tailored for powder bed fusion-laser beam
B.Mehta, S.Bengtsson, D.Riabov, E.Natesan, K.Frisk, J.Ahlström, L.Nyborg
Manuscript

Contributions to appended papers

I, II, V, VI: The author planned and performed the majority of the experimental work. The author analysed the results together with the co-authors. The author wrote the manuscripts together with the co-authors.

III: These studies were planned and performed jointly with T.Mishurova and S. Evsevleev. Samples were manufactured and post-processed by E.Virtanen. SEM analysis and ex-situ mechanical testing were conducted at Chalmers University of Technology, Sweden and the in-situ tensile, XCT were conducted at BAMline, Germany. The manuscript and analysis were conducted together with all the co-authors.

IV: These studies were planned and performed together with A.Martucci. A part of the SEM and optical microscopy analysis was done by A.Martucci. The author printed all the samples, did the rest of the SEM analysis and wrote the papers together with co-authors. XRD tests were conducted at Höganäs AB.

VII: This study was planned and performed by the author and I.Lazar. Samples were manufactured by the author; FIB was done by V. Bertschová; nanoreactor for in-situ analysis

was setup by S.Das and synchrotron studies were done with support from other co-authors. The analysis and interpretation of the data were done mostly by I.Lazar and the author. The manuscript was written with the co-authors.
VIII: Most of the CALPHAD calculations were conducted by the author and K.Frisk. This study was done in collaboration with Thermo-Calc Software AB, Sweden. The author wrote the manuscript together with the co-authors.
IX, X: These studies were planned and performed together with the co-authors. The author manufactured all the samples, did the post-AM heat treatments on most samples, and conducted the SEM analysis, hardness testing and some of the fractography analysis. Mechanical testing was conducted at Höganäs AB by S.Bengtsson. The long-term heat treatments and high T tensile testing were conducted at Chalmers University of Technology. TEM was conducted by D.Riabov and high-temperature tensile testing was conducted by E.Natesan. The papers were planned and written by the author together with the co-authors.

Patent application

WO2022122670A1: New powder, method for additive manufacturing of components made from the new powder and article made therefrom
Applicant: Höganäs AB, Sweden; Priority date: 10 December 2020
Inventors: Karin Frisk, Sven Bengtsson, Lars Nyborg, **Bharat Mehta**

Papers not appended to this thesis

A Effect of Surface Sandblasting and Turning on Compressive Strength of Thin 316L Stainless Steel Shells Produced by Laser Powder Bed Fusion
B.Mehta, E.Hryha, L.Nyborg, F.Tholence, E.Johansson
Metals 11(7), 1070 (2021)

B New Aluminium Alloy Tailored For Powder Bed Fusion-Laser Beam Process
S.Bengtsson, **B.Mehta**, K.Frisk, L.Nyborg
Conference Proceedings of WorldPM 2022, Lyon, France

C Corrosion resistance of additively manufactured Al-alloys for marine applications-effect of alloying elements and heat treatment
C.Linder, **B.Mehta**, J.Lindén, S.Sainis, C.Zanella, L.Nyborg
Manuscript, to be submitted for publication

D Effect of precipitation reactions on the performance of Al-Mn-Cr-Zr alloys tailored for powder bed fusion-laser beam
B.Mehta, I.Lazar, C.Pauzon, K.Frisk, G.Martin, A.Mikkelsen, L.Nyborg
Manuscript

Table Of Contents

ABBREVIATIONS

3D	3-Dimensional
AM	Additive Manufacturing
ASTM	American Society for Testing and Materials
BSE	Back Scatter Electrons
CAD	Computer-Aided Design
CALPHAD	CALculation of PHAse Diagrams
DOE	Design of Experiments
EOS	Electro-Optical Systems
EDS	Electron X-ray Dispersive Spectroscopy
EBSD	Electron Back Scatter Diffraction
FIB	Focused Ion Beam
FCC	Face Centred Cubic
G	Thermal Gradient (K/mm)
ICME	Integrated Computational Materials Engineering
ICP-OES	Inductively Coupled Plasma-Optical Emission Spectroscopy
ISO	International Organization for Standardization
LOM	Light Optical Microscopy
MEMS	Micro-electromechanical systems
PBF-LB	Powder Bed Fusion-Laser Beam
PPM	Parts Per Million
PSD	Powder Size Distribution
R	Solidification Rate (mm/s)
ROI	Region of Interest
RQ	Research Question
RT	Room temperature
SDAS	Secondary Dendrite Arm Spacing
SEM	Scanning Electron Microscopy
SOM	Stereo Optical Microscopy
SXCT	Synchrotron X-ray computed tomography
TEM	Transmission Electron Microscopy
UTS	Ultimate Tensile Strength
VIGA	Vacuum Induction Melting Inert Gas Atomisation
XRD	X-ray Diffraction
XRF	X-ray Fluorescence

CHAPTER 1:
INTRODUCTION

1.1 Background

Additive Manufacturing (AM), as per ASTM 52900 standard [1], is defined as the process of joining materials to make components from 3-dimensional (3D) data, usually layer by layer, as opposed to formative or subtractive manufacturing methodologies. Such an additive layer-by-layer process enables the possibility to create complex designs (bionic designs and lattice structures) while reducing material wastage significantly [2]–[5]. The powder bed fusion-laser beam (PBF-LB) process is an AM process which has gained popularity for being able to design components that contain internal channels and complicated geometric structures that are nearly impossible with other technologies. Figure 1 illustrates one such example of a demonstrator manufactured using PBF-LB process at Chalmers University of Technology, Sweden. This component was a part of the H2020 MANUELA project (grant agreement no. 820774). The component works as a heat exchanger and was designed with complex internal cooling channels, coupled with fluid dynamic simulations to ensure good performance. The material used was forAM® Al-HS1 [6], which was developed in this PhD thesis work. Parts were printed at Chalmers University of Technology using the EOS M290 machine. Such a complicated component is impossible as a single part with any other conventional manufacturing technique, thus illustrating the strengths of PBF-LB process.

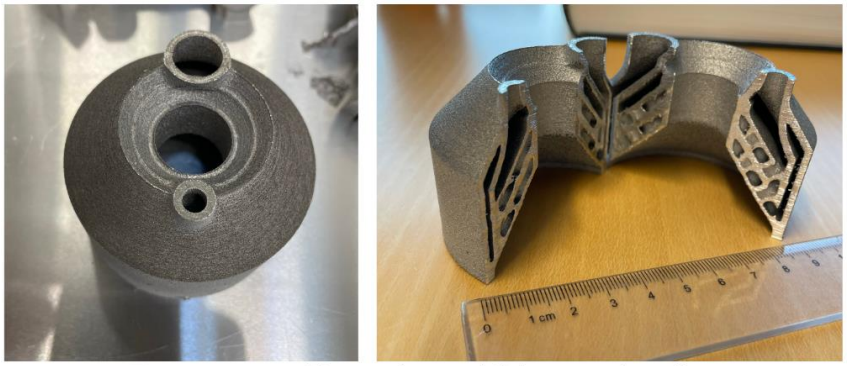

Test geometry (L) top view and (R) cut section view

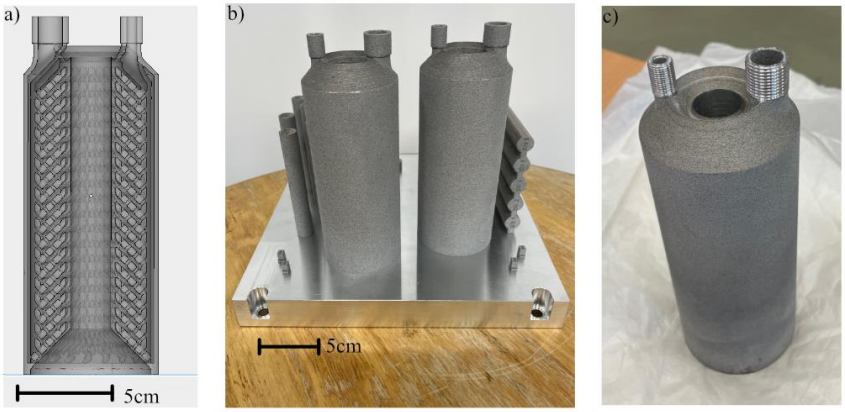

a) CAD cross section b) Printed parts c) Post processed

Figure 1 NEGWATH business use case printed in forAM® Al-HS1 at Chalmers through H2020 MANUELA project (grant agreement no. 820774). The part has been conceptualised and designed by Simon Dybeck, Bättre Design together with CSEM, Switzerland. Post-processing conducted by RISE, Mölndal.

Due to these inherent advantages leveraging the design of better products, the AM industry has been consistently growing with an average growth of 27% year on year standing at 15.2 billion $ in 2021 and forecasting to reach 85.3 billion $ by 2031 [7]. Metal AM accounts for approximately half the share of this AM market, wherein powder bed fusion-laser beam (PBF-LB) is the most commonly used process, comprising about 88% market share in 2019 [8]. This means that PBF-LB for metals represents about 40% of the entire AM market. Despite the benefits of metal AM, the adoption of this technology is not yet implemented at a large scale, accounting for a minuscule of the total revenue from a 15 trillion $ global manufacturing industry [9], [10]. Reasons such as low productivity, high cost per part, high energy consumption and lack of material availability are cited as common reasons [7].

This thesis focuses on the materials aspect as an important part of the metal AM development and how tailored materials can create value for the entire PBF-LB process chain. From a materials perspective, there is considerable growth in the number of available materials for PBF-LB [7], [11], [12]. This alternative still falls short of thousands of metallic alloys to choose as options in conventional metallurgy [13]–[15], which means that the true potential of value creation of PBF-LB is not achieved. Figure 2 illustrates how the conventional Al-alloy processing compares to the PBF-LB process. It can be seen that a conventional Al-alloy processing route creates proportionally higher value with an increase in the number of parts (mostly via cost reduction), thus making it lucrative for large-scale production. However, the PBF-LB process is agnostic to the number of parts produced. Even though the design for PBF-LB can enable value creation, it falls short to be adopted beyond small-scale production mainly due to higher costs per part [16], [17]. One way to significantly enhance the process would then be to create alloys tailored for the PBF-LB process. Such alloys would then leverage the benefits of this process providing performance gains, thus creating added value. Of course, one of the key aspects of such tailored alloys has to be keeping costs under control. If the alloys contain for example rare earth elements, this makes such alloys overly expensive while not providing proportional performance gains and the value creation aspect gets diluted.

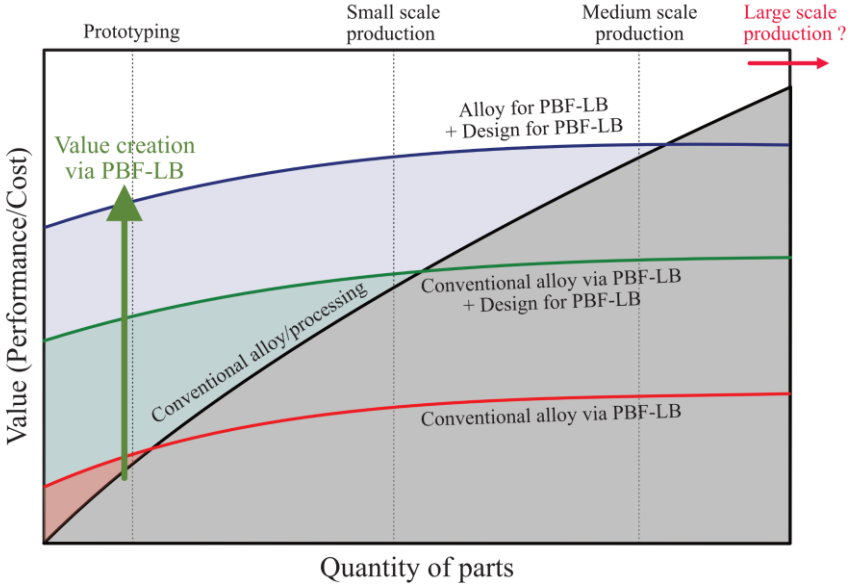

Figure 2 A schematic of value creation via the PBF-LB process. The feasibility of certain processing routes is dependent on the value it creates. Only by enhancing design freedom and alloying freedom can PBF-LB become valuable for medium-large scale manufacturing. Inspired by [18]

Since the last 15 years, an exponential increase in the number of patents published within the field of AM (see Figure 3) also indicates increasing innovations in the process, methods, and materials for AM. About 20-30% of the patents within AM belong to materials for AM, thus suggesting that potential innovations related to materials for AM have followed the overall trend. However, aluminium alloys constituting a significant amount of the manufacturing industry [19], [20], contributed little to innovation aspects in this field. For example, aluminium alloys for AM (143 patents) contributed only 2% of the patents of materials for AM (8233 patents) and 6% of the patents of aluminium alloys (2553) in 2020.

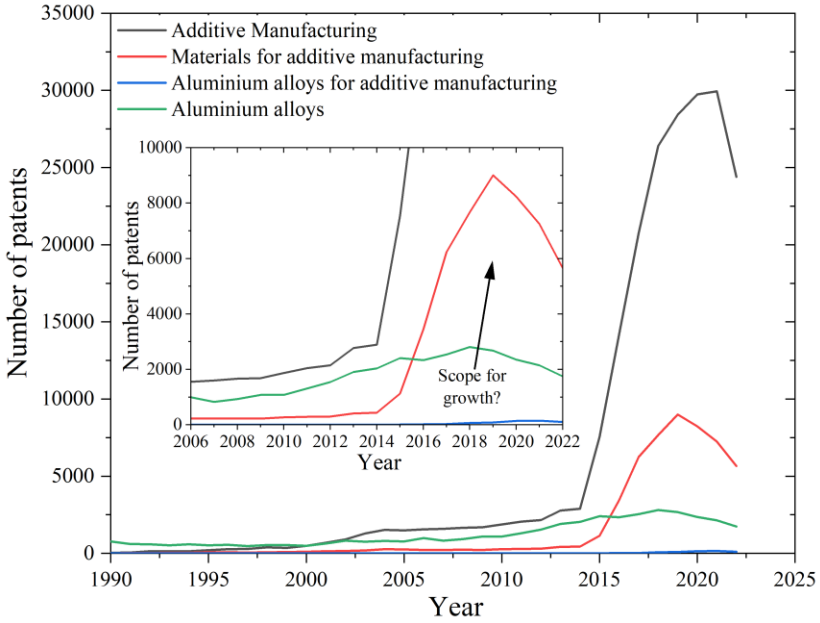

Figure 3 Number of patents published since 1990 in the field of additive manufacturing. Inset shows the range from 2006 onwards focusing on Aluminium alloys. Data sourced from Espacenet in April'2023.

It is clear that within materials for AM (with focus on the PBF-LB process), the development of novel Al-alloys has a big scope of growth that can be explored. This thesis study has thus focused on the development of an entirely new alloy system which is tailored for the PBF-LB process. CALPHAD-based tools were used as a guide to design the alloys, explain and overcome defects formed during processing (such as solidification cracking) and understand post-AM processing reactions (such as precipitation hardening). As mentioned before, the alloy system was designed to keep a strong focus on the value-creation aspect via the PBF-LB process. Thus, the alloys were designed without any rare earth materials or critical elements [21]. For the Al-Mn-Cr-Zr based alloy system developed, high mechanical strength combined with high-temperature strength and general corrosion resistance were identified as objectives. Thus, this translated to a high performance alloy system.

1.2 Objectives

The primary objective of this thesis study has been to show a "proof of concept" of a novel Al-alloy family tailored for the PBF-LB process with the aim for high strength (>450 MPa) combined with specific secondary properties such as high-temperature strength (up to 573 K) and general corrosion resistance.

The objectives of this thesis can be summarized as the following research questions (RQ)

RQ1: How to design Al-alloys tailored for the PBF-LB process?

RQ2: How does the microstructure develop during the PBF-LB process and post-processing heat treatments?

RQ3: To what extent could such Al-alloys meet the performance goals?

1.3 Research approach

Al-alloys that are tailored for the PBF-LB process were studied as the primary part of this thesis study. CALPHAD-based tools combined with extensive literature studies were employed as a guide to creating alloy recipes, which are printable, defect-free and trigger different features during PBF-LB processing or post-PBF-LB heat treatments (**RQ1**). Within alloying methodologies, in-situ and ex-situ alloying was investigated to create printable alloys with nominally full density (**RQ1**). A model alloy system was developed (Al-Mn-Cr-Zr based) and studied in depth at multiple length scales with the help of advanced tools such as microscopy, in-situ measurements, CALPHAD methods and mechanical testing to shed light on the complex structure-property relationship of these alloy systems during PBF-LB processing and post processing heat treatments (**RQ2**). Finally, commercially available alloy systems were benchmarked against this model alloy system to shed light on the benefits/ limitations of such an alloy concept (**RQ3**). These alloys were tested for uniaxial tensile testing, bending fatigue and high-temperature stability (**RQ3**).

Table 1 summarises the scope of the thesis by connecting the different research questions with the alloys studied and the equipment used to produce them. The primary objective of each appended paper as linked to the research questions can be summarized as follows

- **Paper I:** This paper addresses the basic alloy design ideology behind the Al-Mn-Cr-Zr-based alloys and how the design of experiments (DOE) approach can assist in producing fully dense crack-free samples (RQ1, RQ2)
- **Paper II:** Here, Zr addition beyond solubility and Mg additions to Al-Mn-Cr-Zr-based alloys are explored to show the extent of microstructural control possible via PBF-LB (RQ1, RQ2, RQ3)
- **Paper III:** This paper represents the scope of ex-situ alloy design by admixing Zr + TiC to a 7017-grade Al-alloy for creating fully dense samples. Fracture behaviour is studied to understand controlling mechanisms for mechanical properties (RQ1, RQ3)
- **Paper IV:** This study addresses the effect of varying processing parameters on supersaturation limits in Al-Mn-Cr-Zr alloys while being at nominally high density (RQ1, RQ2)
- **Paper V:** In this paper, the scope is to evaluate the printability, and microstructure of Al-Mg-Sc-Zr alloy to benchmark against Al-Mn-Cr-Zr alloy (paper IX) (RQ1, RQ3)
- **Paper VI:** This paper focuses on the precipitation reactions in Al-Mn-Cr-Zr during direct ageing heat treatments to postulate the role of alloying elements on precipitation hardening (RQ2, RQ3)

- **Paper VII:** This study aims at advancing the understanding of precipitation reactions in alloys developed in papers I, II and VI using in-situ heat treatments at synchrotron facilities with X-ray fluorescence (RQ2)
- **Paper VIII:** This paper focuses on the effect of Cr solubility in Mn-rich precipitates on the precipitation kinetics of Al-Mn-Cr-Zr alloys, involving the use of CALPHAD approach and the tentative role of Cr in enhancing the precipitation hardening effect (RQ2)
- **Paper IX:** This study benchmarks the Al-Mn-Cr-Zr alloys against Al-Mg-Sc-Zr alloys for long-term thermal stability tests. Effects studied both with CALPHAD tools and microstructural characterization of long-term heat-treated samples (RQ2, RQ3)
- **Paper X:** Room temperature tensile behaviour, bending fatigue behaviour and high-temperature tensile behaviour of Al-Mn-Cr-Zr based alloys are studied in this paper to elucidate the mechanical properties of this alloy system (RQ2, RQ3)

Table 1 Link between the research questions, materials and equipment used for studies reported in appended papers

Paper	RQ1	RQ2	RQ3	Material studied	Machine
Paper I	■	■		Al-Mn-Cr-Zr	EOS M100
Paper II	■	■	■	Al-Mn-Cr-Zr	EOS M290
Paper III	■		■	Al-7017 + Zr + TiC	EOS M290
Paper IV	■	■		Al-Mn-Cr-Zr	EOS M100
Paper V	■		■	Al-Mg-Sc-Zr	EOS M100
Paper VI		■	■	Al-Mn-Cr-Zr	EOS M100
Paper VII		■		Al-Mn-Cr-Zr	EOS M290
Paper VIII		■		Al-Mn-Cr-Zr	EOS M100
Paper IX		■	■	Al-Mn-Cr-Zr, Al-Mg-Sc-Zr	EOS M100
Paper X		■	■	Al-Mn-Cr-Zr	EOS M290

CHAPTER 2:
POWDER BED FUSION-LASER BEAM

2.1. Working principle

Powder bed fusion-laser beam (PBF-LB) utilises a laser beam to selectively melt a thin layer of powder. This process is then repeated several times to build components layer by layer. Such a method thus uses a "near-net-shape" approach of producing components similar to the powder metallurgy route thus reducing material wastage while providing unprecedented design freedom [4], [22].

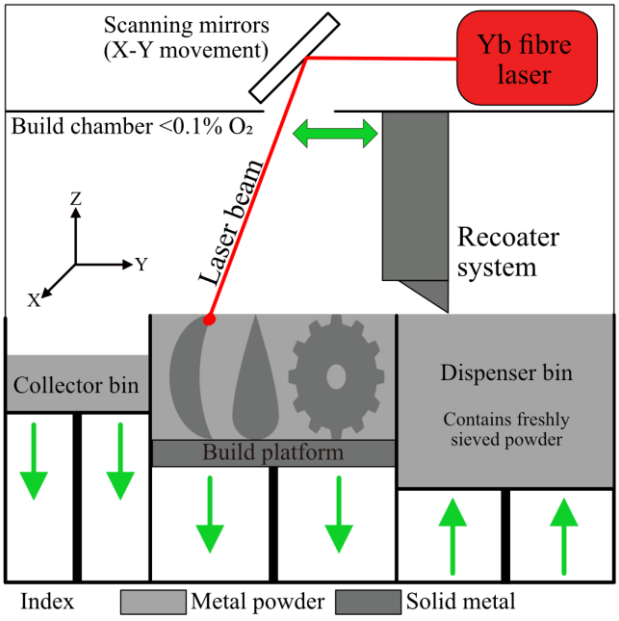

Figure 4 Schematics for a typical metal PBF-LB system in two dimensions. Green arrows demarcate the movement of mechanical components during the PBF-LB process.

The schematics for a typical metal PBF-LB system are presented in Figure 4 which shows the major components of the system during operation. The illustration follows a setup similar to the EOS M290 machine (EOS GmbH, Germany), which has been used in this thesis study. There could be other setups possible depending on the machine or laser source employed. A build chamber shielded with a protective atmosphere (usually Ar, N_2) with <0.1% O_2 (1000 ppm) is kept as the set point. A dispenser bin containing freshly sieved metal powder which is spread with a recoater system on the build platform. After the application of a thin layer of metal powder (usually between 20-80 µm), a Yb-fibre laser selectively melts the area which needs to be built up. This selective melting is done utilising several scanning strategies and processing parameters which have been a subject of research over the years [22]–[24]. The extra powder during recoating goes into the collector bin to be recovered after printing. There are other metal PBF-LB systems where the powder dispenser is rather placed on top of the recoater system such as for EOS M100 machines. Hence, the dispenser bin is then placed on the recoater system where a layer of powder is spread during recoating with the help of gravity.

2.2. Process parameters

The parameters during the PBF-LB process directly affect the resulting properties of the material. This section will elaborate only on the parameters concerning the processing of a component in a PBF-LB machine. The atomisation of metal powder and powder specifications are addressed in a later section 4.2. The parameters that directly affect the manufacturability of a material are laser power, laser speed, layer thickness and hatch distance that are used to reach full density of the alloys manufactured [23]. Figure 5 shows a schematic for some of the parameters for a better understanding of processing parameters. Laser beam characteristics and the scanning direction of the laser define the laser power and laser speed respectively.

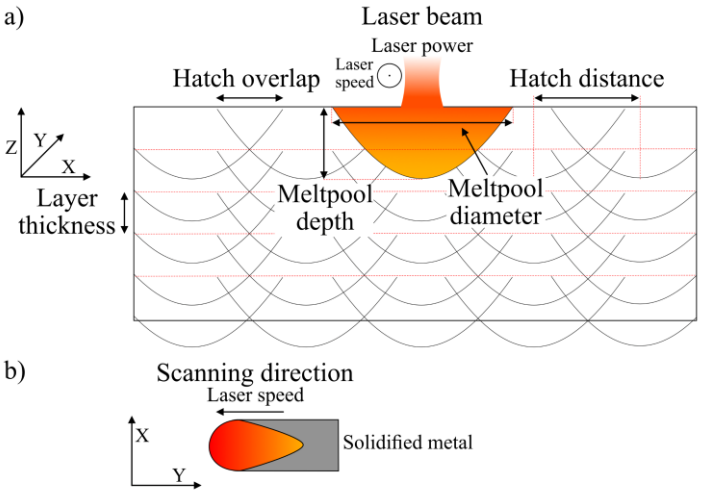

Figure 5 a) Schematic overview of process parameters during PBF-LB process along XZ direction b) XY direction representation of laser scanning creating solidified metal behind. Based on [23]

The laser beams used in the PBF-LB machines in this thesis comprised a Yb-fiber laser with a Gaussian power density distribution [25], [26]. A Gaussian power provides the highest intensity at the centre of the beam and decreases as a function of radial distance from the beam centre. The laser diameter is thus quite important as it directly affects the amount of heat input to the material. For example, a 40µm spot size laser at 170 W power (used in EOS M100 machine) would contain two-three times the amount of energy input per unit area (W/m^2) than a 100µm spot size laser at 370 W power (used in EOS M290 machine). The laser speed controls the amount of heat added to the system, making it a crucial processing parameter. On a component level, the laser scan speed is crucial to ensure proper melting of the material to create proper bonding between two layers and between two melt tracks. On a microstructural level, the amount of heat added affects the phases formed, solidification mechanisms and resulting micro/ macro stresses. Hatch distance is the distance between the centre of two adjoining melt pools if viewed along the XZ plane (see Figure 5). This distance is optimised based on the dimensions of the melt pool and layer thickness. The layer thickness, as the name suggests is the thickness of each consecutive layer during PBF-LB processing. Layer thicknesses of up to 100µm have been reported to be used by researchers and machine manufacturers [26]–[28]. There are a few other parameters which were studied in lesser detail in this thesis. One is powder drying. The Al-powder is prone to the formation of hydroxides upon storage in humid conditions which could affect the print quality and mechanical properties of resulting parts [29]. For the same reason, sieved virgin powder for samples

produced in the EOS M100 machine (*paper I, V*) was dried at 353 K for 4 h before each print. The powder used for the EOS M290 machine was not dried due to limitations of space to dry and the effect of moisture pickup to these powders, which was not established properly. Another parameter is the build plate pre-heating. Researchers have found that build plate pre-heating helps to reduce residual stresses during the PBF-LB process [30]. Pre-heating was not studied directly as part of the thesis, although some samples were produced (up to 473 K) to measure the impact of build plate pre-heating on microstructure and residual stresses as part of H2020 MANUELA project (grant agreement no. 820774) when processing advanced use cases. Lastly, the effect of gas flow on as-printed density was also studied based on work by Pauzon [8]. *Paper I* contained samples which were cut along all three planes (XY, XZ and YZ) to also elaborate on the effect of gas flow on the relative density of the sample. Apart from those major parameters mentioned above, several other parameters such as pulsed laser beam, scanning strategy (chessboard, stripes etc.), recoater speed, type of recoater blade, process gas, etc. are topics of study other researchers [22], [23], [31]–[33]. These parameters were not considered in this thesis study.

2.3. Thermo-physical phenomena

This section highlights the thermo-physical phenomena that occurs as the laser beam interacts with a powder bed, with a special focus on Al-alloys. All the phenomena mentioned below are mentioned in the order of factors to be considered as the laser travels from the source to the material and moves along a pre-determined path to selectively melt the material.

2.3.1. Laser reflectivity

Laser reflectivity is an issue which is not highly relevant for Fe-/Ni-based alloys as a lot of laser energy is absorbed. However, Al or Cu are associated with high reflectivity. For a Yb-fiber laser as shown in Figure 6a), pure Al is expected to absorb <10% of the laser energy. Metal powder, due to an enhanced surface area combined with the fact that the material is alloyed Al and contains oxides on the powder surface of Al [34] increases the absorptivity of the laser as seen in Figure 6b) wherein about 60-70% laser is supposed to be absorbed by Al powder [35]. This still means that there is a lot of energy lost when manufacturing Al-alloys and it is usually compensated by using high power for producing fully dense samples. This has to be carefully balanced with high laser speed so that aluminium does not evaporate due to low boiling temperatures. For example, in this thesis, when samples were produced in EOS M100 and M290 machines, full powers of 170 W and 370 W respectively were used for producing nominally full-density samples together with high laser scanning speeds (>1000 mm/s). A similar approach has been used by other researchers [22], [36].

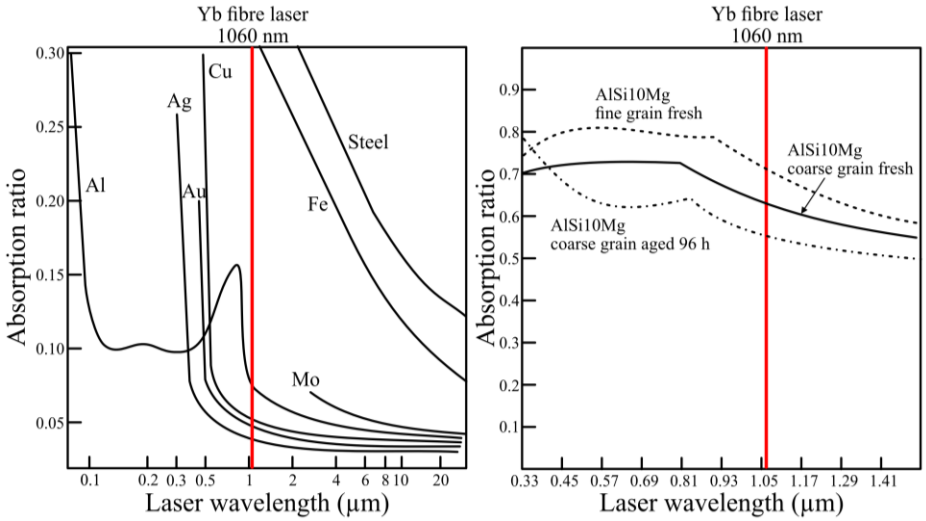

Figure 6 Theoretical absorption ratio of laser in metals as a function of laser wavelength, redrawn manually from [37]. Actual absorption ratio of laser in different AlSi10Mg powders as a function of wavelength, redrawn manually from [35]. Axes may not be considered to scale

2.3.2. Melt pool formation and solidification phenomenon

After consideration of the laser interacting with the powder surface, the next step to consider is the melt pool formation and resulting solidification phenomena. As shown schematically in Figure 7, the melt pool formation is highly dependent on the amount of laser energy absorbed, which is controlled by varying the process parameters as mentioned before. Providing low energy creates a conduction mode type of melt pool which is shallow and wide. On the other hand, high energy leads to a keyhole mode which is deep and narrow. In both cases, layer-by-layer deposition of material can be susceptible to defects. The conduction mode can lead to a lack of fusion defects due to incomplete overlaps between melt pools. The keyhole mode, on the other hand, may lead to entrapped vapour inside the material. Hence, it is important to understand the melting mode during the processing of material to optimise the processing parameters accordingly. This would ensure nominally full-density components.

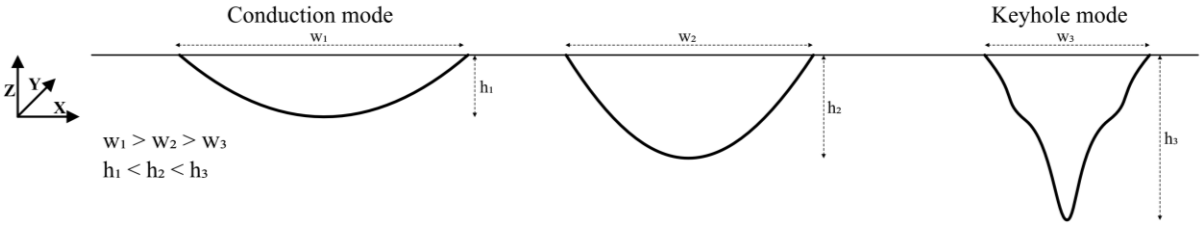

Figure 7 Schematic for different types of melt pools formed due to varying laser power

The solidification of the melt pool is critical to the resulting microstructure. Figure 8 shows the five typical solidification structures formed during the solidification of metals with a temperature gradient (G, K/mm) and solidification rate (R, mm/s) as the parameters. It can be seen that the general solidification structure created during PBF-LB processing is finer due to increased cooling rates, which corresponds to increased thermal gradient and solidification rate (cooling rate = G*R). However, on a local microstructural level, there is a gradient. As shown by [38], [39], the temperature gradient decreases and the solidification rate (and resulting solidification front velocity) increases as one moves from the melt pool boundary to the centre/ surface of the melt pool. Such a local gradient could result in segregations or solute trapping at

micrometre (µm) length scale. Additionally, nucleation of primary precipitates can be caused especially at melt pool boundaries. One example is Al_3Zr precipitates that led to grain refinement (see *Paper II* and *Paper III*).

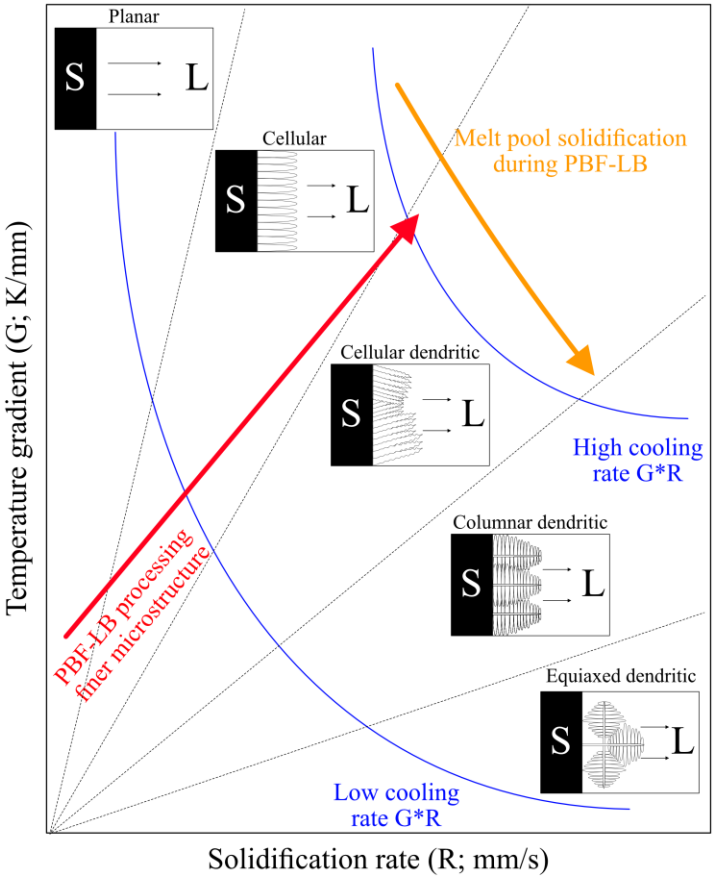

Figure 8 Thermal gradient (G) vs solidification rate (R) showing the five common solidification structures formed during solidification of metals. The effect of PBF-LB is shown by arrows, the red direction shows the general effect of PBF-LB in terms of microstructure development and the orange arrow shows local microstructural development of melt pool during PBF-LB. Schematic is based on [38], [40]

2.3.3. Spatter formation

Spatter is generated as a consequence of laser interaction with the powder bed. It is the by-product that is oxidised depending on atmospheric conditions inside the build chamber and may comprise agglomerated particles [41], [42]. As per [8], [32], the spatter particles could be categorised as either cold or hot spatter particles. Cold spatter is formed when particles are ejected from powder bed whereas hot spatter are the ones that are partially, or completely molten metal particles being ejected. The hot spatter is undesirable in the material as there is always a risk that the ejected spatter particles can drop to another position on the build plate and be incorporated into the build as the next build layer is deposited. The hot spatter is comprised of oxidised metal particles and may hence be difficult to remelt into the material. This becomes a cause for defects which could later affect material properties [43]. Additionally, spatter particles could be harmful as they accumulate over powder reuse and could impact the overall long-term powder and part qualities [43], [44].

2.3.4. Re-melting phenomenon

Re-melting of layers is a mandatory element of the additive manufacturing process. Each layer, after deposition is remelted to maintain full bonding with the previous layer. This phenomenon

creates an undesirable effect, especially for precipitation-hardening Al-alloys (and other precipitation-hardening alloys) wherein the aim is to create fully supersaturated solid solutions. On one hand, the rapid solidification process enables increased solubility of elements, but the re-melting heats the previous layers beyond the precipitation temperature, thus increasing the susceptibility to form precipitates at or close to melt pool boundaries (see Figure 9). This effect is similar to the potential precipitate formation in heat-affected zones (HAZs) experienced during the welding of precipitation-hardened Al-alloys [40], [45]. Thus, the potential increase in solubility is reduced due to re-melting.

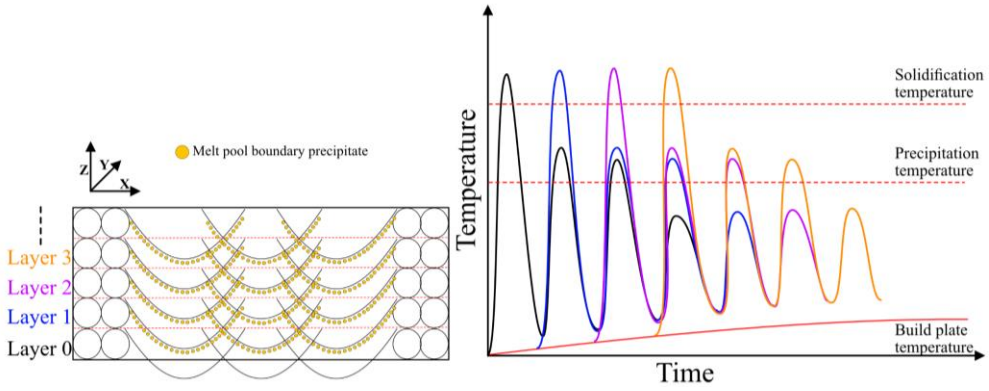

Figure 9 Schematic of PBF-LB process showing remelting effect, forming melt pool boundary precipitates (yellow). The graph on the right shows the corresponding thermal history at layer 0 onwards. Redrawn from [42], [46]

2.4. Defects formed during processing

2.4.1. Lack of fusion

Lack of fusion porosity is formed when two laser tracks do not overlap optimally, or the energy used is low. This lack of cohesion between two laser tracks can cause lack of fusion defects, which can form within a layer (inter-track) or between two layers (inter-layer) [32], [42]. Such defects are critical due to their shape which results in poor mechanical properties [47]. Figure 10 shows lack of fusion defects formed in an Al-alloy processed with too low energy input.

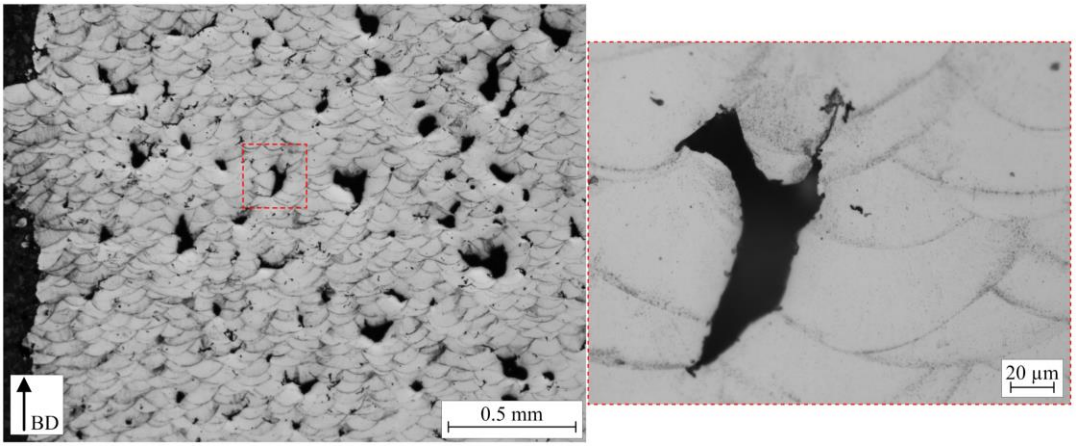

Figure 10 Lack of fusion porosity in PBF-LB processed alloy C (Al-Mn-Cr-Zr based alloy). The inset focuses on one of such defects. Inset image redrawn from [48]

2.4.2. Keyhole porosity

Keyhole porosity is formed as a result of instabilities in the melt pool, where a high-power laser causes pore formation which gets entrained due to Marangoni convection and overcomes buoyancy forces to stay in the melt pool upon solidification [32], [49]. These pores are usually

more spherical than lack of fusion pores (see Figure 11), thus being less detrimental to resulting properties as compared to them.

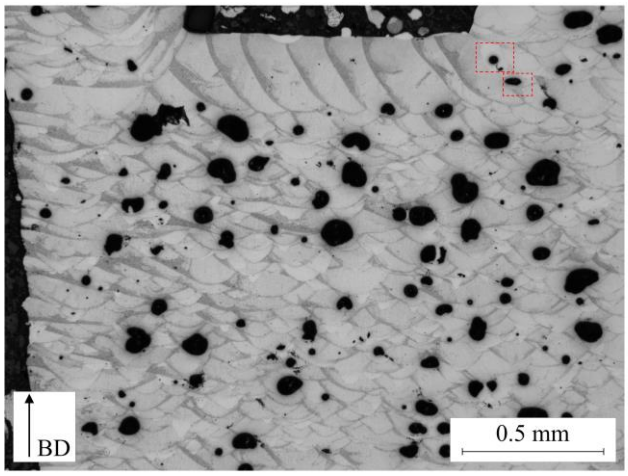

Figure 11 Keyhole porosity in PBF-LB processed alloy C (Al-Mn-Cr-Zr based alloy). The pores are highlighted in red

2.4.3. Gas porosity

Gas porosity is generalised in this thesis as the porosity which originates from raw material (atomized powder) or evaporation of low melting elements (such as Al, Mg). Such pores are usually <10µm in size (see Figure 12), sometimes being sub-micron sizes thus making them hard to see. Due to their size and spherical appearance, the pores are usually unavoidable when producing Al-alloys and thus there always exists a small residual porosity (often <0.05%) [27].

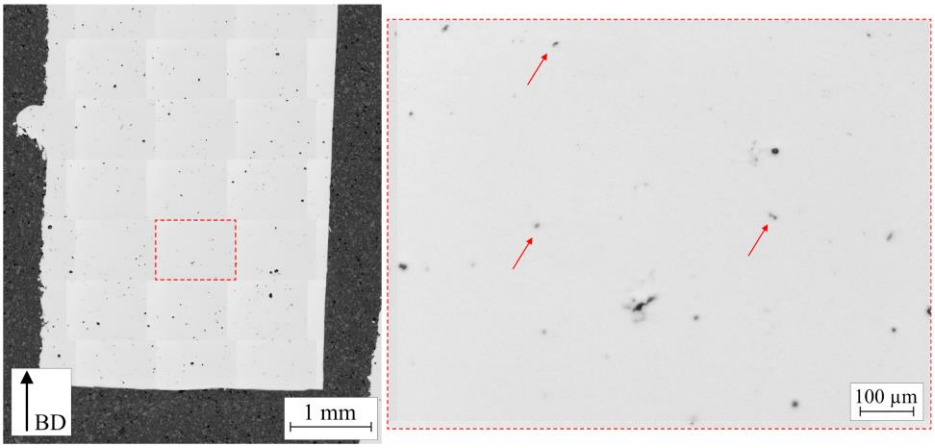

Figure 12 Gas porosity in PBF-LB processed alloy C (Al-Mn-Cr-Zr based alloy). The pores are shown in the inset image with red arrows

The evaporation phenomenon combined with local overheating at sample edges can also lead to sub-surface porosity when producing Al-alloys via PBF-LB as shown in Figure 13a) [50]–[52]. Such porosity could be detrimental to mechanical and corrosion properties if the material is intended to be used without machining to remove the outer layers. This porosity can be significantly reduced by employing two methods. One is by contour scanning which melts the border before/after the bulk scanning. Another is via alloy design as alloys containing Mg namely alloys E, and F in the Al-Mn-Cr-Zr family of alloys did not possess this issue.

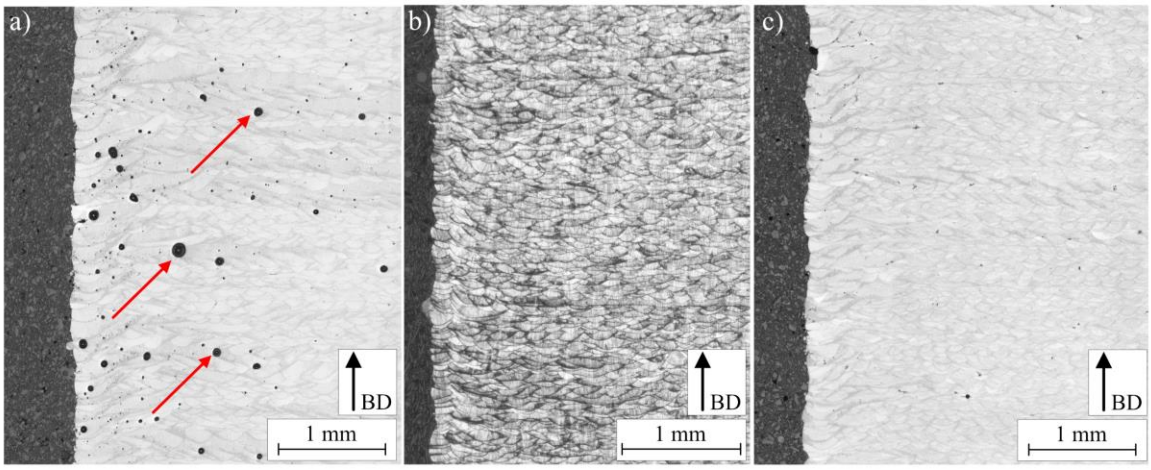

Figure 13 Sub-surface porosity on a) Alloy C (Al-Mn-Cr-Zr) along building direction (marked in red). The porosity goes away significantly in b) Alloy C (Al-Mn-Cr-Zr) with contour scanning activated and c) Alloy F (Al-Mn-Cr-Zr). Melt pools in image b) look more pronounced as it is etched for a longer time

2.4.4. Solidification cracking

Solidification cracking (or hot cracking) is a major issue that affects several Al- and Ni-alloys for several manufacturing processes. As per [40], [53], these cracks originate when there is a combination of thermal contraction and the inability to fill the final melt with enough liquid. These cracks typically originate between grain boundaries when two adjoining Al-grains during the end of solidification are under tensile stress and are not fed with sufficient liquid [53]. For PBF-LB processes, as shown in Figure 14, these solidification cracks can run across multiple layers up to several hundred µm which can severely impact the mechanical properties of the material in question [54]. In this thesis study, alloys susceptible to solidification cracking were intentionally designed (an example shown in Figure 14) to show the extent of cracking and two possible solutions. A method of identifying and ranking tentative solidification cracking susceptibility based on Scheil simulations [55] as suggested by Sindo Kou [53] was also discussed.

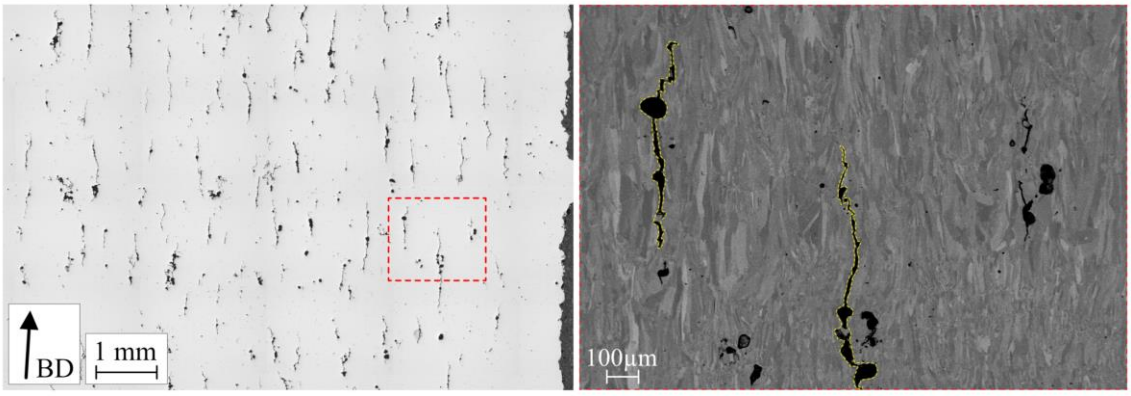

Figure 14 Solidification cracking in alloy E (Al-Mn-Cr-Zr alloy). Inset shows the cracks as an electron micrograph image using backscattered mode. The columnar Al-grains are visible as a contrast along building direction (BD). Solidification cracks are marked in yellow

2.4.5. Residual stress

Residual stresses are the stresses that remain in a body at equilibrium [56]. Such stresses can be detrimental (for welded joints) and good (for toughened glass). Usually, three scales of residual stresses exist, namely types I, II, and III [57]. Type I results from macro-stresses acting on the entire part, type II originate from micro stresses occurring at µm scale whereas type III

occurs on a nanometric scale. The only type I stresses are relevant on a length scale where stresses large enough to cause part failure to occur, thus only these stresses are considered here. Residual stresses in the PBF-LB process occur due to the inherently high thermal gradients and rapid solidification rates, which create a thermal gradient >1000 K in small local regions as shown in Figure 15a). This, combined with the thermal history of each layer being exposed to thermal gradients in a solid state causes stresses to build up. Sometimes, these stresses overcome the yield strength of the material and cause plastic deformation or even delamination between layers or of the whole component, as seen in Figure 15b), which then is a relaxation of built-up stresses. Delamination from residual stresses can sometimes be fixed. For the case in Figure 15, the delamination was mitigated by creating a stronger connection with the build plate (no supports) combined with large radii at the bottom to reduce stress concentrations.

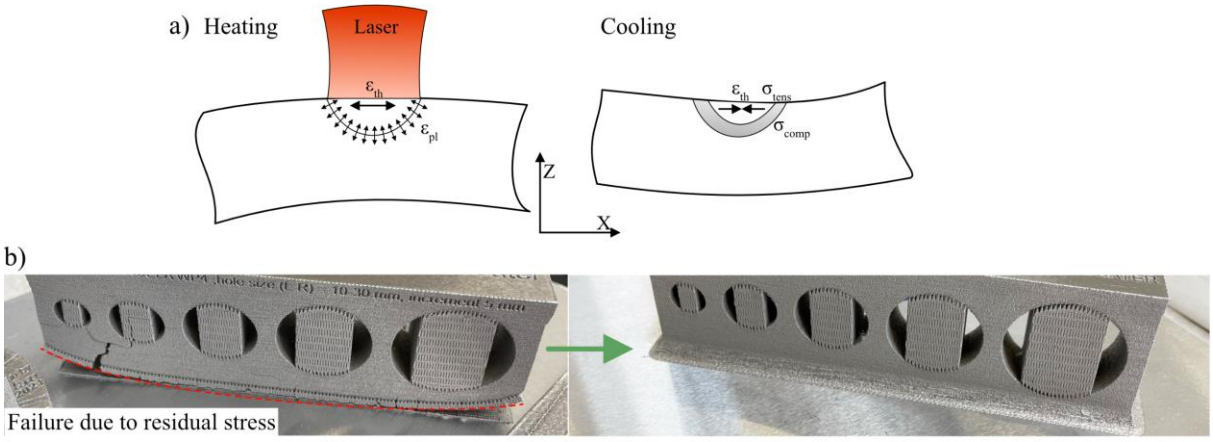

Figure 15 a) Residual stresses formed during heating and cooling process during PBF-LB process showing thermal strains (ε_{th}) and plastic strains(ε_{pl}) which causes tensile and compressive stresses in a material [58] b) Illustration of residual stress causing failure (follow dotted red line) in a long component (length~20 cm). It was avoided by a solid connection to build a plate and a large radius to avoid stress concentration. Printed in Al-Mn-Cr-Zr alloy in H2020 MANUELA project (grant agreement no. 820774)

CHAPTER 3:
ALUMINIUM ALLOYS

3.1. Definition

Aluminium (Al) is one of the most abundantly available metals on Earth [59]. Aluminium and its alloys are used in nearly every industry. The major benefit of Al-alloys is high specific strength making them an ideal system for light-weighting products. This is realised by alloying pure-Al, which has a yield strength of 15 MPa to reach high strengths up to 600 MPa [13], [60], [61]. Aluminium alloys have been developed over the past hundred years, with major alloying elements being Cu, Mg, Zn and Si. All these alloying elements are considered lucrative due to their solid solubility in Al. This solid solubility provides solid solution strength directly after processing. Later on, precipitation hardening can be employed via post-processing heat treatments to reach high strengths. Other elements or even the abovementioned elements beyond the solubility limit are avoided due to the formation of harmful intermetallic phases during solidification which can lead to a loss in properties. A summary of different Al-alloy series based on two of the most common processing routes namely wrought and cast alloys are shown in Table 2.

Table 2 Strength ranges of different wrought and cast aluminium alloys. Data taken from [62]

Wrought aluminium alloys			
Aluminium series	Type of alloy composition	Strengthening method	Tensile Strength (MPa)
1xxx	Al	Cold work	70-175
2xxx	Al-Cu-Mg (1-2.5% Cu)	Heat treat	170-310
	Al-Cu-Mg-Si (3-6% Cu)	Heat treat	380-520
3xxx	Al-Mn-Mg	Cold work	140-280
4xxx	Al-Si	Cold work (heat treatment)	105-350
5xxx	Al-Mg (1-2.5% Mg)	Cold work	140-280
	Al-Mg-Mn (3-6% Mg)	Cold work	280-380
6xxx	Al-Mg-Si	Heat treat	150-380
7xxx	Al-Zn-Mg	Heat treat	380-520
	Al-Zn-Mg-Cu	Heat treat	520-620
8xxx	Al-Li-Cu-Mg	Heat treat	280-560
Cast aluminium alloys			
Heat treatable sand cast alloys (various tempers)			
Alloy system (AA designation)		Tensile strength (MPa)	
Al-Cu (201-206)		353-467	
Al-Cu-Ni-Mg (242)		186-221	
Al-Cu-Si (295)		110-221	
Al-Si-Cu (319)		186-248	
Al-Si-Cu-Mg (355, 5% Si, 1.25% Cu, 0.6%Mg)		159-269	
Al-Si-Mg (356,357)		159-345	
Al-Si-Cu-Mg (390, 17% Si, 4.5%Cu, 0.6% Mg)		179-276	
Al-Zn (712, 713)		241	
Non-heat treatable die-cast alloys			
Al-Si (413, 443, F temper)		228-296	
Al-Mg (513, 515, 518, F temper)		276-310	
Non-heat treatable permanent mould cast alloys			
Al-Sn (850, 851, 852, T5 temper)		138-221	

3.2. Strengthening mechanisms in Al-alloys

It can be seen from Table 2 that the highest strengths for Al-alloys is produced by Cu- and Zn-containing Al-alloys. Both these elements have high enough solubility in Al (2.5 at% and 18.9 at% respectively) to produce desirable precipitates. These precipitates are usually coherent/ semi-coherent with the Al-matrix and can significantly strengthen it. The overall increase due to different strengthening mechanisms can be summarised according to equation 3.1. It is assumed for the time being that a simple addition principle would point to an expected increase in the strength of the final alloy. However, strengthening mechanisms are complicated and more work would be needed to quantify each effect.

$$\sigma_{total} = \sigma_0 + \Delta\sigma_{SS} + \Delta\sigma_{GB} + \Delta\sigma_{Ppt} + \Delta\sigma_{Dis} \quad [3.1]$$

In equation 3.1, σ_0 is the strength of pure Al = 10-15 MPa [63], [64], $\Delta\sigma_{SS}$ represents strengthening due to the solid solution effect, $\Delta\sigma_{GB}$ represents strengthening due to the grain size effect, $\Delta\sigma_{Ppt}$ represents precipitation hardening effect and $\Delta\sigma_{Dis}$ represents dislocation strengthening. The following sub-sections elaborate on each strengthening effect.

3.2.1. Solid solution strengthening

Solid solution strengthening in metals could be through interstitial alloying or substitutional alloying. In the case of interstitial alloying (common for Fe-alloys), elements such as C, and N occupy interstitial places between atoms thus creating a stress field around the matrix. The substitutional alloying which is the focus for Al-alloys occurs when an atom replaces Al-atom thus creating a stress field due to a difference in atomic radius and electron configuration. This stress field strengthens the matrix by restricting dislocation motion. A schematic is shown in Figure 16.

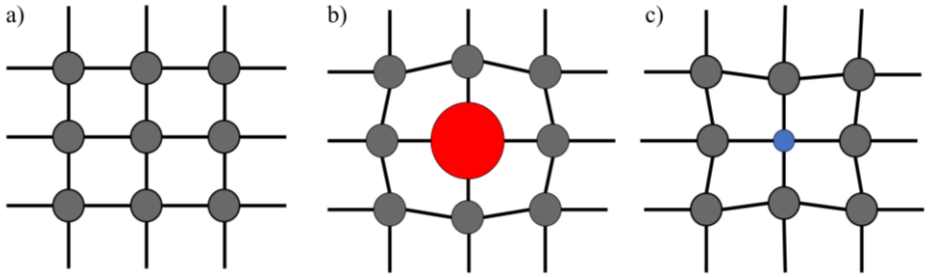

Figure 16 Illustration of substitutional solid solution, where grey atoms represent Aluminium and red and blue atoms represent substitutional atoms which are larger or smaller in radius respectively

Solid solution strengthening has been explained in detail by several authors [65]–[67]. The model suggested by Uesugi et al. [67], based on first principle studies of several binary Al-alloys up to 3.7 at% was considered as a good representation for predicting tentative solid solution strengthening for PBF-LB processing. The solid solution strengthening ($\Delta\sigma_{SS}$) can be written as shown in equation 3.2.

$$\Delta\sigma_{SS} = M\left(\frac{3}{8}\right)^{\frac{2}{3}}\left(\frac{1+v}{1-v}\right)^{\frac{4}{3}}\left(\frac{w}{b}\right)^{\frac{1}{3}}G|\varepsilon|^{\frac{4}{3}}c^{\frac{2}{3}} \quad [3.2]$$

In equation 3.2, M is Taylor's mean orientation factor = 3.06 [68], v is Poisson's ratio = 0.345 [68], $w = 5b$ where b is Burger's vector for Al = 0.286 nm [69], G is shear modulus of Al = 25.4 GPa [69], ε is the lattice strain (%) from the solute and c is concentration of solute (at%).

3.2.2. Grain size effect

The size of primary grains inversely affects the strength of an alloy, which is commonly known as the grain size effect or Hall-Petch effect after the classical papers by Hall and Petch [70], [71]. This effect can be written as shown in equation 3.3.

$$\Delta\sigma_{GB} = kd^{-\frac{1}{2}} \quad [3.3]$$

In equation 3.3, $\Delta\sigma$ represents the increase in yield strength, k is the Hall-Petch constant (MPa.µm$^{1/2}$) and d is grain size in µm. For Ni- and Fe- alloys, k can be 230 MPa.µm$^{1/2}$ and 310 MPa.µm$^{1/2}$ respectively, thus making the effect much more pronounced as compared to Al-alloys, wherein k is reported to be around 90 MPa.µm$^{1/2}$ [64]. Al-haidary et al. [63] also argued that, depending on the alloying elements and processing conditions, this constant could for Al-alloys vary between 70-130 MPa.µm$^{1/2}$, thus having a large impact on tentative grain size effect. Figure 17 illustrates this effect in the range of 0.1-1000 µm which covers the range of grain sizes for most Al-alloys.

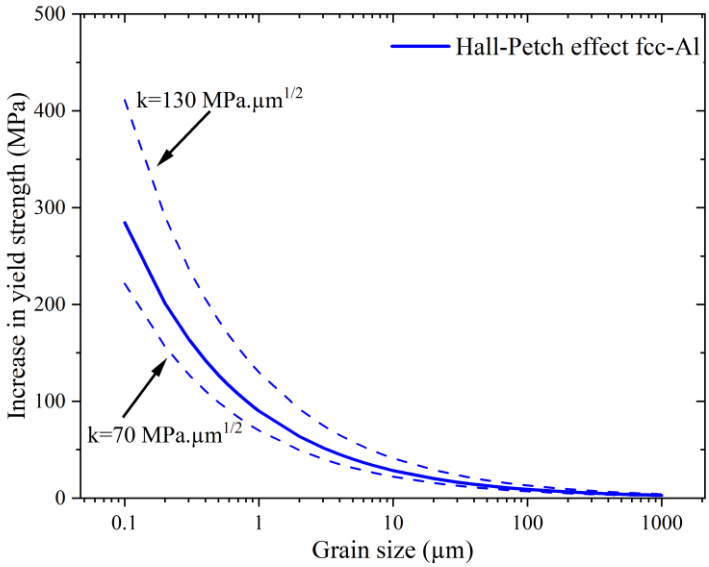

Figure 17 Grain size effect for fcc-Al, comparing the different ranges of Hall-Petch constant (between 70-130 MPa.µm$^{1/2}$) [63], [64]

3.2.3. Precipitation hardening

Precipitation hardening is arguably the strongest mechanism for strengthening Al-alloys. All the high-strength Al-alloys derive a large part of their strength from precipitates [45], [72], [73]. It is preferred to have a homogenously distribution and high amounts of fine and coherent precipitates for the best response. This can be achieved by first dissolving high amount of solutes in a solid solution and later causing precipitation via direct ageing heat treatments. Depending on the size of the precipitate, and its coherency with Al-matrix, the precipitate strengthening usually varies.

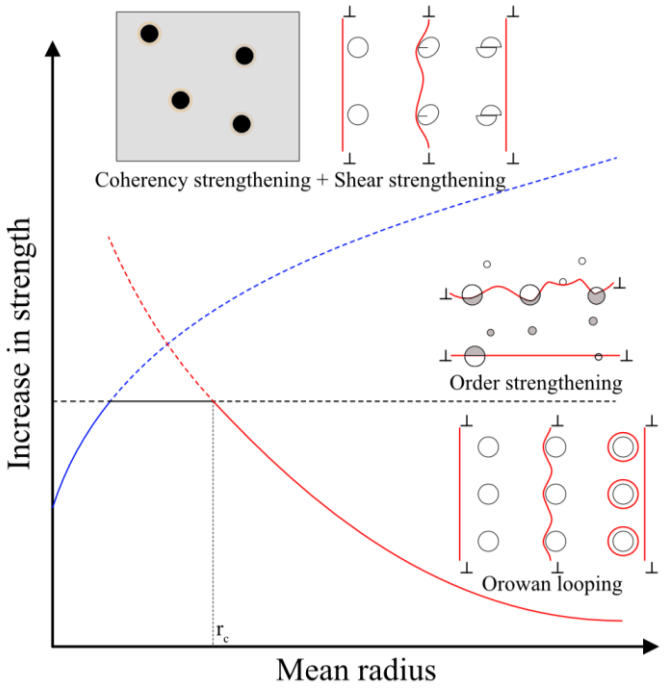

Figure 18 Summary of precipitation strengthening on aluminium alloys as a function of mean radius. Order strengthening effect is redrawn from [74]. Volume fraction is assumed to be constant

Figure 18 illustrates the strengthening effect created by each of the different precipitation mechanisms as a function of the mean radius. This effect is crucial for mostly Al_3Zr nanoprecipitates, which have a radius <10 nm during heat treatments. The lowest strengthening effect (solid line) is considered as the valid strengthening mechanism at the corresponding mean radius [75]–[77]. For very small radii (usually 1-2 nm), a combination of coherency + shear strengthening defines the strength from such precipitates. Above a certain radius, order strengthening becomes the controlling mechanism and this is independent of mean radius and rather controlled only by the volume fraction of precipitates. After a critical radius (r_c) is reached (usually around 3-5 nm), strength is defined by Orowan looping, which is inversely proportional to radius of precipitates.

Coherency strengthening [78] originates from the interactions between dislocations with the stress fields generated by coherent precipitates. It is proportional to the lattice misfit between precipitates and Al-matrix, radius and volume fraction. Shear strengthening (Nembach's shear hardening [79]) is caused when dislocations completely shear the precipitate. It is proportional to difference in shear modulus of precipitate and matrix, radius and volume fraction. Both these shear mechanisms are assumed to act together for small radii, as described elsewhere [75], [80]. For small radii, coherency and shear strengthening are defined by equations 3.4 and 3.5.

$$\Delta\sigma_{coh} = M\alpha_{\varepsilon}(G\varepsilon)^{\frac{3}{2}}\left(\frac{r.f_v}{0.18G\,b^2}\right)^{\frac{1}{2}} \quad [3.4]$$

In equation 3.4, M is Taylor's mean orientation factor = 3.06 [68], α_{ε} is constant for coherency strengthening = 2.6 [78], G is the shear modulus of Al = 25.4 GPa [69], ε is constrained lattice parameter mismatch (ε) between Al and Al_3Zr precipitates [75], [81], b is burger's vector for Al = 0.286 nm [69]. r and f_v represent the average radius (nm) and volume fraction of precipitates respectively.

$$\Delta\sigma_{shear} = 0.0055.M.(\Delta G)^{\frac{3}{2}}.\left(\frac{2.f_v}{G}\right)^{\frac{1}{2}}.\left(\frac{r}{b}\right)^{\left(\frac{3m}{2}-1\right)} \quad [3.5]$$

In equation 3.5, M is Taylor's mean orientation factor = 3.06 [68], ΔG is the difference in shear modulus between the matrix and the precipitate = 42.6 GPa [75], [82], G is the shear modulus of Al = 25.4 GPa [69], b is burger's vector for Al = 0.286 nm [69], m is material dependent constant for shear hardening = 0.85 [78]. r and f_v represent the average radius (nm) and volume fraction of precipitates respectively.

As precipitates reach a certain radius, the long-range order of some specific precipitates (such as $L1_2$-Al_3Zr nanoprecipitates) to the fcc-Al matrix strengthens it. The strengthening is derived when a dislocation shears an ordered precipitate, creating an anti-phase boundary in its glide plane [74], [78]. The maximum strength is when the dislocation has sheared through half the precipitate. This strengthening is proportional to anti-phase boundary energy and volume fraction. Equation 3.6 shows the strengthening effect of order strengthening.

$$\Delta\sigma_{Ord} = 0.81M\frac{\gamma_{APB}}{2b}\left(\frac{3\pi f_v}{8}\right)^{\frac{1}{2}} \quad [3.6]$$

In equation 3.6, M is Taylor's mean orientation factor = 3.06 [68], γ_{APB} is the anti-phase boundary energy for Al_3Zr = 0.455 J/m^2 [75], b is burger's vector for Al = 0.286 nm [69]. f_v represent the volume fraction of precipitates.

Upon longer heat treatments, precipitates start to coarsen and in some cases, lose coherency. In case of Al_3Zr nanoprecipitates, a phase transformation from metastable $L1_2$ structure to stable $D0_{23}$ structure could happen at long term heat treatments [83], [84]. When precipitates are larger, a relatively weaker Orowan looping becomes the main strengthening mechanism where, instead of a shearing route, dislocations "loop" around the precipitate to provide strength. This strengthening is proportional to volume fraction and $\frac{\ln r}{r}$ where r is radius, thus making it inversely proportional to radius. This mechanism is represented mathematically by equation 3.7.

$$\Delta\sigma_{Oro} = M\frac{0.4}{\pi}\frac{Gb}{\sqrt{1-v}}\frac{\ln\left(\frac{2r}{b}\right)}{\lambda} \quad [3.7]$$

In equation 3.7, $\lambda = \left[\left(\frac{3\pi}{4f_v}\right)^{\frac{1}{2}} - 1.64\right]r$, M is Taylor's mean orientation factor = 3.06 [68], G is the shear modulus of Al = 25.4 GPa [69], b is Burger's vector for Al = 0.286 nm [69], v is the Poisson's ratio for Al = 0.345 [68]. r and f_v represent the average radius (nm) and volume fraction of precipitates respectively.

To illustrate the coherency effect to strengthening, an example of conventional Al-4wt% Cu alloy is considered. A typical Al-4wt% Cu alloy is heat treated to 813 K to completely dissolve all the Cu in a solid solution followed by quenching in water. Then the alloy is heat treated at 453 K. Even though the equilibrium phase diagram suggests the formation of Θ ($CuAl_2$) phase, in reality, the precipitation sequence in these alloys observed is GP Zones → Θ'' (discs) → Θ' (plates) → Θ ($CuAl_2$) [45]. The reason is that directly forming the fully incoherent Θ phase has a large activation energy barrier due to high interfacial energy. This barrier may be overcome by heat treating at high temperatures as high as 573 K. However, for best hardening response,

at 453 K heat treatments, fully coherent (GP Zones) form due to lower activation energy barrier caused by low interfacial energy. This precipitation sequence also controls the peak strengthening in the alloys as the peak strength over ageing time is achieved from Θ'' precipitates and loss of strength is observed when phase transformation from Θ'' → Θ' occurs (corresponding to ~1 day of ageing at 463 K for Al-4wt% Cu) [85].

3.2.4. Dislocation strengthening

Dislocation strengthening is a relatively less known strengthening method for Al-alloys. It is prevalent in cold work/ extruded Al-alloys (3xxx, 5xxx series) where a high density of dislocations are generated by applying cold working that strain hardens the material to enhance the yield strength. The dislocation strengthening effect can be summarised as equation 3.8.

$$\Delta\sigma_{Dis} = M\alpha_1 Gb\sqrt{\rho_d} \quad [3.8]$$

In equation 3.8, $\Delta\sigma_{Dis}$ represents the increase in yield strength, α_1 is dislocation constant for fcc-Al [86], [87] = 0.3 and ρ_d is dislocation density in m^{-2}. The other constants are mentioned in previous sub-sections. Figure 19 shows the increase in strength with increasing dislocation strengthening.

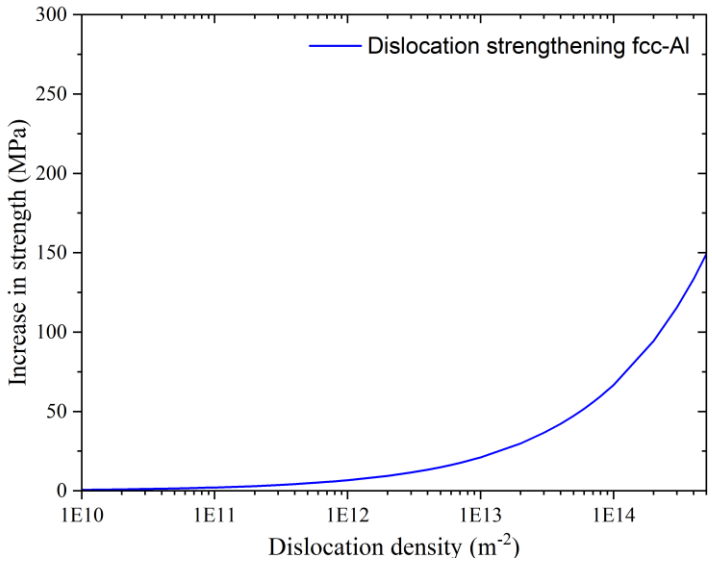

Figure 19 Dislocation strengthening effect on fcc-Al

Increased dislocation densities have been suggested to be one of the reasons for higher yield strengths in stainless steels processed by PBF-LB process [88], [89]. The process inherently adds residual stress to the material (mentioned in section 2.4.5) which could trigger an increase dislocation density. For Al-alloys, dislocation densities as high as $1*10^{14}$ - $5*10^{14}$ m^{-2} [90], [91] have been reported, even for PBF-LB materials. However, this effect is not considered to be significant by some researchers. Still, as shown analytically by Roters et al. [91], a two-phase Al-alloy (typically precipitation-hardened alloys) could have about two-three times higher peak dislocation densities in the deformed state as compared to single-phase Al-alloys (solid solution strengthened). This means that high dislocation densities could be worth considering as a contributing strengthening mechanism.

3.3. High performance in Al-alloys

The data in Table 2 show that a wide range of strength levels of Al-alloys exist. This means that for certain applications, strength alone is not the only deciding factor and thus secondary properties often define the use of Al-alloys. 5xxx or 6xxx series aluminium alloys are used in marine environments due to their general corrosion resistance even though they are not the strongest. Moreover, Cann et al. [92] mentioned that the use of Al-alloys can be expanded to replace electrical wires in long-range transport. Therein, a combination of strength at room temperature (RT) and high service temperature is needed for success. Finding a combination is hard as the high-temperature strength in Al-alloys is poor held after 473 K. Another category with high-temperature strength benefits could be to replace Fe- or Ti- alloys in aerospace applications due to the high specific strength of aluminium at room temperature [18]. At higher operating temperatures >473K, commercial Al-alloys does not meet the strength requirements thus leaving a large opportunity space to be filled as discussed before [46]. Based on the lucrative opportunities in aerospace structures and high thermal stability products (such as heat exchangers), this thesis study hence aimed at focusing on good RT strength (>450 MPa) combined with high-temperature resistance (up to 573K) as objective properties. An additional aspect of corrosion was also considered as part of alloy design but is not appended as part of this thesis study.

CHAPTER 4:
ALUMINIUM ALLOYS TAILORED FOR PBF-LB

Aluminium alloys for PBF-LB have been a field of growing interest for the last 10-15 years. Since the first research conducted on AlSi10Mg by Thijs et al. [93] in 2013, there has been an increase in demand for Al-alloys processed by PBF-LB. As of 2021, about 100 Al-alloys for AM were available [7]. However, most of these alloys are based on simply using cast-compatible Al-alloys (such as AlSi10Mg or AlF357) for printing using the PBF-LB process, having limited strength of ~400 MPa. These alloys perform better than their cast counterparts due to refined microstructures enabled via PBF-LB processing. This thesis study aims to better utilise the PBF-LB process to conceive novel chemistries which are compatible with the process to produce better strength and at the same time provide high-temperature stability as well as general corrosion resistance.

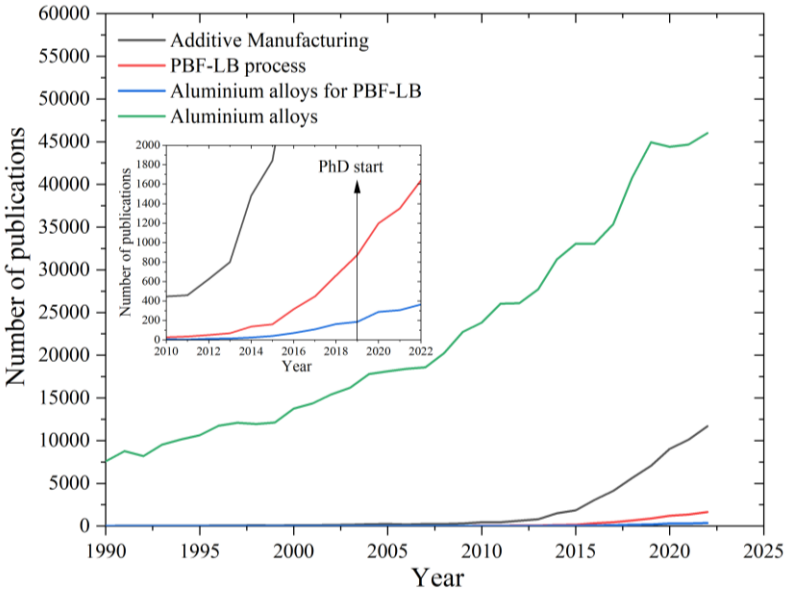

Figure 20 Scientific publications per year comprising of following topics in the title, abstract or keywords: Additive manufacturing, Aluminium (or Aluminum) and PBF-LB (or LPBF or L-PBF or MAM or LAM or SLM® or DMLS®). Data sourced from Scopus in April'2023.

As illustrated in Figure 3 and Figure 20, Al-alloys are heavily researched and there lies immense theoretical and experimental information from conventional and novel processing routes which could be leveraged to create new alloy systems. CALPHAD-based software packages such as Thermo-Calc have advanced over the last few years thus being capable enough to provide reasonable guidelines towards reaching a desirable alloy system. This chapter discusses in detail the alloy design approach that was chosen and the benefits/ limitations of the CALPHAD techniques employed. Eventually, the expected post-processing methods (i.e. heat treatments) were also included as a part of the alloy design. All of this was done as a part of the approach to reach desired performance for the studied alloys.

4.1. CALPHAD Approach

CALculation of PHAse Diagram (CALPHAD) approaches is based on computational thermodynamics. Since its inception [94], [95], it has become a commonly used method to utilise thermodynamic properties of various phases formed during processing or after post

processing treatments to predict the process-structure-property-performance aspect of multicomponent systems. Advanced software packages such as Thermo-Calc provide the possibility to do equilibrium assessments, solidification (using Scheil toolbox [55]) and precipitation simulations (PRISMA toolbox [96]) to name a few. These simulations, particularly for aluminium alloys can provide information for predicting the final properties of an imaginary multi-component system. Some researchers have successfully used these techniques for developing novel alloys, even for the PBF-LB process [97]–[100]. On the other hand, limitations to such software are that calculations cannot easily predict the effect of high cooling rates and couple with remelting effect during layer-by-layer deposition that is common in the PBF-LB process. Additionally, precipitation calculations cannot accurately account for the previously nucleated precipitates which could be formed on PBF-LB processing. Another major issue is the limited availability of thermodynamic databases associated with novel alloy systems. CALPHAD approaches were still considered beneficial to set a defined objective and provide direction. However, actual experimental results were deemed necessary to prove and characterise the outcome in this thesis study.

4.1.1. Integrated computation materials engineering (ICME)

Integrated computational materials engineering (ICME) is a relatively new field, which aims to shorten development cycles for future components while accelerating the development of new materials [101]. This is achieved by understanding the process-structure-property-performance relationship and applying advanced CALPHAD-coupled as well as machine-learning tools to predict resulting properties. Such methods rely heavily on modern computing capabilities, historical metallurgical data and most importantly, materials models that quantitatively describe the process-structure-property relationship. Figure 21 shows a simplified example of such a process-structure-property relationship chart which was applied in this thesis. The alloy system it refers to is the Al-Mn-Cr-Zr based system developed for the PBF-LB process.

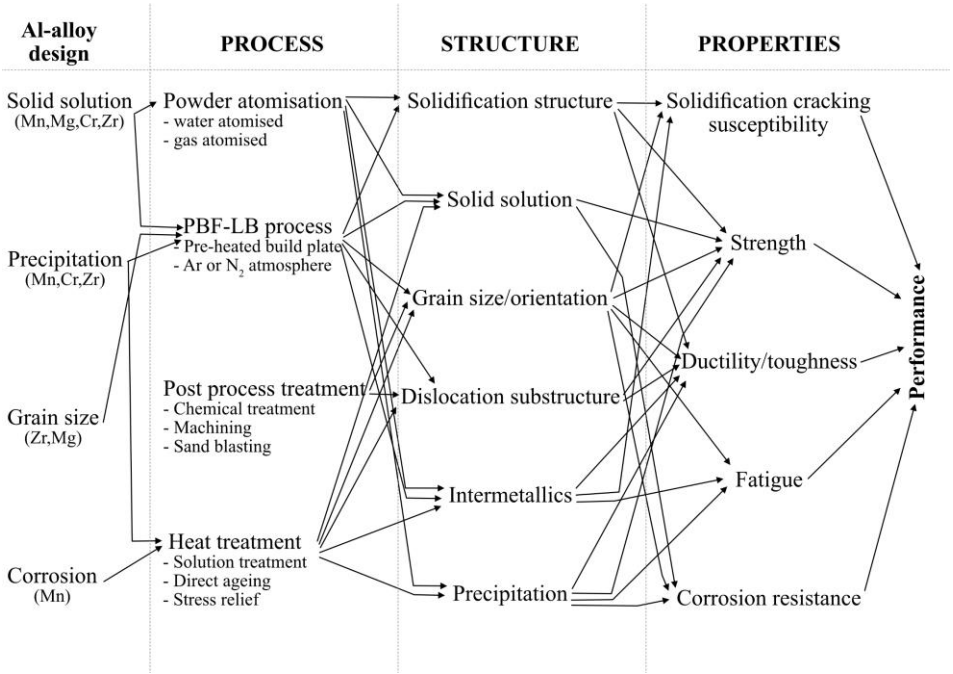

Figure 21 Simplified process-structure-property chart including alloy chemistry design for Al-Mn-Cr-Zr alloy system designed in this thesis work. Figure based on [38], [46]

4.2. Powder for the PBF-LB process

The PBF-LB process involves the use of spreading a thin layer of metal powder over the build plate, which is then selectively melted. This powder layer needs to have desirable characteristics to perform well for processing. Riabov [102] studied several aspects of powder characteristics and how it affects final part quality. Powder size distribution, sphericity, basic flow energy and break energy were among many factors that directly affected printability [103]. Thus it is important to have a good control over these properties. Most metal powder grades for the PBF-LB process are produced by the gas atomisation process, which is elaborated in the next section.

4.2.1. Atomisation process

Metal powder for PBF-LB is typically produced via a gas-atomisation process [104], [105]. Figure 22 shows a simplified version of such an atomisation process. In this process, molten metal is produced in an alumina crucible using an induction furnace, which is slowly released into an atomisation chamber via gravity. The molten metal is introduced in this large container via impingement of inert gases, typically N_2 or Ar, which breaks up the melt to form liquid metal droplets that solidify into metal powder under forced cooling. The resulting powder is then distributed into various sieve sizes based on the process requirements. For the PBF-LB process, this range is 20-53 µm or 20-63 µm for several materials.

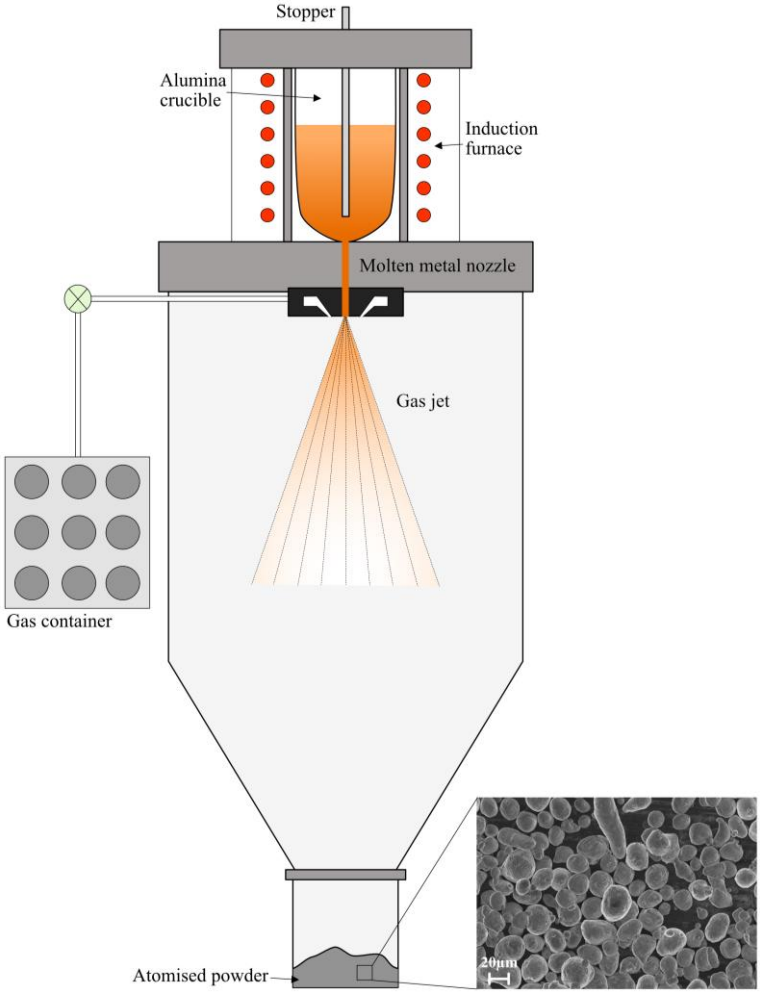

Figure 22 Schematic illustration for a typical gas-atomisation system and resulting powder. The powder image is Al-Mn-Cr-Zr based alloy. Redrawn from [104]

4.2.2. Powder specifications for PBF-LB

The metal powder after production from the atomisation process needs to have certain specifications to be suited for the PBF-LB process. Powder size distribution, packing density, and powder flowability are important to depict proper powder flow behaviour, which in turn affects the quality of the build. Usually, spherical powder is desired for optimised flow and packing density of the powder bed thus creating better-resulting properties [106], [107]. However, the more spherical powder produced by processes like vacuum induction melting inert gas atomisation (VIGA) costs more than other cheaper methods like water atomisation processes which produce a relatively non-spherical powder. Recently, research has been conducted on this topic [102], [106] to identify the role of powder size distribution, morphology, flow and the sphericity of the powder needed to be acceptable for the PBF-LB process wherein it was identified that lack of sphericity of the powder limits the maximum layer thickness achievable [102], [103].

4.3. Alloy design

4.3.1. Alloy design for atomisation and PBF-LB process

The atomisation process itself is often overlooked when alloy design for PBF-LB is considered. However, the atomisation conditions have a direct role in the resulting microstructure after PBF-LB processing. One example is cooling rates. Measuring dendrite arm spacing to measure the cooling rate with the formula shown in equation 4.1 which was shown in [108].

$$\lambda = \lambda_0 R^{-n} \qquad [4.1]$$

In equation 4.1, λ = secondary dendrite arm spacing (SDAS), λ_0 and n are material dependent constants and R is the cooling rate. Thus SDAS is inversely proportional to cooling rates. For Al-alloys, the atomisation process is seen to have cooling rates of 10^3 - 10^6 K/s depending on different atomisation conditions [108]. Figure 23a)-b) shows a dendritic-cellular solidification structure in the atomised version of an Al-alloy (Al-Mn-Cr-Zr) and a cellular-dendritic solidification structure in as-printed of the same Al-alloy. The solidification structure is much finer in the as-printed condition as compared to atomised condition (suggesting higher cooling rates), although some precipitates are formed upon the PBF-LB process, which is not seen in the as-atomised powder.

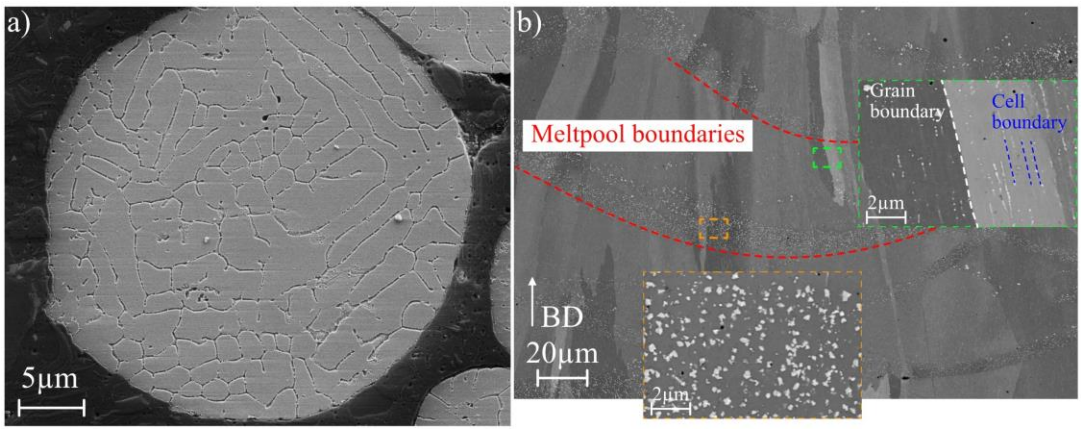

Figure 23 a) Cut section showing dendritic solidification in atomised powder of Al-Mn-Cr-Zr based alloy and b) As-printed microstructure with cellular solidification inside melt pool after PBF-LB processing in Al-Mn-Cr-Zr based alloy

As per [109]–[111], the rapid cooling rates induced by atomisation and the PBF-LB process provide a possibility to suppress the formation of primary intermetallic phases and reduce the chances of solute partitioning thus leading to increased solid solubilities. As shown in Figure 25a), this increase for Al-alloys becomes more prevalent in transition series metals (such as Mn, Cr, and Fe) wherein solid solubilities can be extended by one-two orders of magnitude. When this effect is combined with two more objectives, namely higher solid solution effect (Figure 25b)) and low bulk diffusivity (Figure 25c)), the resulting choice of elements can lead to alloy systems with high amounts of strength in as-printed conditions followed by slow, homogeneous precipitation upon post-processing heat treatments. Hence, Mn, Cr, and Zr were selected as possible alloying elements since they have about three times more solid solution potential than other commonly used alloying elements (Mg, Si, Zn, Cu) while having about five-six orders of magnitude slower bulk diffusivities making them lucrative for high-temperature applications. An additional grain size control was desired from the alloys, to induce the Hall-Petch effect and reduce the anisotropy which is common for PBF-LB processed materials [11]. Herein, as shown in Figure 25d), increasing the cooling rate does not only provide an increased solubility of Zr, but for higher amounts of Zr, it can suppress the formation of the stable $D0_{23}$ phase and instead lead to the formation of the metastable $L1_2$ phase. As per Griffiths [112], reduced interfacial energy combined with a structural factor to the interface energy is the reason which should favour this phase. More recently, Buttard et al. [113] have also argued that a liquid structure (namely icosahedral short-range order) plays a role in the nucleation of some of these primary $L1_2$ phases. However, this thesis study did not try to ascertain the reason for this effect further than identifying the limit of solubility beyond which Zr additions cause grain refinement and characterising it. Based on literature evidence and EBSD analysis, the primary $L1_2$ phases were characterised (see Figure 24).

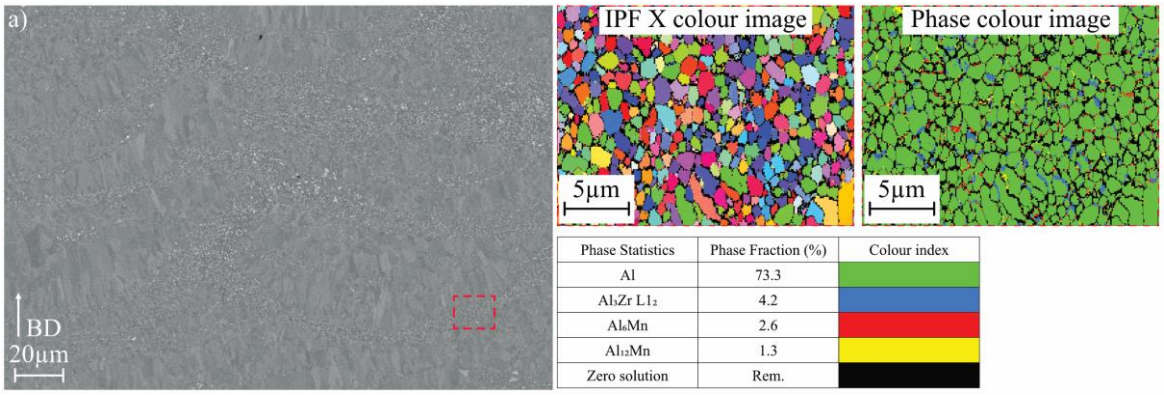

Phase Statistics	Phase Fraction (%)	Colour index
Al	73.3	
Al_3Zr $L1_2$	4.2	
Al_6Mn	2.6	
$Al_{12}Mn$	1.3	
Zero solution	Rem.	

Figure 24 a) Electron micrograph of Al-Mn-Cr-Zr based alloy with grain refinement and inset images show EBSD measurements at refined grain region showing only IPF X colour image and phase colour image. The Al_3Zr phase was characterised to be around 4%. Image for illustration purposes only

Another feature of this alloy design approach could tentatively contain general corrosion resistance due to fine precipitation and formation of protective oxide film [18]. This has been studied in collaboration with RISE, Stockholm in the H2020 MANUELA project (grant agreement no. 820774) but is not appended as a part of this thesis study. In summary, the PBF-LB process has inherent limitations, which affects this methodology of alloy design. The technique results in a moving melt pool with remelting happening layer-by-layer combined with scan rotation of laser. Thus, the resulting solidification structures formed upon deposition and remelting of previously deposited layers are different on a micrometre length scale [32],

[38], [39], [46], [114]. This means that alloy design needs to account for such variations. One way was by conservatively assuming the extended solid solubilities of elements such as Mn to avoid undesirable segregations during processing. Even though Figure 25a) suggests that this could be 7.5 at% (~15 wt%), only about 2.5 at% (5 wt%) was assumed as an extended solubility limit valid for PBF-LB. Such solubilities have been shown to work previously for the atomisation of Al-Mn-Cr powder [115], [116] and were thus considered compatible both for PBF-LB and atomisation.

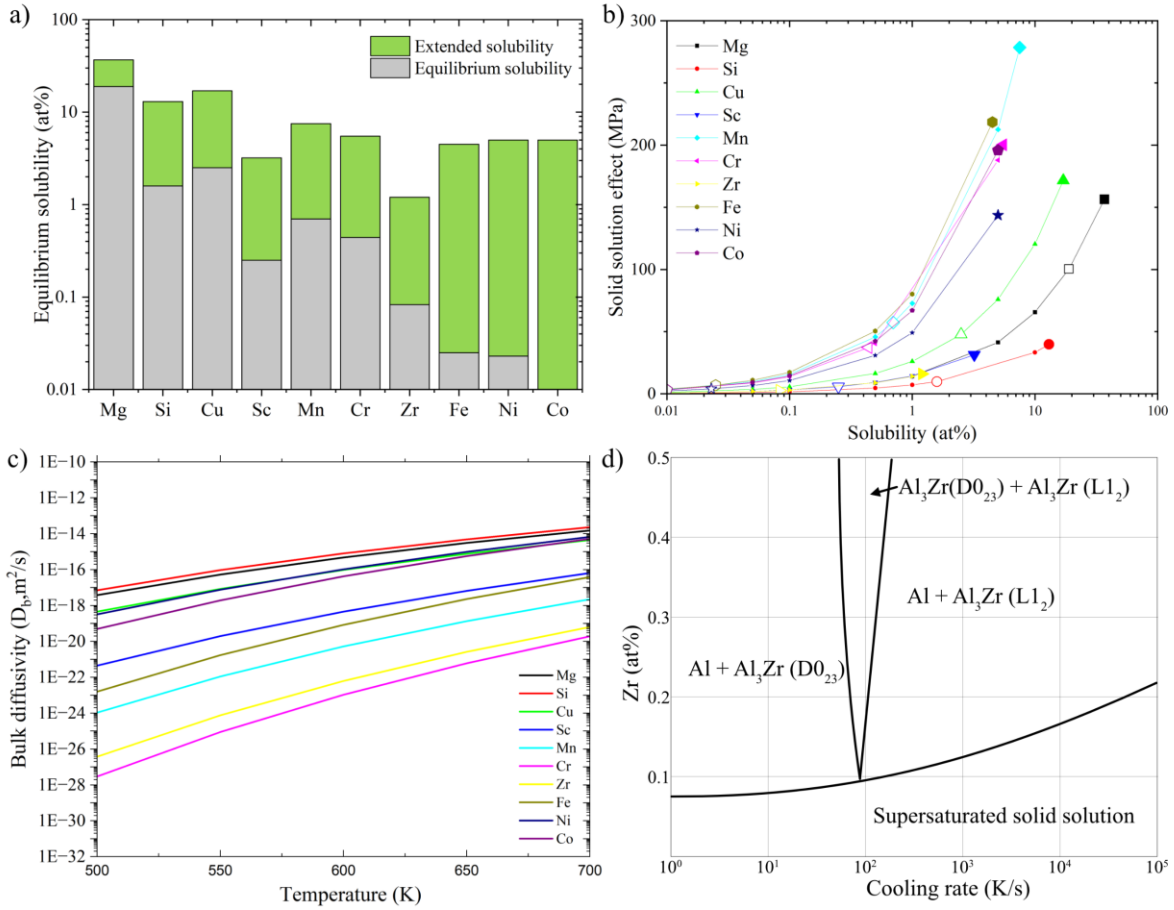

Figure 25 a) Extended solubility enabled with rapid solidification techniques [110], [117] b) Effect of extended solubility to solid solution effect of given elements. Empty markers and solid markers show the equilibrium and extended solubilities respectively [46], [67], [117] c) Bulk diffusivities of some elements in fcc-Al at temperatures between 500-700 K [46], [118], [119] d) Structural stability diagram for Al-Zr alloys showing stable tetragonal ($D0_{23}$ phase) and metastable ($L1_2$ phase) [112], [120]

4.3.2. Defect-tolerant alloy design

Alloy design for PBF-LB has another aspect which should be addressed i.e. alloys which are defect tolerant. Designing an alloy with the best possible property theoretically but containing severe cracking could significantly reduce the value creation aspect of PBF-LB. In this thesis study, defect tolerance was considered in two ways. One was the reduction of solidification cracks via in-situ alloying (*Paper I, II*) and ex-situ mixing (*Paper III*). Solidification cracking was resolved in alloys susceptible to cracking (containing Mg or impurities such as Fe+Si) via alloying with Mn, Cr (to reduce solidification range) or alloying with Zr. An approach to visualising the problem with two possible solutions is represented in Figure 26b). This approach is based on the method suggested by Sindo Kou [53].

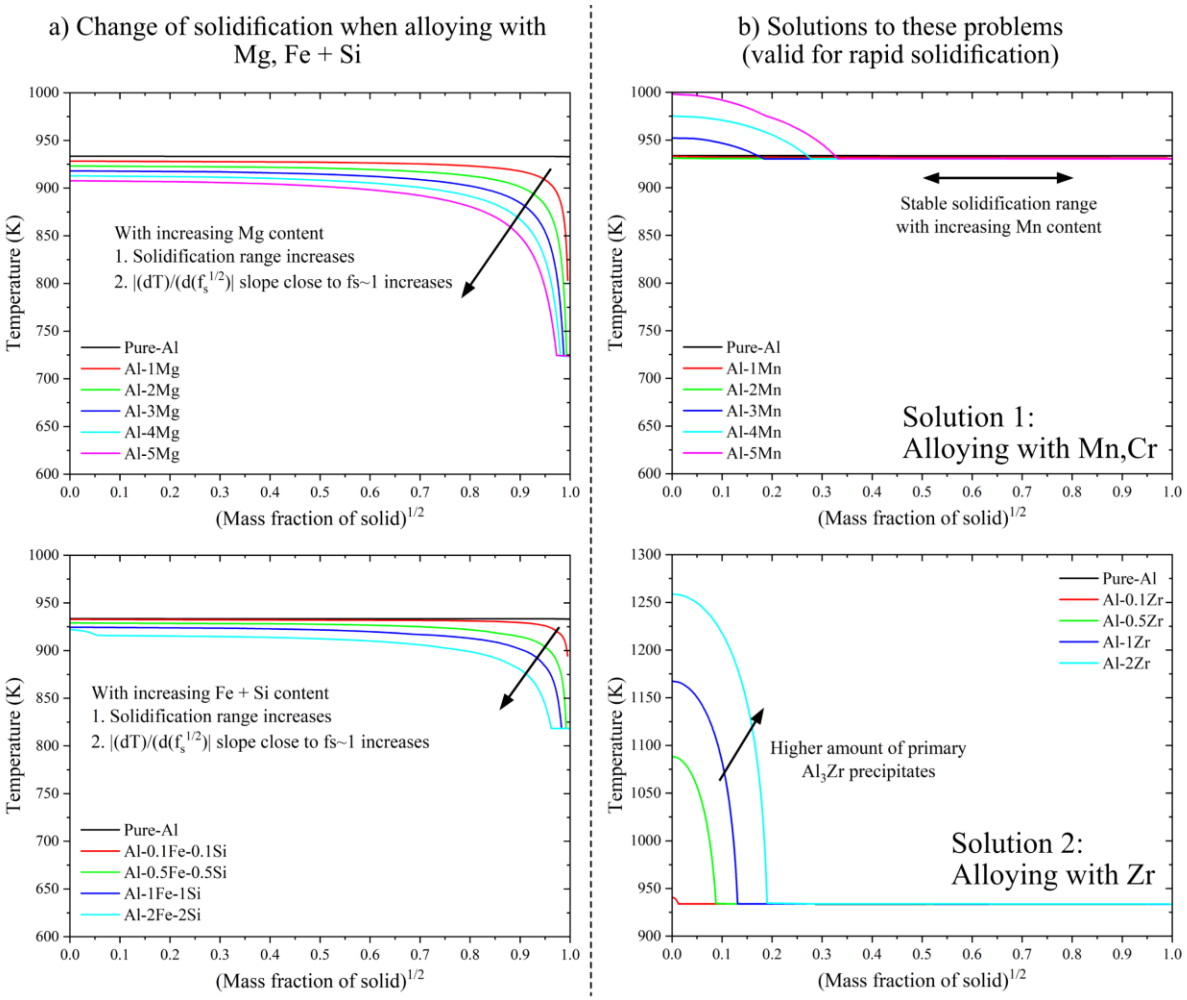

Figure 26 a) Increase in solidification cracking susceptibility when alloying with elements such as Mg or Fe+Si (found in impurities) b) Two possible solutions suggested to rectify the issue namely addition of Mn, Cr (solution 1) or addition of heterogeneous nucleation causing Zr (solution 2). All contents in wt% and calculations conducted using the Scheil module in Thermo-Calc 2022a

The other way defect tolerance was considered was to optimise processing parameters to achieve full density. An example is shown in Figure 27 wherein a processing window for an alloy is shown. At high power (170 W) and low speeds (500 mm/s), there is an extremely high amount of laser energy which leads to gas porosity due to evaporation of the material during processing. On the other hand, at low power (100 W) and high speeds (1250 mm/s), the laser energy is insufficient to melt the powder, thus causing a lack of fusion porosity. Overall, a region with reasonable energy is needed which can be balanced by combining different processing parameters, as was done in *paper I, paper II and paper V* for EOS M100 and EOS M290 machines at Chalmers.

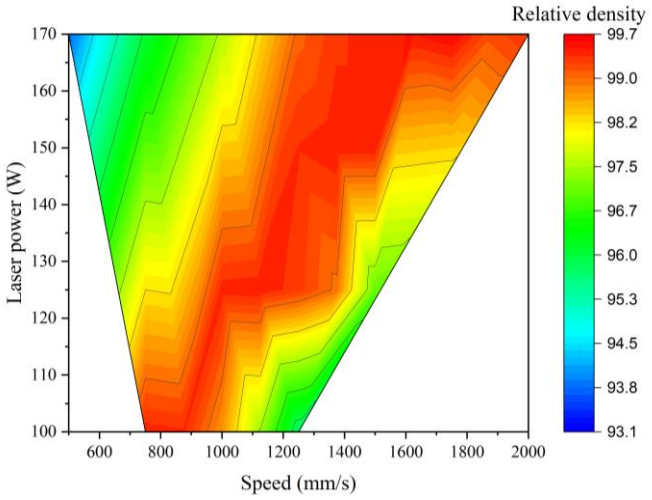

Figure 27 Typical processing window illustrating the relative density in the regions of interest with different laser power (W) and laser speed (mm/s). Processing window taken from Alloy C (Al-Mn-Cr-Zr) manufactured using EOS M100 machine. Redrawn from *Paper I* [48]

4.4. Resulting microstructure

During PBF-LB processing, the material is solidified in a shape of a hemisphere, which can be viewed in two dimensions with an image plane along the XZ plane. The cross-section created for this view when cutting along the building direction (XZ plane) has the appearance of multiple welds. The layer-by-layer processing of the material creates a repetitive structure wherein aluminium grains solidify and grow along the build direction. As seen in Figure 28, along the build direction, the repetitive structure layer-by-layer along the XZ plane becomes visible after etching. At the borders of the melt pools, i.e. the melt pool boundaries, a more pronounced formation of primary precipitates is seen (see Figure 29b)) owing to the change in local solidification and remelting conditions mentioned before. On the transverse direction (XY plane), several scan lines are visible, the width of which represents the melt pool width, and the length of these lines is set by the processing condition applied, i.e. for the case in question a stripe length of 7 mm is used.

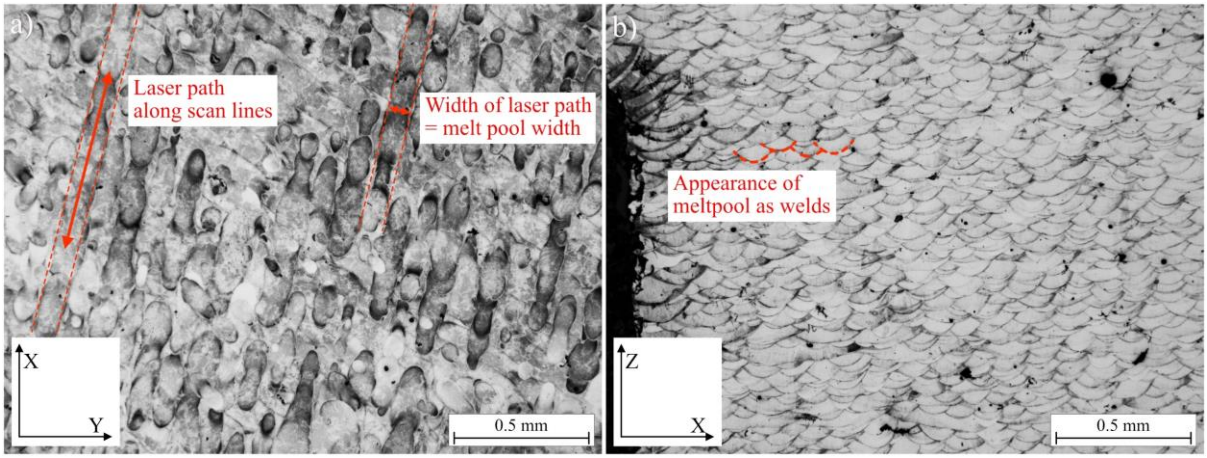

Figure 28 1)-b) Etched image of as-printed Al-Mn-Cr-Zr based alloy along XY and XZ plane respectively.

When examining the solidification microstructure closely, see Figure 29, it can be observed that the microstructure differs between melt pool boundaries and the surface of melt pools. This is due to different conditions enabled by the temperature gradient (G) and growth rate (R) in the two regions as elaborated before in Figure 8. Still, the Al-alloys experience columnar

growth along the build direction unless there are primary precipitates formed which can break this growth by heterogeneous nucleation of Al-grains, as illustrated in Figure 29b). These primary precipitates for the alloy system studied, $L1_2$ type Al_3Zr precipitates refine grain size and reduce the anisotropy in the as-printed material.

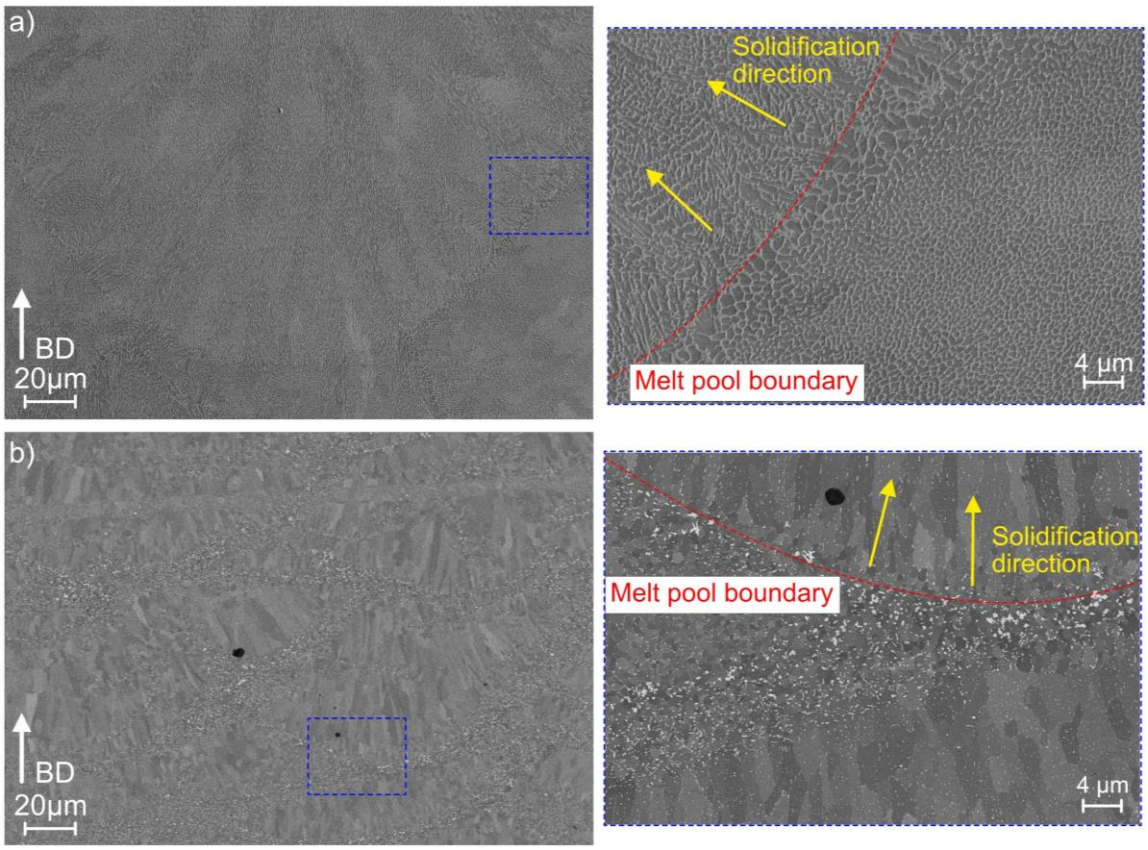

Figure 29 a)-b) As-printed microstructure of AlSi10Mg and an Al-Mn-Cr-Zr alloy respectively. The insets show the formation of melt pool boundary and solidification direction of fcc-Al

Further investigation of the microstructure reveals different observations depending on the alloy system studied. A comparison was done between the AlSi10Mg alloy with one of the Al-Mn-Cr-Zr variants, see Figure 29. In as-printed conditions, AlSi10Mg consisted of eutectic Al-Si intertwined networks [22], [36] with different sizes depending on solidification condition, examples provided in Figure 29a). For Al-Mn-Cr-Zr alloy variants as for 7017 Al-alloy, there were two types of visible precipitates seen namely at the melt pool boundaries and the solidification boundaries. The precipitates at melt pool boundaries, as mentioned in section 2.3.4 are suggested to form as a consequence of the re-melting of each layer. The re-melting pushes out solutes from the supersaturated solid below thus forming primary precipitates. The second category, precipitates at solidification boundaries (such as cell boundaries or grain boundaries), as mentioned in section 2.3.2 are potentially precipitates formed despite rapid solidification and cooling conditions. Some of them are low melting precipitates rich in Fe, Si seen in 7017 Al-alloy [121]. For the Al-Mn-Cr-Zr alloys, the characterisation of these precipitates could only reveal that they are Mn-rich (or Cr-rich), but their crystal structure was not successfully characterised yet due to their small sizes. Future work is ongoing with high-resolution TEM combined with advanced crystallographic mapping that will shed light on their crystal structure (not appended in this thesis).

4.5. Post-processing heat treatments

4.5.1. Direct ageing heat treatments

The common heat treatment of the high-strength Al-alloys involves a two-stage procedure, referred to as T6 [13], [60], [122], see Figure 30. This involves a first solutionising stage wherein the material is heated up close to the eutectic melting temperatures for the alloy system in question to dissolve low melting phases (such as Al-Fe precipitates) and to dissolve some elements into solid solution (such as Cu, Mg). This stage is followed by quenching in a cooling medium (usually water or oil) to quench-in the solutes in Al-matrix. Then follows the second stage, the ageing heat treatment at elevated temperature to trigger the homogenous precipitation of nanometric secondary phase precipitates creating the precipitation hardening effect. This two-stage approach is less relevant to precipitation-hardened Al-alloys that are tailored for the PBF-LB process. The reason is that the alloy design includes solutes often added beyond their solubility limits. Heating to solutionising temperatures will instead lead to coarse harmful precipitates instead of the dissolution of solutes. Additionally, manufacturing via PBF-LB creates a quenched-in state in terms of high dislocation density and fine microstructures [23], [90]. Consequently, direct ageing without any intermediate solutionising is considered better. At temperatures of 500-550 K, stress relief may be conducted for a few hours to remove the quenched-like state before ageing [27]. Such treatment could hence remove residual stress from the material for better machining tolerances. Depending on the alloy system, this temperature may be insufficient for causing precipitation hardening at the same time. For materials such as Al-Mn-Cr-Zr alloy variants developed in this thesis study as well as Al-Mg-Sc-Zr (Scalmalloy®), direct ageing at temperatures >573 K were conducted to reach peak hardening. However, as per manufacturer recommendations, materials like AlSi10Mg and Al7017 are heat treated using T6-like heat treatment wherein the solutionising step is shortened to 1-2 h instead of 6-8 h [27], [121]. In either case, novel heat treatments are necessary to reach peak strengths for PBF-LB materials and optimise the time for the heat treatment.

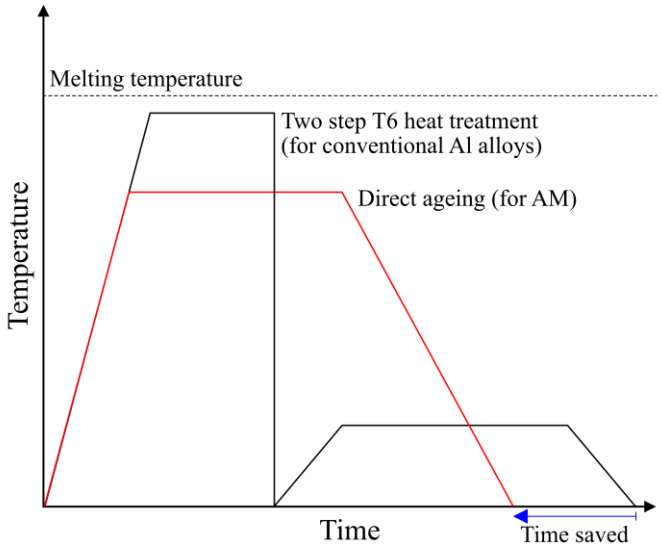

Figure 30 Conventional T6 type heat treatment used for conventional Al-alloys (black) compared to direct ageing heat treatment for Al-alloys for AM (red)

CHAPTER 5:
MATERIALS AND METHODS

5.1. Materials

5.1.1. Al-Mn-Cr-Zr based alloy system

All six variants of this alloy system were provided by Höganäs AB, Sweden. The powder was nitrogen gas-atomised and was sieved to a particle size of 20-53 µm. The chemical composition of all six alloys in an as-printed state is provided in Table 3.

Table 3 Alloy composition as per ICP-OES technique. All compositions are in wt%. Fe and Si are considered impurities

Alloy name	Alloy composition	Reference
Alloy A	Al 4.7 Mn 0.48 Zr 0.16 Fe 0.16 Si	[48]
Alloy B	Al 4.8 Mn 0.8 Cr 0.18 Fe 0.17 Si	[48]
Alloy C	Al 5 Mn 0.8 Cr 0.6 Zr 0.16 Fe 0.17 Si	[48]
Alloy D	Al 4.7 Mn 0.8 Cr 1.2 Zr 0 Mg 0.13 Fe 0.21 Si	[123]
Alloy E	Al 4.7 Mn 0.8 Cr 0.7 Zr 1 Mg 0.16 Fe 0.21 Si	[123]
Alloy F	Al 4.8 Mn 0.9 Cr 1.1 Zr 1.2 Mg 0.19 Fe 0.20 Si	[123]

5.1.2. Al-7017 + Zr + TiC

This was a special Al-alloy powder provided by EOS Oy, Finland. The powder was prepared by taking Al-7017 powder (20-63 µm standard size) mixed with 3 wt% Zr powder + 0.5 wt% TiC powder. The three powder variants were combined by a process of dry mixing and the final chemical composition of the alloy in the as-printed state is provided in Table 4

Table 4 Composition of Al-7017 alloy studied as per ICP-OES technique. All compositions are in wt%. The content of other metallic elements was <0.05% each and 0.25% total

Alloy	Alloy composition	Reference
Al-7017 + 3 wt% Zr + 0.5 wt% TiC	Al 4.4 Zn 2.3 Mg 0.45 Si 0.4 Fe 0.23 Mn 0.01 Cu 3.1 Zr 0.49 Ti	[121]

5.1.3. Al-Mg-Sc-Zr alloy (Scalmalloy®)

The powder was provided by Höganäs AB, Sweden. Powder size distribution was between 30-70 µm size [124]. The chemical composition of the alloy in the as-printed state is provided in Table 5

Table 5 Composition of Al-Mg-Sc-Zr alloy studied as per ICP-OES technique. All compositions are in wt%. Fe and Si are considered impurities

Alloy	Alloy composition	Reference
Al-Mg-Sc-Zr	Al 4.3 Mg 0.7 Sc 0.27 Zr 0.48 Mn 0.13 Fe 0.06 Si	[124], [125]

5.1.4. AlSi10Mg

This alloy is one of the most common Al-alloys available for the PBF-LB process. It was produced via gas atomization and 25-70 µm size. The powder was purchased from EOS GmbH, Germany. The chemical composition of the alloy is provided in Table 6

Table 6 Composition of AlSi10Mg alloy studied as per ICP-OES technique. All compositions are in wt%

Alloy	Alloy composition	Reference
AlSi10Mg	Al 9.8 Si 0.33 Mg 0.15 Fe	[27]

5.2. Powder bed fusion-laser beam process

All of the materials were processed using either the EOS M100 (EOS GmbH, Germany) or the EOS M290 (EOS GmbH, Germany). The EOS M100 machine at Chalmers University of Technology was used for producing samples of Al-Mn-Cr-Zr based alloy and Al-Mg-Sc-Zr alloy for *Papers I, IV, V, VI, VIII and IX*. The EOS M290 machine at Chalmers University of Technology was used for producing Al-Mn-Cr-Zr based alloys for *Papers II, VII and X*. An EOS M290 machine at EOS Oy, Finland was used for producing Al-7017 based alloy for *Paper III*. Some technical data for the two machines used for manufacturing is provided in Table 7. When producing all of the components in any machine, Ar as shielding gas was used to keep oxygen levels <0.1% (<1000 ppm).

Table 7 Technical data for EOS M100 and EOS M290 machines

	EOS M100	EOS M290
Build volume	Cylindrical d 100 mm x h 95 mm	w 250 mm x d 250 mm x h 325 mm
Laser power	170 W nominal	370 W nominal
Laser diameter	40 µm	85 µm
Build plate pre-heating	Not possible	Up to 200 °C
Powder feed	Gravity feed	Push feed

Process development to achieve fully dense samples was conducted for Al-Mn-Cr-Zr alloys in *Papers I and II* using EOS M100 and M290 machines respectively. For Al-Mg-Sc-Zr alloy, similar experiments were conducted for *Paper V* using the EOS M100 machine. For EOS M100 machine runs, a full factorial DOE was conducted on several alloys varying the laser power, laser speed and hatch distance. For EOS M290 machine runs, a simpler DOE was employed by varying the laser power and laser speed only. More details are provided in results section.

5.3. Sample preparation

5.3.1. Sample designs

Based on work by Pauzon [8], the test coupons were designed with a notch to mark the gas flow direction, as shown in Figure 31. This enabled the study of three cross sections (XY, XZ and YZ) in *Paper I* to verify if there is any effect of gas flow on relative density. Additionally, the notches were useful for locating the sample edge for microstructural studies when using electron microscopy. Sample designs were either cubic with 10 mm side or rectangular with 16 mm height, 8 mm length and 8 mm width.

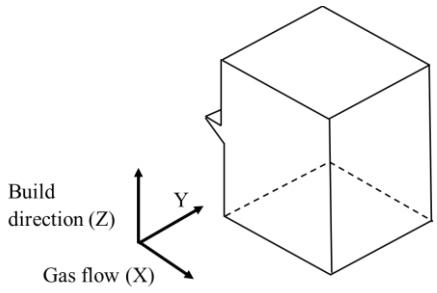

Figure 31 Sample with notch for manufacturing cubes for microstructural studies [48]

5.3.2. Metallography

Depending on the analysis to be conducted, several planes were studied. For DOE samples to measure density, all three XY, XZ and YZ planes were studied for samples produced in EOS

M100 machine and XZ, and XY planes were studied for samples produced in EOS M290 machine. For heat-treated samples, only XZ and XY planes were characterised. The samples were cut using a precision saw and mounted on polyfast resin (from Struers, Denmark). The samples were ground and polished based on a self-developed procedure. The procedure can be found elsewhere [46], [48], [126]. It can be summarised as follows

- Grinding of samples starting with SiC-foil #240 or #320 to make the samples flat
- Grinding progressively with finer grit foils till SiC-foil #4000
- Polishing with 1 µm diamond paste with 20 N load 3-5 min and 15 N 3-5 min
- Final polishing with OP-S suspension 15 N 1-2 min (with suspension) and 15 N 2 min with water only

Etching of aluminium samples was not needed for revealing microstructure as back-scatter mode was used for most electron microscopy analyses with good results. OP-S suspension provides slight etching too. Selected samples were chemically etched for optical microscopy for which Keller's reagent was used. The recipe was comprised of 95 ml water, 2.5 ml HNO_3, 1.5 ml HCl and 1 ml HF. Etching was conducted by directly dipping the sample into the etchant for 8-10 s followed by dipping in water and then cleaning with ethanol. The samples for transmission electron microscopy (TEM) were prepared by preparing thin foils (0.1 mm) along the XZ plane of the sample followed by punching to discs of 3 mm diameter. These discs were then twin-jet electropolished using Struers Tenupol 5 machine with freshly prepared Struers A2 electrolyte at 243 K and 15V. The samples for synchrotron studies were prepared using plasma focused ion beam (FIB) using a Xe+ ion at TESCAN, Czech Republic. Plasma FIB was used to avoid grain boundary contamination of the aluminium, which is common in conventional Ga-FIB [127], [128]. The as-printed samples were polished along the XZ plane up to the mirror finish (1 µm polishing step). This was then followed by the FIB lift-out produced using a TESCAN AmberX plasma-FIB SEM at TESCAN, Czech Republic.

5.4. CALPHAD simulation and precipitation modelling

The simulations conducted for alloy design and simulation of possible precipitation response were conducted using Thermo-Calc software provided by Thermo-Calc software AB, Sweden. For the thesis, Thermo-Calc 2019-22 versions of the software were used depending on the latest version available. The material databases for aluminium alloys were TCAL6-8 databases [100] from Thermo-Calc AB and COST507 open CALPHAD database [129]. For precipitation modelling calculations, mobility databases MOBAL5-6 were used. The use of these simulations has been limited to act as a guide to alloy design due to the unavailability of studied thermodynamic databases (Al-Mn-Cr-Zr based) and the limited development of non-equilibrium reactions. *Paper VIII* elaborates on the benefits of having a database explaining the effects of Cr on Mn-rich precipitates which could not be done with available TCAL databases.

5.5. Heat treatments

All the heat treatments at >523 K were conducted in a pre-heated resistance coil furnace with a secondary thermocouple close to the sample (<5 mm) to ensure temperature control within ±2 K close to the sample. The heat treatments at <523 K were conducted in a convection-heated oven with a similar setup for a secondary thermocouple to ensure temperature control.

5.6. Materials characterization techniques

5.6.1. Optical microscopy

Light optical microscopy (LOM) analysis was conducted on a ZEISS Axioscope 7 instrument. The microscope is equipped with an automated stage that can capture stitched images of larger sample sections. For large-area analysis to measure the relative density of samples, a 10x optical zoom was used, providing a resolution of 0.4 µm/pixel. This resolution could resolve defects up to ~1 µm (~6 pixels) with reasonable accuracy. The image analysis to obtain relative density was conducted using ImageJ V1.52a. The stereo optical microscopy (SOM) analysis was conducted on a ZEISS stereo discovery.V20 microscope. The SOM was used for the fractography of specimens from tensile and bending fatigue testing.

5.6.2. Scanning electron microscopy

Scanning electron microscopy (SEM) is a characterization technique that can help to study the structure of materials at several length scales. Based on which electron imaging is being done, the contrast could reveal information about the material [130]. For this thesis, backscatter electron (BSE) imaging was employed primarily. The benefit of BSE imaging is that atomic contrast can be seen as grey contrast of images.

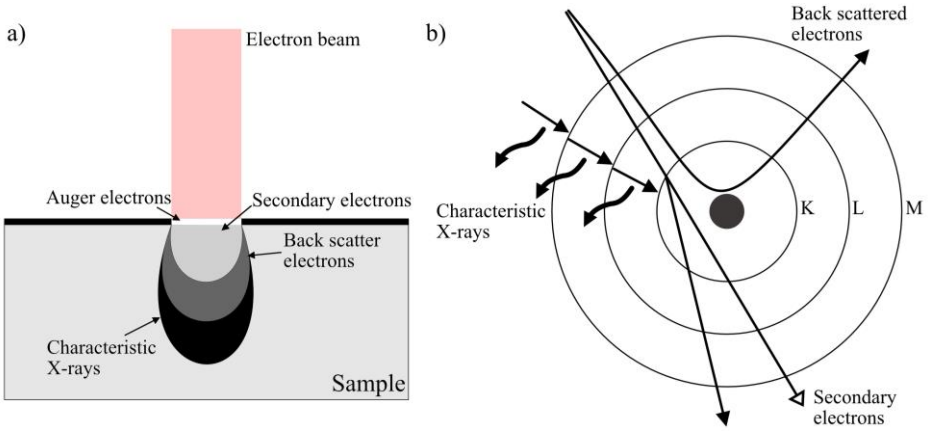

Figure 32 a) Schematic of interaction volume created by electron beam and b) Atom-high energy electron interactions with inner electron shells labelled as K, L and M respectively. Adapted from [130]

Depending on the different phases formed in the aluminium samples during PBF-LB processing or post-processing heat treatments, these phases were classified by using this grey contrast. This was achieved by using the BSE imaging coupled with electron dispersive X-ray spectroscopy (EDS) to facilitate feature analysis for precipitation analysis in the SEM. EDS is a technique which analyses the characteristic X-rays to study the chemical composition of a given point, line or area. It can be used as a method to quantify the amount of solutes in a certain precipitate or matrix. The limitation is the size of the interaction volume generated by the electron beam or the number of counts received by the detector (see Figure 32). A higher beam voltage creates higher counts for better analysis but reduces the spatial resolution of the detected feature due to larger interaction volume from electron beam. In this thesis study, ULTIM MAX EDS detector from Oxford Instruments was employed with a Zeiss Gemini 450 FEGSEM. Using this detector at high probe current (1 nA) with AZTec software, it was possible to generate relatively high count rate (6000-8000 cps) at low beam voltages of 4-5 kV to detect instead Lα peaks for features of interest, thus making it possible to assess precipitates

of 100-150 nm thus enhancing spatial resolution. The SEM was equipped with a six-channel BSE detector, which enabled better discrimination between the low atomic number Al matrix as compared to higher atomic number Mn-rich or Zr-rich precipitates. As shown in [131], such contrast was then leveraged for semi-quantitative analysis. Feature analysis is a tool provided within the Aztec software package, which couples large area stitching of several images and combining with EDS point scans of specific regions of interest (ROIs). By carefully controlling the settings and after several iterations, a working method was created [126] to identify two different precipitate classes ($Al_{12}Mn$ or Al_6Mn) based on differences in their grey contrast. This method was employed combined with EDS analysis at lower resolution (130 nm) in *Papers VI, IX* and for morphology-only analysis at even higher resolutions (30-40 nm) in *Papers II, IV, VIII*. The overall approach enabled large-area analysis of precipitates to do a semi-quantitative analysis of their sizes and in some cases, their tentative chemical compositions.

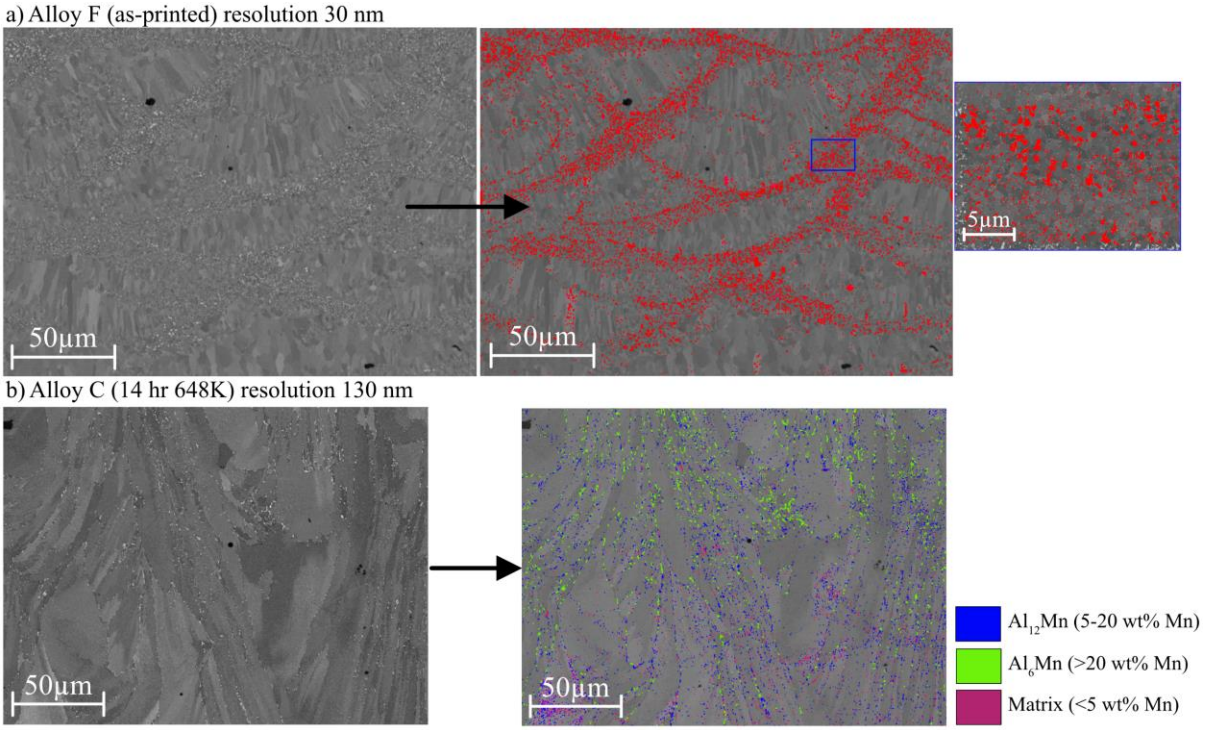

Figure 33 Feature analysis summary a) Alloy F as-printed with a resolution of 30 nm to study the morphology of precipitates. Blue insets represent the detection of fine melt pool boundary precipitates b) Alloy C heat treated at 648K 14 hr with a resolution of 130 nm to enable chemistry analysis. Thresholding limits are mentioned for three classes of precipitates. The matrix class of precipitates were ignored from calculations. Adapted from *Paper VI* [126]

The electron back-scatter diffraction (EBSD) is a technique where backscatter electrons interact with the crystal and form different diffraction cones for each lattice plane. The interaction of these cones on a phosphor screen is seen as a pair of parallel lines called Kikuchi bands [132], [133]. These Kikuchi bands provide information about the crystallographic structure of a local area and can be used for phase analysis, texture analysis, etc. EBSD measurements were conducted on freshly polished samples at 10 kV, 15 nA settings using a Symmetry CMOS EBSD detector from Oxford Instruments on the Gemini 450 FEGSEM. In this thesis study, the application of EBSD was limited to the study of Al-Mn-Cr-Zr based alloy system for studying the general microstructure of Al, particularly the grain refinement effect

induced by Zr addition beyond solubility limits and some phase analysis of different Mn-rich phases, see *Paper II, IV, VIII* and *IX*.

5.6.3. Transmission electron microscopy

Transmission electron microscopy (TEM) was conducted at CMAL (Chalmers Materials Analysis Laboratory) at Chalmers University of Technology. In both *Paper VI* and *Paper X* wherein TEM is utilized, Al-Mn-Cr-Zr based alloys were studied. For *Paper VI*, the samples were analysed using a probe-corrected Titan 80-300 kV TEM with a C2 aperture size of 70 µm and spot size 6. For *Paper X*, the previous TEM was used together with Tecnai T20 at 200 kV with imaging in bright-field mode.

5.6.4. X-ray fluorescence at synchrotron facilities

X-ray fluorescence is a technique which has similar characteristics to EDS. Hard X-rays are used and raster scanned on the region of interest wherein a K- or L-shell electron is captured into the XRF detector (usually energy dispersive detector) [134]. This information can be fine-tuned with a small spot size of an X-ray beam (50-60 nm) combined with better detectors (annular Rococo detector [135]) and higher energy X-rays to provide elemental information in a pixel of 50 nm x 50 nm in ng/cm^2. A simple schematic for XRF is shown in Figure 34.

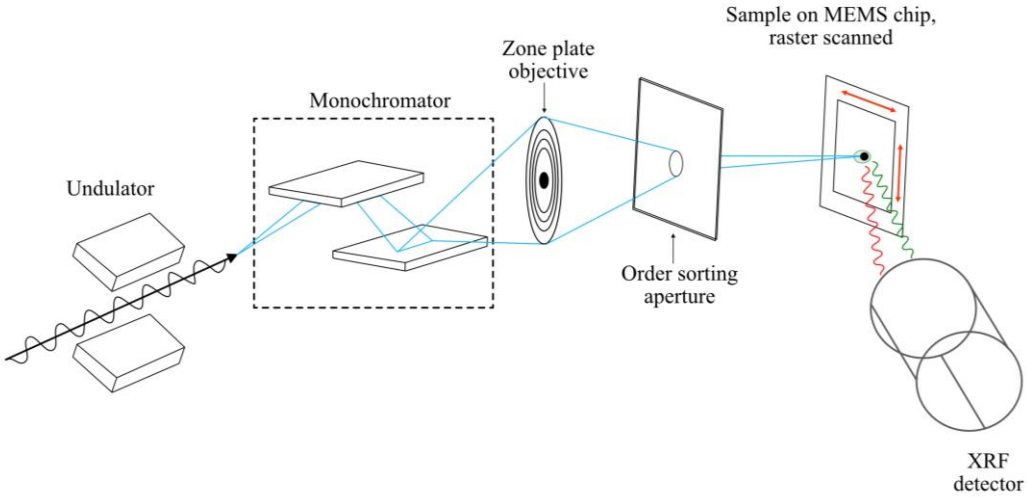

Figure 34 Schematic for XRF conducted at synchrotron facilities. Figure adapted from [134], [136]

Paper VII used this measurement technique to understand precipitation mechanisms in the Al-Mn-Cr-Zr alloys. The samples for these experiments were taken from Al-Mn-Cr-Zr based alloys and were prepared using plasma-FIB as explained before. After preparation, samples of 30 µm x 10 µm x 1µm were placed on a MEMS chip from DENS Solutions, The Netherlands with Pt deposition at the edges of the lamella. These Pt markers were used to stick the samples on the chip and used as a locator during XRF measurements. The samples were then placed in a nanoreactor at the P06 beamline at PETRA III, DESY Hamburg, Germany. The nanoreactor cell enabled a controllable heating/cooling of the chip together with a controlled environment (in this case N_2 was used) [137]. During the experiments, heat treatments at controlled heating and cooling rates of 15-20 K/min and 45-50 K/min respectively were used to avoid sample damage. The samples were exposed to 648 K temperature for up to 24 hours, wherein the heating was stopped and samples were cooled to room temperature at 4, 8, 14, 16 and 24 hours of heat treatment respectively to take higher resolution scans across the whole lamella. Three

types of scans were conducted, two of which were at heat treatment temperatures (648 K), and one was at room temperature (298 K). The ones at high temperatures were an "on-the-fly" rapid scan at 150 nm step size, exposure time 20 ms. The other was a region of interest (ROI) scans at 50 nm step size and 120 ms exposure time. The ROI scans were conducted at the melt pool boundary and close to a developing grain boundary in the size of 5 µm x 5 µm areas. After cooling the samples, the whole lamella was scanned at 50 nm step size and 30 ms exposure time to take a snapshot of heat-treated microstructure at that condition. *Paper VII* discusses the setup, methodology used and initial results of in-situ precipitation from such lamellas. More work has been conducted at other beamlines with a similar setup and method, which is currently under analysis and would be part of future work.

5.6.5. Synchrotron X-ray computed tomography

Synchrotron X-ray computed tomography (SXCT) is a tomography technique that provides volumetric information of a sample and can detect defects via difference in densities through a small sample, in a non-destructive way. In addition, the sample can be placed on a rotating stage to record projections that can be stitched together to provide a 3D reconstruction of the object. The contrast in the sample is dependent on the attenuation of X-rays passing through the object, which depends on the density and atomic number. Thus, for Al-alloys, defects (such as pores) with low density and precipitates (such as Zr-based) with high density can be distinguished via grey contrast. The SXCT was conducted on samples of 1.1 mm x 1.1 mm cuboid and testing was conducted at BAMline, BESSY II (Berlin, Germany) with results presented in *Paper III*. The energy of the monochromatic X-ray beam was set to 30 kV with an effective pixel size of 0.44 µm. In-situ tensile testing combined with SXCT was conducted on a DEBEN 5kN load rig installed on a rotation table. Thin flat tensile bars with 8 mm x 3 mm section were scanned with an X-ray beam set at 40 kV and the scanning was conducted after that nominal load was reached and stress relaxation was ended. The setup for SXCT and in-situ tensile testing can be found in [121], [138].

5.6.6. X-ray diffraction

X-ray diffraction (XRD) is a commonly used technique in materials science. Incoming X-rays irradiate the specimen with varying angles of incidence, and they are subsequently diffracted following Bragg's law. These diffracted X-rays are studied to provide inter-planar spacing (d), depict crystal structure, phase amount etc. Bragg's equation is shown in equation 5.1.

$$n\lambda = 2d \sin\theta \qquad [5.1]$$

In equation 5.1, n is the diffraction order, λ is the wavelength (Å), d is inter-planar spacing (Å) and θ is the incidence angle. The XRD experiments were conducted at Höganäs AB, Sweden using a Bragg-Brentano HD X-ray machine with Cu source (Kα =1.5406 Å) with 0.007° step size and 1 s scan step time. The XRD analysis was conducted in *Papers I, II, IV, VI and X*. This provided information on the solid solution effect and the assessment of possible phases formed during printing and after heat treatments.

5.6.7. Chemical analysis

Inductively coupled plasma-optical emission spectroscopy (ICP-OES) was conducted for Al-Mn-Cr-Zr, Al-Mg-Sc-Zr alloys by Höganäs AB, Sweden and AlSi10Mg and Al7017 by EOS

Oy, Finland. In this process, argon plasma at high temperatures (>5000 K) is generally used for ionizing a given sample, creating a characteristic emission spectrum for each element and thus revealing the amount of each element [139]. The limitation of this technique is that combustion at 5000 K is agnostic to the formation of precipitates etc., hence the information cannot reveal differences in microstructure within the material.

5.7. Mechanical testing

5.7.5. Hardness testing

Hardness testing depicts the resistance of a given material against a diamond indenter at a certain applied load. The average diagonal of the indentation is measured using optical microscopy or manually and can be co-related to a hardness value as shown in equation 5.2.

$$HV = \frac{1854.4 * F}{d^2} \quad [5.2]$$

In equation 5.2, F is the applied load (in gf), and d is the length of the diagonal (in µm). The measure is the Vickers hardness value in HV units. In this thesis, Vickers micro-hardness measurements were conducted at 300g applied load for 10s dwell time using a DuraScan system. The testing was conducted as per ASTM E92, and E384 standards [140]. Hardness testing was employed for most of the papers in this thesis as a method to assess tentative mechanical properties as a function of hardness values.

5.7.6. Uniaxial tensile testing

Uniaxial tensile testing was conducted in *Papers III and X*. All the samples were tested following ASTM E8 or similar ISO standards [141]. The samples were printed as cylinders with a length of 100 mm and diameter of 14 mm, and then post-processed depending on heat treatments needed to reach desired properties followed by machining to final specifications. The room temperature tensile samples tested at Höganäs AB, Sweden were run in displacement control at 0.45 mm/min till the yield point, after which they were run at 10 mm/min. The room temperature tensile samples at Chalmers University of Technology were tested on an Instron 8501 servo-hydraulic testing machine at a constant strain rate of 0.01% s^{-1} till failure. High-temperature tensile testing was conducted at Chalmers University of Technology on an Instron 8501 servo-hydraulic testing machine equipped with fast electronic control system and a 1 kHz data logging system. The test was conducted as per ASTM E8 standard with a strain rate of 0.01 % s^{-1}, and the strain was measured with an extensometer during the tests.

5.7.7. Bending fatigue testing

Bending fatigue tests were done at Höganäs AB, Sweden. The tests were conducted on 90 mm x 11 mm x 5 mm samples, which underwent post processing heat treatments followed by machining to achieve final dimensions. The four-point bending test was conducted with a load ratio (R) set to fully reversed bending (R=-1). The testing was conducted using the stair-case method, to begin with average fatigue strength until a run-out limit (set at $2*10^6$ cycles) was reached.

CHAPTER 6:
RESULTS AND DISCUSSION

The results and discussion chapter summarises the work done as presented in the appended papers concerning the research questions defined in section 1.2.

6.1. Al-alloy design tailored for PBF-LB

6.1.1. Supersaturated solid solution

The PBF-LB process is characterised by high cooling rates. Taking advantage of this fact enabled the design of an Al-Mn-Cr-Zr based alloy family with 3-5.5 wt% Mn, 0.1-1.4 wt% Cr, 0.2-2 wt% Zr and 0-2 wt% Mg as summarised in patent application [142]. Several alloy variants were produced to demonstrate the effect of each alloying element and the solubility limits that may be achieved. Three methods were employed to measure the solid solution effect namely X-ray diffraction (XRD), electron microscopy and hardness testing. The electron microscopy part is shown in a later section 6.2.1. X-ray diffraction of as-received powder and as-printed samples were conducted to illustrate the supersaturation achieved post-manufacturing [48]. A summary of XRD plots for all six variants is shown in Figure 35a) wherein it can be seen that there exists a shift in the aluminium diffraction angle peak towards the right (to a higher angle), suggesting that solutes are dissolved in the matrix. These results are presented in *Paper I and Paper II*. The amounts of solutes were estimated using a method from [67] in *Paper I* wherein a simple rule of mixture approach was considered. This rule suggested the resulting lattice parameter of Al-alloy with increasing solubility of Mn, Cr and Zr, see Figure 35b).

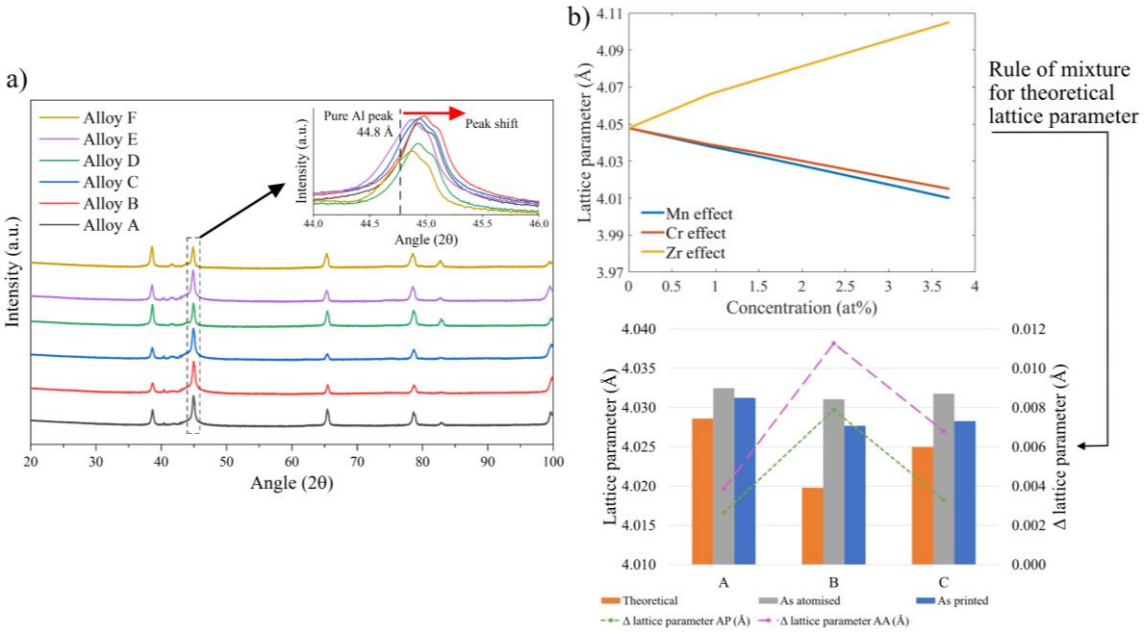

Figure 35 a) Summary of XRD plots for all six alloys in as-printed condition with inset showing peak shift for these alloys as compared to pure-Al b) Rule of mixture approach based on [67] to calculate lattice parameters for these alloys, three alloys namely A-C presented as examples. Data taken from *Paper I* [48] and *Paper II* [123]

Vickers hardness testing was conducted for samples of all six alloy variants produced in both machines. This was conducted as a part of *Paper I* and *Paper II*. Figure 36 shows for all the cases that the hardness values in the alloys were significantly higher than that of pure Al (~15-

20 HV). The hardness also increased with an increasing amount of alloying elements such as Mn, Cr and Mg. There were some additional increases in hardness from potential grain refinement and primary precipitation from the most alloyed grade (alloy F), although it is expected that most of the hardness in the as-printed condition comes from the solid solution strengthening.

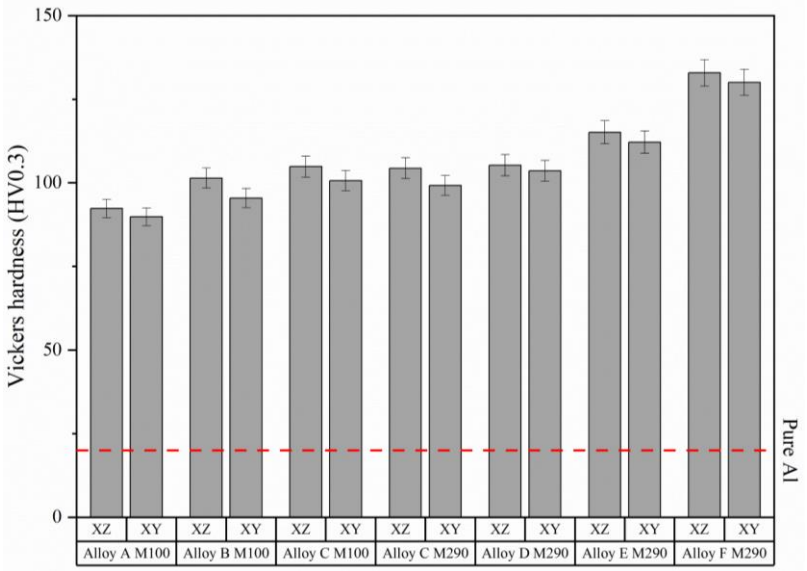

Figure 36 Summary of Vickers hardness (HV0.3) for all the Al-Mn-Cr-Zr alloys manufactured on EOS M100 and EOS M290 machines as compared to pure Al. Error bars represent one standard deviation. Data taken from *Paper I* [48] and *Paper II* [123]

The analysis provided sufficient evidence for a significant solid solution effect in as-printed conditions. Since these exact alloys utilizing PBF-LB do not exist before, similar alloys such as Al-Mn-Cr [116] produced from rapidly solidified powder employing hot extrusion or Al-Mn-Zr [143] developed for splat quenching were considered as closest comparisons. Similar lattice parameters and hardness for similar amounts of elements in solid solution confirmed that most of the alloying elements are indeed in solid solution. As observed by BSE imaging in electron micrographs (see Figure 40 and Figure 42), some unavoidable primary nanoprecipitation occurs during printing. This is mostly triggered for alloy F, for which about 8 area% of precipitates were shown in the as-printed state. This value is however much less as compared to the theoretical amount of precipitates (about 25 vol% at 648 K). It is expected that primary precipitation in alloys D and F would affect the precipitation kinetics during direct ageing heat treatments, which are discussed in later sections. Moreover, Mg added in some of the alloys, namely 1 wt% in alloy E and 1.2 wt% in alloy F underwent 0.2 wt% and 0.1 wt% evaporation respectively during printing, similar to reports in the literature [54], [144].

6.1.2. Defect-tolerant alloy design

As mentioned in previous sections, solidification cracking is the major obstacle to the development of high-strength Al-alloys for the PBF-LB process. The strategy based on Kou's work [40], [53] to reduce the solidification range towards the end of solidification was hence employed as a guide to producing crack-resistant alloys. Figure 37a)-b) compares the Scheil solidification curves and electron micrographs for three alloys having different crack susceptibility. A high amount of solidification cracking is observed in alloy E, mainly due to Mg and a small part possibly due to Fe, and Si segregation, while alloys C, F and Al-7017 are

resistant to solidification cracking. Two solutions are hence depicted and addressed in more detail in *Paper I*, *Paper II* and *Paper III*. The first solution is to avoid alloying with elements such as Mg which increase crack susceptibility while keeping the amount of Fe+Si low. Scheil curves can be used as a measure of the reduction of solidification range and reduction of $\left|\frac{dT}{d(f_s^{\frac{1}{2}})}\right|$ slope close to end of solidification (when $f_s^{\frac{1}{2}}$ ~1, with f_s being mass fraction of solid). The second solution, which is proposed by others [12], [38], [54], [145], [146] involves increasing the amount of primary precipitates which can instigate heterogeneous nucleation of the primary Al (fcc) with resulting grain refinement, thus creating a crack tolerant alloy. In this thesis study, two different ways of Zr increase were looked at, the first (see Figure 37d)) is Zr addition during atomisation itself to reach levels high enough to cause primary Al_3Zr precipitation. A level of 1-1.1 wt% Zr was considered sufficient to trigger enough grain refinement. The other method (see Figure 37e)) was by mixing 7017 Al alloy powder with pure Zr powder (3 wt%) to create a crack-tolerant alloy during printing. The limitation of this second method was the potential creation of micro-cracks at the interface between Zr particles and Al-matrix after manufacturing, which is discussed in *Paper III* [121].

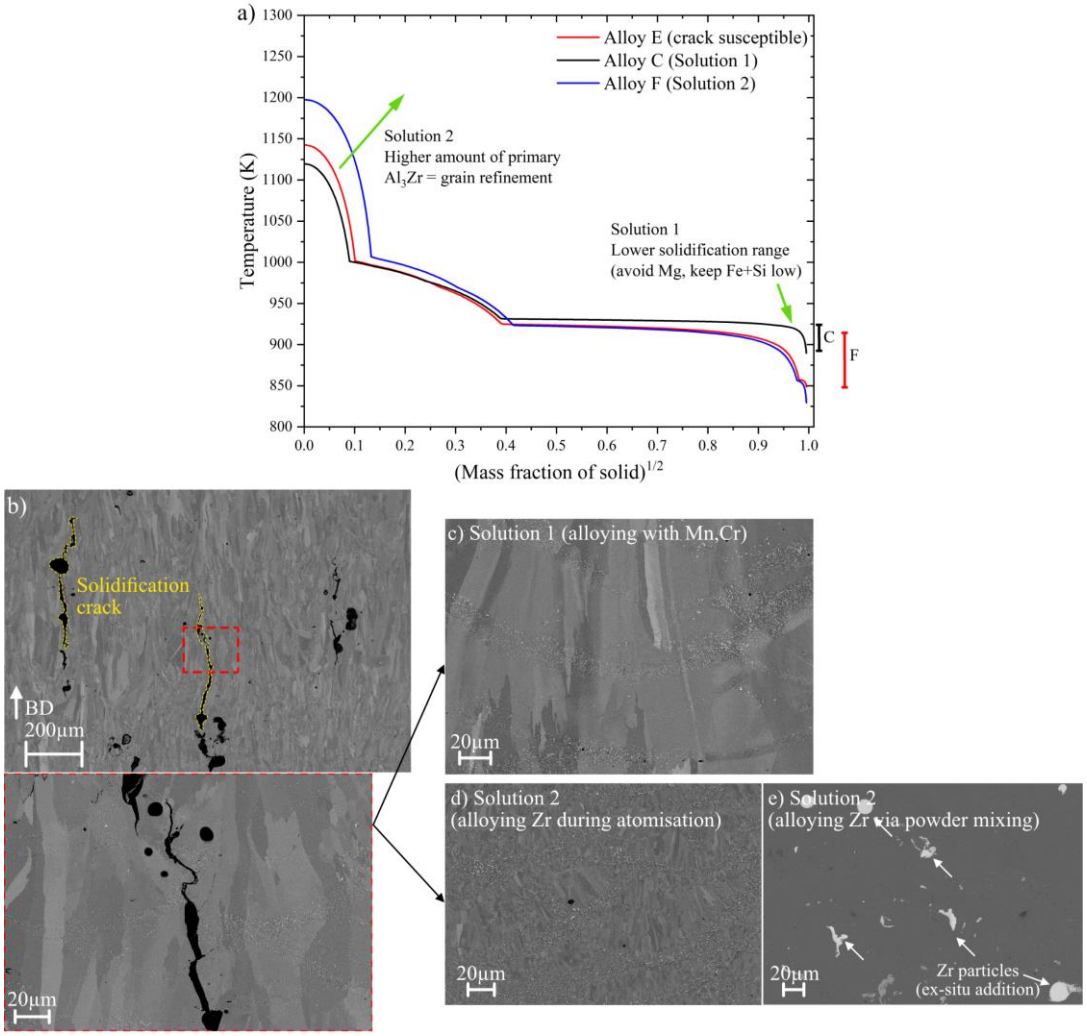

Figure 37 a) Classic Scheil solidification curve for alloys C, E and F with alloy E being crack susceptible and alloy C and F presenting two solutions. Curves drawn using Thermo-Calc 2022a with TCAL8 and MOBAL6 databases b) Electron micrograph showing solidification cracking in alloy E c)-e) Electron micrograph for crack-

free alloys namely alloy C (Al-Mn-Cr-Zr), alloy F (Al-Mn-Cr-Zr) and Al7017 + Zr alloy respectively. Some images were redrawn from *Paper III* [121]

Defect control during PBF-LB manufacturing was a second parameter to ensure defect-free alloys. In this thesis study, a simple full factorial design of the experiment (DOE) was conducted to identify a processing window with variables being laser power and laser speed. In some cases, hatch distance was used as a third variable. In *Paper I* and *Paper V*, the methodology for achieving fully dense samples is addressed. Figure 38 shows a processing window for alloy C (Al-Mn-Cr-Zr alloy) wherein the region with high density (>99%) is seen in red. The relative density of the samples was measured by cutting the samples along three planes XZ, YZ and XY and taking large, stitched images using an optical microscope at 10X objective. This ensured defect detection limits of ~1µm in areas of 40-60 mm^2 each.

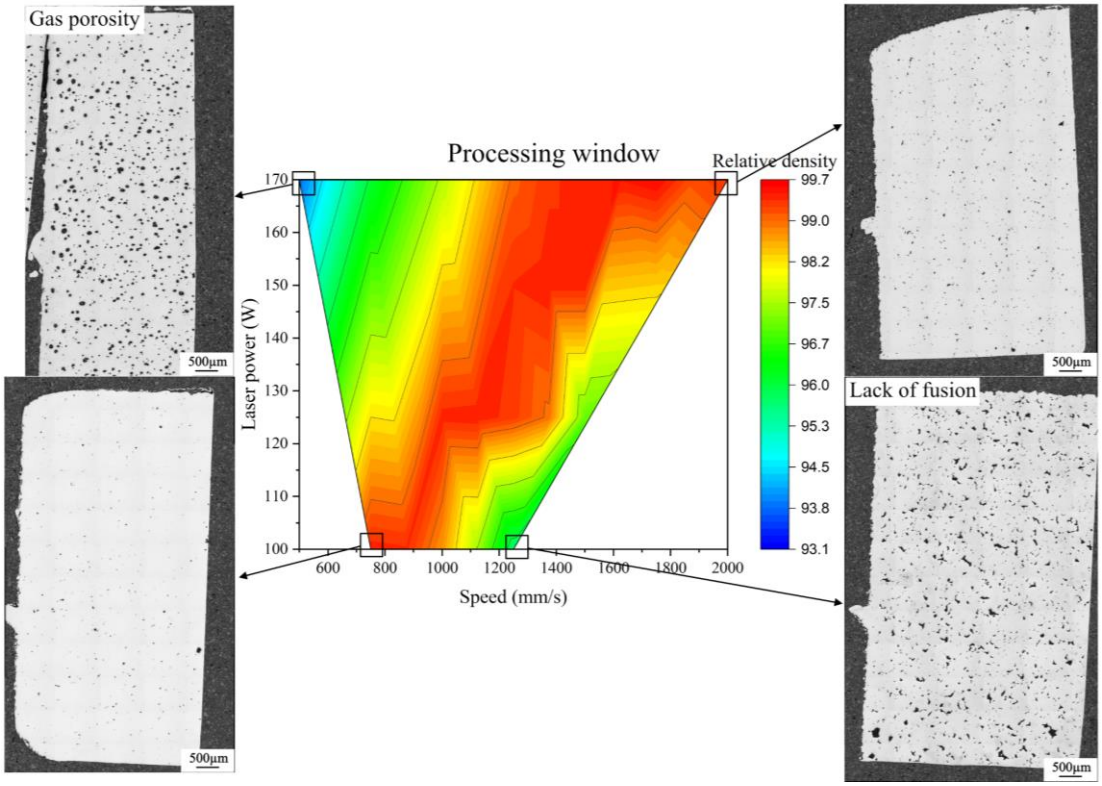

Figure 38 Typical processing window illustrating the relative density in the regions of interest with different laser power (W) and laser speed (mm/s). Processing window taken from Alloy C manufactured using EOS M100 machine. Redrawn from *Paper I* [48]

An additional observation was made when trying to reach optimum processing parameters, see Figure 39. When processing the same material in the EOS M100 machine, there was residual porosity up to 0.4% at optimum parameters, whereas in the EOS M290 machine, the residual porosity <0.2% could be achieved easily. One reason that may be attributed to this could be the laser power in EOS M100 being two-three times more intense per unit area (explained in section 2.2). This may have led to higher susceptibility to evaporation of elements and in general a more complicated melt pool dynamics thus making the processing window narrower thus being susceptible to defect formation. This issue may be resolved by utilising a better set of processing parameters, which could be a part of future studies. However, 99.5-99.6% density in EOS M100 and 99.7-99.8% density in EOS M290 were considered appropriate and nominally fully dense.

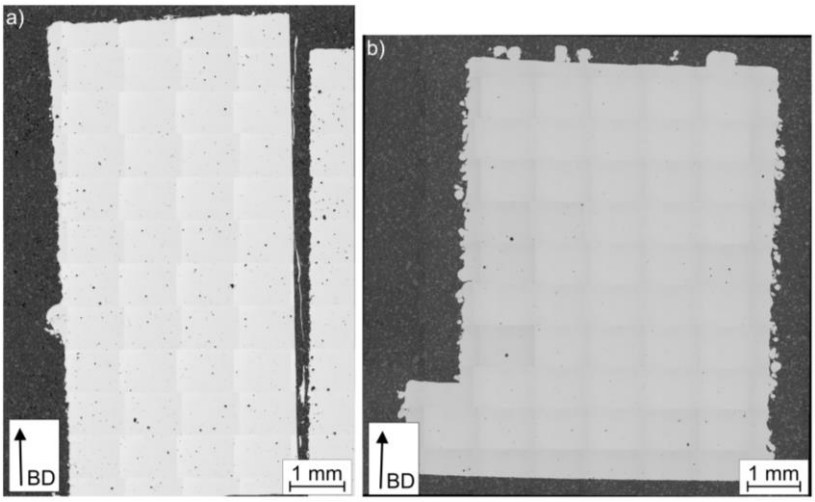

Figure 39 a)-b) As-printed alloy C (Al-Mn-Cr-Zr) processed in EOS M100 and EOS M290 machines respectively.

6.2. Evolution of microstructure during PBF-LB processing and post-processing heat treatments

6.2.1. Microstructure after PBF-LB processing

After printing, samples of all the alloys contained the majority of solutes in Al-matrix. However, the microstructure developed upon PBF-LB processing had some primary precipitation unique to the process. For the Al-Mn-Cr-Zr based alloy variants namely alloys A, B, C and E, the microstructure consisted of long columnar Al-grains along the building direction (see Figure 40 and Figure 41). For alloys D and F, grain refinement of primary Al occurred which created a randomised texture and reduced the grain size by an order of magnitude [123]. In both cases with or without grain refinement, primary precipitates of two categories were observed. The first ones occurred at melt pool boundaries, which were expected to form from remelting layer upon layer thus leading to the formation of these primary precipitates from a supersaturated solid below. The other is solidification boundary precipitates, which were expected to form from during solidification of the material. Even though rapid solidification conditions exist in PBF-LB, these nano-precipitates were formed, nonetheless. As per *Paper I*, it was also observed that relatively larger and spherical precipitates (~200 nm) at melt pool boundaries whereas elongated needle-shaped precipitates (~100 nm length and <50nm width) were observed at solidification boundaries. All the precipitates were enriched in Mn, whereas some were enriched in Cr or tentatively Fe. For the grain refined alloys, primary $L1_2$ type Al_3Zr precipitates were also observed at melt pool boundaries. Their morphology was cubic and sizes of ~200-400 nm. Feature analysis was conducted on the resulting microstructure to verify the amount of supersaturation and study if there is a role of processing parameters in modifying the amount and size of primary precipitates. The results were summarized in *Paper II and Paper IV*. Large area analysis (~0.1 mm^2) for different printing conditions, cross sections and alloy variants were done to show the amount, size and morphology of primary precipitates in as-printed conditions. Feature analysis tool was used at a spatial resolution of 30 nm. Figure 42a)-b), redrawn from *Paper II* shows two different areas scanned for the two variants of Al-Mn-Cr-Zr based alloys denoted alloy C and alloy F. Precipitates at melt pool boundaries and solidification boundaries (such as grain boundaries)

can be seen. The summary of precipitate size distribution is shown in Figure 42c)-d) (from *Paper II* and *Paper IV*). The amount of precipitates and their average size increased when processing the alloys in the M290 machine instead of the M100 machine and when grain refinement occurred in the alloys (alloys D, F). Upon modifying the processing conditions, the amount of precipitation was kept low and a max 0.3 area% of precipitates was observed [147].

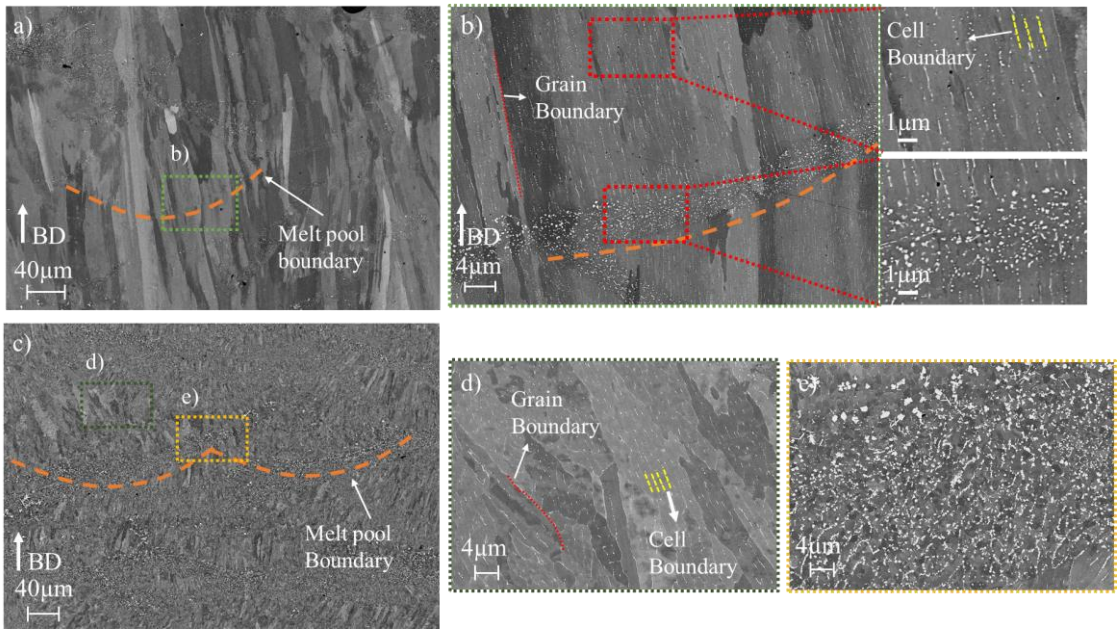

Figure 40 Electron micrograph showing general microstructure for a)-b) Alloy C and c)-e) Alloy F. Two areas which are shown in insets are melt pool boundaries and solidification boundaries (such as cell/grain boundaries). Images adapted from *Paper II* [123]

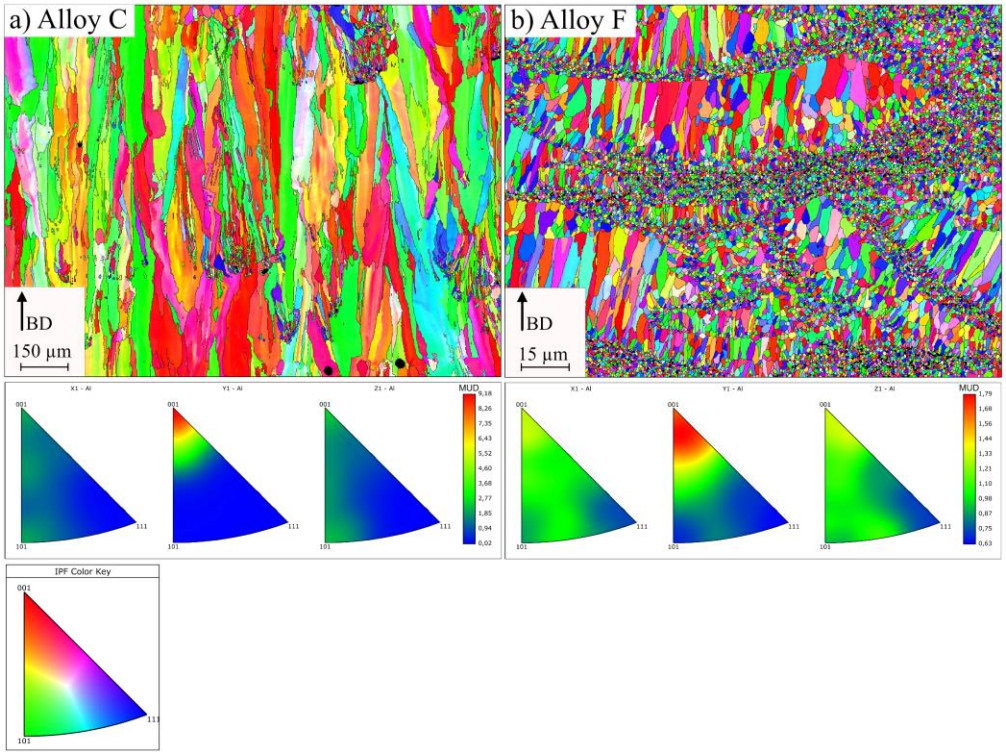

Figure 41 Electron micrograph showing EBSD image of a) Alloy C and b) Alloy F in as-printed condition along building direction (BD). Both images are inverse pole figure X images. Images adapted from *Paper II* [123]

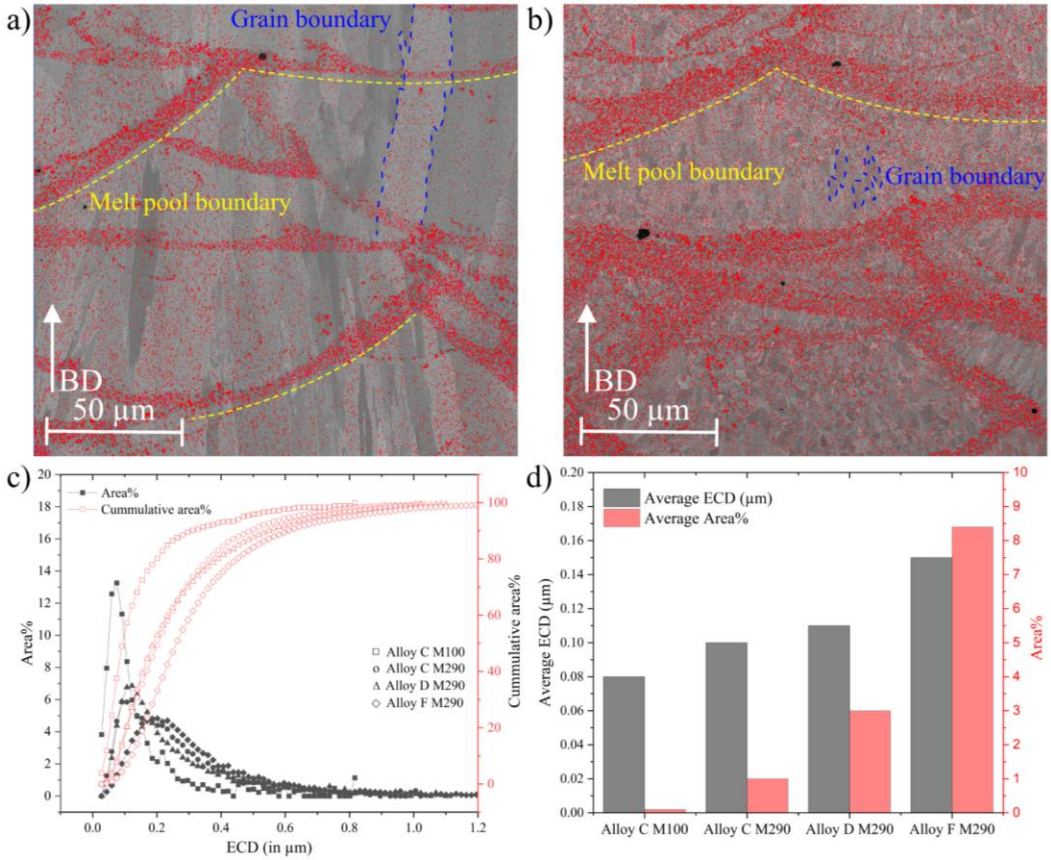

Figure 42 a)-b) Feature analysis summary of alloy C and alloy F along XZ plane (BD) showing precipitates as features (red). The melt pool boundaries and grain boundaries are marked in yellow and blue respectively c) Shows the distribution of precipitates to their equivalent circular diameter (ECD, µm) in four different as-printed conditions and d) Shows the summary of precipitates to average ECD and average area%. Data from *Paper II* [123] and *Paper IV* [147]

6.2.2. Direct ageing heat treatment

To identify the temperature for an optimum hardening response, a range of heat treatments between 523K – 678K were conducted first for alloy C in *Paper I* and *Paper VI*, see Figure 43a). For up to 573 K, negligible or weak hardening response was seen, which picked up significa ntly between 623 K – 648 K. For 623 K 24 h and 648 K 14 h, a peak hardness of 142 HV was observed. Further, a slight increase in temperature (678 K) led to a decrease in peak hardening (128 HV peak) with much faster precipitation kinetics. Thus, 648 K was chosen as an optimum ageing temperature for the highest strength achieved in the shortest time. It was also observed for alloy C that two local peak hardness maxima after around 8 h and 14 h were obtained. This has been reported previously for Al-Mn-Zr alloys by Ohashi et al. [143]. Figure 43b) showed the response for all the six alloy variants processed using EOS M100 and EOS M290 machines at 648 K (summary of results from *Paper I*, *Paper II* and *Paper VI*). When comparing alloys A-C, the clear benefit of Cr (alloy C) is observed. The Cr addition not only seems to increase the peak hardening capability, but it seems that it slows down the kinetics as the peak hardness is achieved after longer ageing times (12-14 h) for alloy C. Additionally, comparing alloy C to Mg-containing alloys (alloy E and F), a clear benefit of Mg is seen which is retained during the heat treatment time. The increase in Zr content in alloy D and alloy F (as compared to alloy C) is also found to impact precipitation kinetics leading to peak hardness quicker. It is postulated that this occurs due to finer grain size, which increase the amount of

grain boundaries available to coarsen precipitates quicker thus causing a shift to the left in peak hardening time. Additionally, alloys D, E and F had higher primary precipitates in as-printed conditions than alloy C, which could affect precipitation kinetics. However, the amount of peak hardenability of alloy E and alloy F (+40 HV) was the same while lowered in alloy D (+30 HV) as compared to alloy C (+40 HV). This indicates similar levels of precipitation hardening for most alloyed version (alloy F).

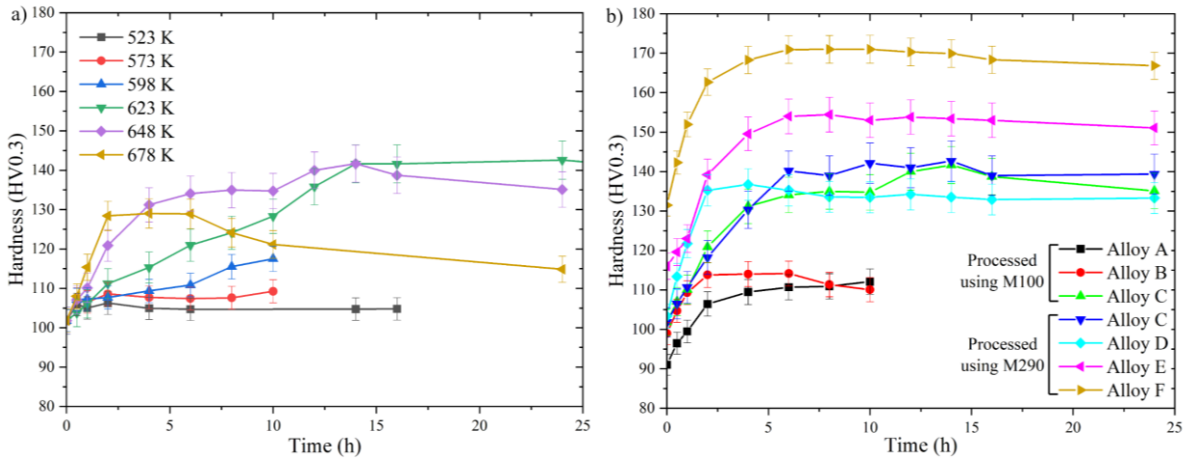

Figure 43 a) Vickers hardness plots for Alloy C heat treated at temperatures between 523 K – 678 K b) Vickers hardness plots for all Al-Mn-Cr-Zr variants heat treated at 648 K. Error bars denote one standard deviation for each condition. Data were taken from *Paper I* [48], *Paper II* [123] and *Paper VI* [126]

6.2.3. Precipitation mechanism

To understand the precipitation mechanisms with two plateaus of peak hardening, alloy C was studied in detail with the help of characterisation tools in *Paper VI*. Feature analysis was conducted for samples aged at 648 K for 0, 8, 14 and 24 h respectively. It was observed that during heat treatment, Mn-rich precipitates grow selectively at grain boundaries, followed by the bulk. The Mn-rich precipitates appear to adopt higher Mn content (Al_6Mn stoichiometry) over time from $Al_{12}Mn$ stoichiometry. The investigation also revealed that Zr-rich precipitates decorate the Mn-rich precipitates. The Zr-rich precipitates were confirmed using EDS analysis in TEM [126]. It is postulated that Cr enrichment in some of the Mn-rich precipitates (tentatively $Al_{12}Mn$ stoichiometry) is responsible for slower precipitation kinetics combined with a better hardening response as $Al_{12}Mn$ precipitates are expected to be semi-coherent with the matrix and the Cr solution into the precipitates would mean slower growth rate thus resulting in more controlled hardening response for alloy C.

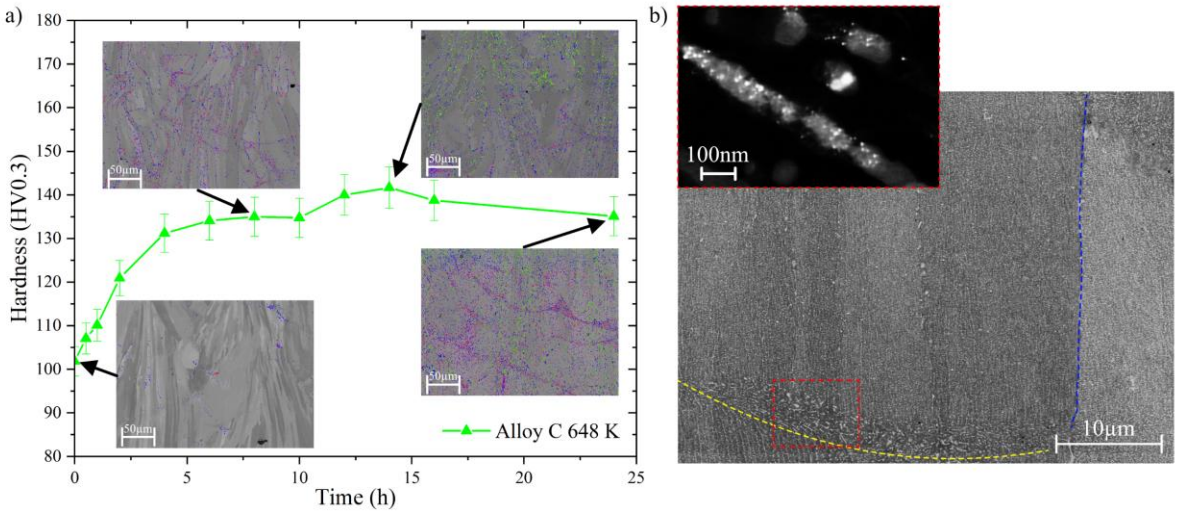

Figure 44 a) Precipitation kinetics for alloy C during heat treatment at 648 K combined with feature analysis shown via electron microscope images. Pink, blue and green features represent matrix precipitates (<5 wt% Mn), $Al_{12}Mn$ (5-20 wt% Mn) and Al_6Mn (>20 wt% Mn) respectively b) Electron microscopy image of alloy C heat treated 648 K 8 h showing melt pool boundaries (yellow) and grain boundaries (blue). The inset image (red) shows the co-precipitation of small Zr-rich precipitates on larger Mn-rich precipitates. Data is redrawn from *Paper VI* [126]

To further understand the effect of Cr on Mn-rich precipitates, in-situ measurements combined with thermodynamic database development work were conducted in *Paper VII* and *Paper VIII* respectively. In *Paper VII*, thin lamellas (1 µm) of alloy C were placed on a MEMS chip and heat treated through the heat treatment cycle at 648 K till 24 h, similar to what was done previously for the hardness study in *Paper VI*. The XRF measurements were conducted with different resolutions during the heat treatment to study the transport of elements across the lamella for different regions of interest. The heat treatment was stopped at 0, 4, 8, 14, 16 and 24 h to take high-resolution scans and get a snapshot of the precipitation phenomenon. The Kα peaks studied were limited to Mn, Cr and Fe as a 9 kV beam was used at the DESY P06 beamline. Two major observations were made from these experiments. The precipitates at melt pool boundaries were distinctly rich in both Mn and Cr and they stayed stable during the whole heat treatment. The precipitates growing at grain boundaries were initially rich in Mn, followed by the decoration of Cr-rich precipitates at the interface of Mn-rich precipitates. However, no depletion of Mn was observed in Cr-rich precipitates or vice versa. Finer precipitates inside the grains could not be studied due to loss of spatial resolution due to a thicker sample (~1 µm) combined with small size (~100 nm) of such precipitates. The second study related to thermodynamic database development (*Paper VIII*) is aimed at depicting the long-term effects of Cr entering into Mn-rich precipitates. Thus, a quinary Al-Mn-Cr-Zr-Fe database based on the TCAL database was provided by Thermo-Calc AB. Experimental samples of alloy C heat treated at 623 K for >1000 h (samples also studied in *Paper IX*) were considered to be representative of a steady-state condition. The comparison of Cr solubility in two different Mn-rich precipitates (namely Al_6Mn and $Al_{12}Mn$) was conducted. Thermodynamic parameters were defined based on theoretical work on Al-Mn-Cr ternary systems [148], [149]. Then, by combining these theoretical calculations with the experimental data, updated thermodynamic parameters were added to the quinary system. When precipitation calculations were conducted using PRISMA toolbox with the new thermodynamic parameters, it was indeed observed that

Cr solubility slows down the kinetics and stabilises the $Al_{12}Mn$ precipitate as compared to a system where no Cr solubility exists. The results agree well with the experimental observations that Cr slows down the precipitation as shown in *Paper VI*. However, the interpretation of the role of Cr is not fully clear as *Paper VII* showed the formation of Cr-rich precipitates on Mn-rich precipitate interfaces which is not the same as Cr being dissolved in the Mn-rich precipitates. More future studies are being conducted to understand this, which are not appended in this thesis study.

6.3. Mechanical properties of alloys

This chapter presents the results of the mechanical testing of the alloys studied. The two main objectives for the development of the Al-Mn-Cr-Zr based alloys were high strength (>450 MPa) at room temperature (RT) combined with high-temperature resistance (up to 573 K). Long-term thermal stability was tested by peak hardening first and then pursuing isothermal holds at 523 K for 2544 h and 623 K for 1054 h. The alloys were also benchmarked against other Al-alloys such as AlSi10Mg and Al-Mg-Sc-Zr (Scalmalloy®), both of which were also PBF-LB processed at Chalmers University of Technology.

6.3.1. Uniaxial tensile properties at room temperature

Among the variants produced in Al-Mn-Cr-Zr based alloys, alloy C, alloy D and alloy F were produced for uniaxial tensile testing, as presented in *Paper X*. Seven samples along XZ and XY directions were tested in both as-printed and heat-treated conditions. The results are summarised in Table 8 and compared against the performance of AlSi10Mg, Al-Mg-Sc-Zr (Scalmalloy®) and Al7017 + Zr + TiC alloys (*Paper III*). About 10 samples for each building direction were printed for AlSi10Mg, 3 samples along XY direction for Al-Mg-Sc-Zr and up to 2 samples (as-printed + heat-treated condition) for Al7017 + Zr + TiC. Hence the uniaxial tensile results from Al-Mg-Sc-Zr and Al7017 + Zr + TiC are not having the same statistical relevance. Overall, the Al-Mn-Cr-Zr alloys in peak hardened condition exceed the objective of >450 MPa strength, with the best alloys (alloy F) reaching ~550 MPa UTS. These alloys are also versatile with a wide range of mechanical properties tuneable by alloy composition and application of direct ageing. Alloy C and alloy D show high ductility in as-printed conditions and alloy F show high strength in peak hardened condition.

Table 8 Summary of uniaxial tensile properties of all the alloys produced as part of this thesis work. The properties for all the alloys are averaged along both XZ and XY directions of printing, except Al-Mg-Sc-Zr which was only printed along XY direction. Values are rounded off to the next tenths digit for simplicity

Alloy	Heat treatment	Yield strength (R_p0.2%, MPa)	Tensile strength (R_m, MPa)	Elongation to failure (%)	Reference
Alloy C (Al-Mn-Cr-Zr)	As-printed	250	310	25	*Paper X*
	648 K 24 h (*Paper VI*)	350	440	8	*Paper X*
Alloy D (Al-Mn-Cr-Zr)	As-printed	300	330	25	*Paper X*
	648 K 4 h (*Paper II*)	360	430	3	*Paper X*
Alloy F (Al-Mn-Cr-Zr)	As-printed	390	450	17	*Paper X*
	648 K 8 h (*Paper II*)	500	560	5	*Paper X*
AlSi10Mg	As-printed	240	460	13	[150]

	Peak aged (EOS T6 data)	260	320	11	[27]
Al-Mg-Sc-Zr (Scalmalloy®)	As-printed	290	360	19	Internal work
	598 K 4 h (*Paper V*)	470	520	8	Internal work
Al7017 + Zr + TiC	As-printed	250	310	20	*Paper III*
	Peak aged	440	460	9	*Paper III*

6.3.2. Long-term thermal stability

The Al-Mn-Cr-Zr based alloys were assessed considering their long-term thermal stability in *Paper IX*. All the samples went through direct ageing heat treatment post-PBF-LB processing at 623 K for 24 h to reach peak hardness. After achieving peak hardness, a few samples were tested at a lower temperature (523 K) for another 2544 h (106 days) to study the decrease in hardness over time. Another set of peak hardened samples was heat treated at the same temperature (623 K) for another 1054 h (~44 days) to notice the decrease in hardness. Few samples were taken out at different times, as is visible from the data points. Figure 45 shows the hardness values for alloy C as a function of isothermal holding time at 523 K and 623 K. Alloy C showed no decrease in hardness at 523 K for 2544 h (106 days). The samples at 623 K showed a decrease of 17 HV (~12%) decrease from peak hardness, thus suggesting attractive thermal stability as high as 623 K. The two families of precipitates, namely Mn-rich and Zr-rich are hence considered to be resistant to coarsening over long times. This is confirmed by employing the microstructural characterisation in *paper IX*.

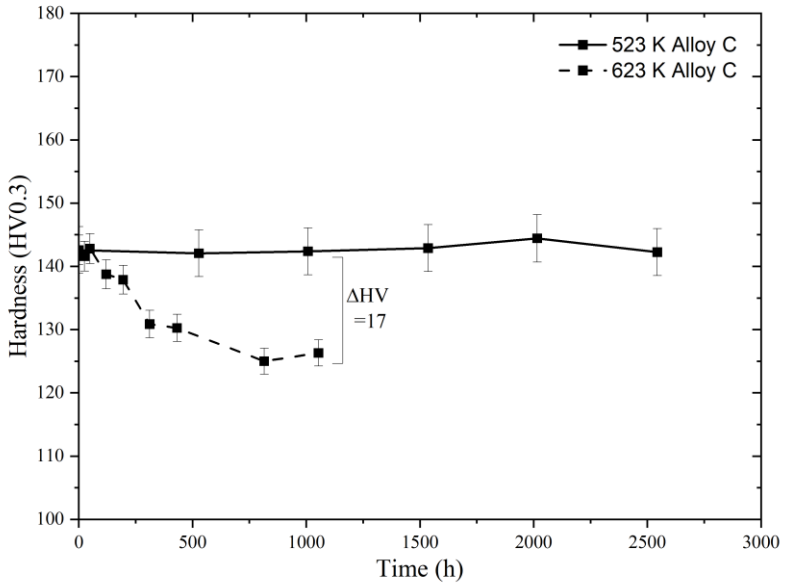

Figure 45 Long-term thermal stability of alloy C after peak ageing heat treatment at 623 K. Long-term testing at 523 K 2544 h and 623 K 1054 h after peak ageing. Data taken from *Paper IX* [151]

6.3.3. Uniaxial tensile properties at elevated temperature

The second part of the equation to illustrate the high-temperature stability of these alloys is uniaxial tensile testing at elevated temperatures. *Paper X* reports these results wherein heat-treated samples of alloy C and alloy F from the Al-Mn-Cr-Zr based family of alloys were tested

from room temperature up to 573 K. The results suggest that while alloy F maintains a high YS of 490 MPa at room temperature, its YS reduces to ~100 MPa at 573 K. Alloy C, however, shows lower YS of 340 MPa at room temperature, but has >150 MPa YS at 573 K. Nevertheless, the possibility to have >100 MPa YS at high temperatures describe a strong alloy system as compared to most conventional Al-alloys [13].

6.3.4. Bending fatigue

Four point bending tests were conducted on alloy C, alloy D and alloy F in heat-treated conditions, as reported in *Paper X*. These tests were conducted to assess the fatigue performance of these alloys. The load ratio was set to fully reversed bending (R = -1). The test sequence was using the staircase method. The runout limit of 2 million cycles was set and about 30 samples of each alloy were tested to identify the low-cycle and high-cycle region of fatigue. Fatigue strength in peak aged conditions (with 50% probability) was observed to be between 140-200 MPa depending on the alloy tested (alloys C, D and F were tested). The fatigue strength of these alloys describe an Al-alloy with high fatigue limit as compared to most conventional Al-alloys [27], [60], [152], [153].

CONCLUSIONS

RQ1: How to design Al-alloys tailored for the PBF-LB process?

Supersaturated solid solution

- Rapid solidification conditions during PBF-LB processes increase the solubility of Mn, Zr by about three times the equilibrium limit. Solutes like Cr and Mg (up to solubility limit) improve the solid solution effect and help reach the objective of high-temperature strength
- Low amount of precipitates are formed upon printing. Introducing Zr beyond the solubility limit or adding Mg increases the amount of primary precipitates. The Zr increase beyond solubility causes grain refinement of primary-Al thus increasing primary precipitation. Adding Mg stabilises liquid-Al by reducing melting temperature and causes chemical segregation during solidification thus increasing primary precipitation

Defect-tolerant alloy design

- Solidification cracking occurs with Mg addition (alloy E). This is shown to be resolved by either avoiding Mg altogether (alloy C) or increasing Zr content beyond solubility to cause heterogeneous nucleation of primary-Al (alloy D, alloy F, Al 7017) thus creating crack tolerant alloys. The Zr addition is shown to work both via in-situ alloying or ex-situ mixing
- Porosity and lack of fusion that are formed during PBF-LB processing were avoided using simple full factorial DOE. For the EOS M100 machine, three variables namely laser power, laser speed and hatch distance were varied. For the EOS M290 machine, two variables namely laser power and laser speed were varied to achieve processing windows. In both cases, high relative density (>99.5%) was achieved

RQ2: How does the microstructure develop during the PBF-LB process and post-processing heat treatments?

Microstructure developed during PBF-LB processing

- During PBF-LB processing, primary precipitation at melt pool boundaries and solidification boundaries occurs, as is observed from studying as-printed samples. Alloys variants with low Zr (alloy A, B, C, E) have columnar Al-grain growth along building direction, whereas those containing high Zr (alloy D, F) contain grain refinement
- Most of the precipitates formed in as-printed conditions were observed to be rich in Mn. Some of them were also seen to be rich in Cr, and possibly Fe. For grain-refined alloys, primary $L1_2$ type Al_3Zr precipitates were observed at melt pool boundaries. Overall, primary precipitation between 0.2-1% for alloy C and up to 8% for alloy F was observed, which is low than maximum precipitation possible (~25%)

Direct ageing heat treatments

- Direct ageing heat treatments were conducted on one of the alloys (alloy C) between 523 K – 678 K to identify optimum temperature–time response. The temperature of 623 K and 648 K were chosen to produce the highest increase in hardness (~40 HV) in optimum time
- When the hardening response was compared between all the six alloy variants at 648 K, the benefit of each alloying element to strength became clear due to the creation of six variants. The Mn and Cr addition provided solid solution strength, which became precipitation strength upon heat treatment. The Cr addition slowed down the possible precipitation kinetics in the alloys. The Mg addition seemed to have the opposite effect but

provided solid solution strength in both as-printed and heat-treated conditions. The Zr addition provided strength upon heat treatments. Adding Zr beyond the solubility limit caused primary Al-grain refinement which also increase the strength

Precipitation mechanisms

- Alloy C showed double hardening peaks during direct ageing at 648 K, at 8 h and 14 h respectively. Post-mortem microstructural characterisation showed that Mn-rich precipitates grew preferentially at grain boundaries followed by formation in the bulk of the sample
- Primary strengthening of the alloys comes from finely dispersed Al_3Zr nanoprecipitates combined with needle/plate-shaped Mn-rich precipitates in the matrix. Some Zr-rich precipitates were characterised as co-precipitating with Mn-rich precipitates, which could directly impact their kinetics
- In-situ XRF analysis at synchrotron sources shed more light on precipitation reactions. At the melt pool boundary, precipitates are rich in both Mn and Cr and these precipitates are stable during heat treatments. At grain boundaries, precipitates grow as Mn-rich precipitates and during heat treatment, Cr-rich precipitates form at the interfaces of the Mn-rich precipitates and matrix. This showed an active role of Cr in precipitation kinetics
- Thermodynamic database development was conducted to understand the Al-Mn-Cr system. A first attempt done by modifying the parameters of Mn-rich precipitates to account for Cr solubility in them. Results showed slowing of precipitation kinetics and stabilisation of the $Al_{12}Mn$ phase, which is confirmed previously from the characterisation experiments and seen from hardness curves

RQ3: To what extent could such Al-alloys meet the set performance goals?

The Al-Mn-Cr-Zr based alloy system was designed to provide high strength at room temperature (>450 MPa strength) combined with high-temperature stability (up to 573 K)

Uniaxial tensile properties at room temperature

Three of the alloys (alloys C, D and F) were chosen for uniaxial tensile tests at room temperature. Their properties showed high versatility with yield strengths of 250-500 MPa, ultimate tensile strengths of 300-550 MPa and elongation to failure of 3-25%. The room temperature properties show high strength, do not use any rare earth elements and require simple direct ageing heat treatments to achieve peak strength

Long-term thermal stability

Long-term thermal stability tests on one of the alloys (alloy C) in peak hardened condition at 523 K for 2544 h and 623 K for 1054 h were conducted. At 523 K, there was no change in hardness. At 623 K, only 17 HV loss (12%) in hardness suggesting potential thermally stable alloys at high temperatures (up to 573 K)

Uniaxial tensile properties at elevated temperatures

Uniaxial tensile testing for alloys C and F was conducted at elevated temperatures (up to 573 K). Both the alloys were peak hardened before testing. Alloy F showed a yield strength of 490 MPa at room temperature and >100 MPa yield strength at 573 K. Alloy C showed a yield strength of 340 MPa at room temperature and >150 MPa yield strength at 573 K

Other properties such as bending fatigue of 140-200 MPa at fully reversed bending (R=-1) were observed.

FUTURE WORK

Alloy design

- The alloy variants elucidate the Zr effect clearly (*Paper I, II, III*). However, the role of Mg could be understood better by modifying compositions to study the onset of cracking and conducting in-operando studies to elucidate the effect of Mg
- Alloy F (*Paper II, VI, VII*) showed higher Mn-rich precipitation combined with faster kinetics upon heat treatment. More variants containing less Mn could be designed to keep full supersaturation after printing. One alloy variant (alloy G) was produced (not mentioned in the thesis) with 4wt% Mn, which could be studied further

Process development

- Processing parameters such as pre-heating, scan strategy etc. were not experimented with as part of this thesis work. These could be explored to see if any performance gains could be achieved such as retaining full supersaturation in alloy F (Paper *I, II*)
- The PBF-LB process can be developed for higher layer thickness (60,90 µm) which is possible for other Al-alloys that would improve productivity. With increased layer thickness, the remelted zones will reduce which might improve the properties (*Paper X*)
- Additional work on contour parameters is needed for good surface roughness and sub-surface porosity control. Some studies have suggested optimising processing parameters to improve the fatigue life of alloys at the cost of a slight reduction in tensile properties, which could be worth investigating

Structure-property characterisation

- The precipitation reactions are not understood in full detail (*Paper VI, VII*). Furthermore, advanced characterisation including TEM, APT, and in-situ methods is needed to elucidate the precipitation reactions. This could be coupled with further CALPHAD studies (*Paper VIII*) to include cross solubility of solutes which directly impacts precipitation reactions. Some experiments are ongoing with analysis of synchrotron work conducted at ESRF, France and TEM work ongoing at Grenoble, France
- Heat treatments could be further optimised between 623 K – 673 K by making a test matrix of 5 K instead of 25 K steps. This could be beneficial to optimise heat treatment time
- Mechanical testing such as uniaxial tensile and bending fatigue showed promising results (*Paper X*). More fatigue tests could be conducted to understand fatigue behaviour. More thermal stability tests may be conducted at temperatures between 523 – 623 K to understand at which temperature the alloy stays completely stable (*Paper IX*). Since these alloys are designed for up to 573 K, that could be a temperature of interest. Some experiments are already ongoing at Höganäs
- High-temperature tensile testing showed promising results (*Paper X*). Similar tests could be conducted at as-printed conditions and different strain rates to understand their role in mechanical properties. Moreover, since alloy C showed reduced ductility with increasing temperature of testing, this needs to be investigated.
- The corrosion properties of these alloys and the benchmarking against commercially available Al-alloys would be of interest since it was part of the alloy design

ACKNOWLEDGEMENTS

I would like to thank my supervisors Professor Lars Nyborg and Docent Karin Frisk for their unwavering support over the years. I would also like to thank my co-supervisor Professor Eduard Hryha and industrial supervisor Adjunct Professor Sven Bengtsson (Höganäs AB) for everything. I am extremely thankful for this opportunity to create something over the past few years.

I acknowledge the support from the funding I have received for doing this work. Centre for Additive Manufacturing – Metal (CAM^2), supported by VINNOVA, ALL-Light project, supported by VINNOVA, European Union's Horizon 2020 MANUELA project (grant agreement nr. 820774) and Vetenskapsrådet.

A big thanks to all my collaborators who taught me new perspectives and brought great experiences and long discussions to the table. That helped bring a lot of this research work to completion. Special thanks to the colleagues at Höganäs AB [Sven, Sigurd, André, Björn, Dmitri and Denis] who have been more than keen on helping with different experiments over the years, however extreme my demands may have been. forAM® Al-HS1 is a result of all that work together that I would cherish.

Thanks go to colleagues at RISE, Mölndal who have been very helpful, and it has been fun to work with all of you. Thanks to Eero, Marie and Jesper who have been teaching me about Al-alloys and AM since even before I started my PhD. I would like to thank my only MSc thesis student Arvid who did an excellent job. At Chalmers, I would like to acknowledge the research support from Roger, Yiming, Eric, Johnny and Håkan over the years. Also, Jessica, Lilvor and Maria for help with administrative support. I would like to thank all my colleagues in the department, especially from our AM group. Our group is special with people from all over the world keeping our work (or other) discussions fun. All my numerous officemates, especially Elangho, thanks for bearing with me. My badminton and tennis mates for all the good times.

Since this thesis has not been possible just by working within the confines of the department, immense support from my friends and family has been helping me over the years to push me in the right direction. All those friends in India, Sweden and around the world I would like to thank you for not losing hope and bearing with me all these years, especially and not limited to Fredrik, Richard, Erika, Mohit, Jalaj, Lakshit, Rasmus, Bala, Ismail and the list goes on.. Thanks goes to my loving family who has been on the opposite side of the earth but have made sure I feel their love and support all the time.

Finally, to the special person in my life, Jyo, thank you for about a decade of togetherness. Your support has been key to making all this happen and I am looking forward to more adventures together.

REFERENCES

[1] "Additive manufacturing – General principles – Fundamentals and vocabulary (ISO/ASTM 52900:2021)," 2021, [Online]. Available: www.sis.se

[2] C. Emmelmann, P. Sander, J. Kranz, and E. Wycisk, "Laser additive manufacturing and bionics: Redefining lightweight design," in *Physics Procedia*, Elsevier B.V., 2011, pp. 364–368. doi: 10.1016/j.phpro.2011.03.046.

[3] C. Yan, L. Hao, A. Hussein, S. L. Bubb, P. Young, and D. Raymont, "Evaluation of light-weight AlSi10Mg periodic cellular lattice structures fabricated via direct metal laser sintering," *J Mater Process Technol*, vol. 214, no. 4, pp. 856–864, 2014, doi: 10.1016/j.jmatprotec.2013.12.004.

[4] B. Blakey-Milner *et al.*, "Metal additive manufacturing in aerospace: A review," *Mater Des*, vol. 209, p. 110008, 2021, doi: 10.1016/j.matdes.2021.110008.

[5] D. Gu, X. Shi, R. Poprawe, D. L. Bourell, R. Setchi, and J. Zhu, "Material-structure-performance integrated laser-metal additive manufacturing," *Science (1979)*, vol. 372, no. 6545, 2021, doi: 10.1126/science.abg1487.

[6] Höganäs AB, "forAM(r) Al-HS1 powder." https://www.hoganas.com/en/powder-technologies/products/foram/foram-al-hs1-20-63-ga/

[7] "Wohlers Report 2022," 2022.

[8] C. PAUZON, *Tailored process gases for laser powder bed fusion*. 2021. [Online]. Available: https://research.chalmers.se/en/publication/522522%0Ahttps://research.chalmers.se/publication/522522/file/522522_Fulltext.pdf

[9] W. Krenz, *Manufacturing Industries 2030*. Oliver Wyman, 2020. [Online]. Available: https://www.oliverwyman.com/content/dam/oliver-wyman/v2/publications/2020/November/Oliver_Wyman_Manufacturing_Industries_2030_final.pdf

[10] WorldBank, "Manufacturing, value added." https://data.worldbank.org/indicator/NV.IND.MANF.CD (accessed May 22, 2023).

[11] D. D. Gu, W. Meiners, K. Wissenbach, and R. Poprawe, "Laser additive manufacturing of metallic components: Materials, processes and mechanisms," *International Materials Reviews*, vol. 57, no. 3, pp. 133–164, 2012, doi: 10.1179/1743280411Y.0000000014.

[12] P. A. Rometsch, Y. Zhu, X. Wu, and A. Huang, "Review of high-strength aluminium alloys for additive manufacturing by laser powder bed fusion," *Mater Des*, vol. 219, p. 110779, 2022, doi: 10.1016/j.matdes.2022.110779.

[13] ASM International, "Introduction to Aluminum and Aluminum Alloys," *Metals Handbook Desk Edition*, pp. 417–423, 1998, doi: https://doi.org/10.31399/asm.hb.v02.9781627081627.

[14] J. J. deBarbadillo and J. J. Fischer, "Dispersion-Strengthened Nickel-Base and Iron-Base Alloys," in *Properties and Selection: Nonferrous Alloys and Special-Purpose Materials*, ASM International, 1990, pp. 943–949. doi: 10.31399/asm.hb.v02.a0001103.

[15] P. Samal and J. Newkirk, Eds., *Powder Metallurgy*. ASM International, 2015. doi: 10.31399/asm.hb.v07.9781627081757.

[16] G. Costabile, M. Fera, F. Fruggiero, A. Lambiase, and D. Pham, "Cost models of additive manufacturing: A literature review," *International Journal of Industrial Engineering Computations*, vol. 8, no. 2, pp. 263–282, Apr. 2016, doi: 10.5267/j.ijiec.2016.9.001.

[17] M. Mandolini, M. Sartini, C. Favi, and M. Germani, "Cost Sensitivity Analysis for Laser Powder Bed Fusion," *Proceedings of the Design Society*, vol. 2, pp. 1411–1420, May 2022, doi: 10.1017/pds.2022.143.

[18] R. A. Michi, A. Plotkowski, A. Shyam, R. R. Dehoff, and S. S. Babu, "Towards high-temperature applications of aluminium alloys enabled by additive manufacturing," *International Materials Reviews*, 2021, doi: 10.1080/09506608.2021.1951580.
[19] R. Schreiber, "The Growing Role Aluminum & Titanium Is Playing in the Manufacturing Resurgence." https://www.gray.com/insights/the-growing-role-aluminum-titanium-is-playing-in-the-manufacturing-resurgence/
[20] O. E. Directorate, "OECD Global Forum on Environment Focusing on Sustainble Materials Case Study 2 : Aluminium," *Environment*, no. October, p. 66, 2010.
[21] J. A. Kinnaird and P. A. M. Nex, "Critical raw materials," *Routledge Handbook of the Extractive Industries and Sustainable Development*, pp. 13–33, 2022, doi: 10.4324/9781003001317-3.
[22] N. T. Aboulkhair, M. Simonelli, L. Parry, I. Ashcroft, C. Tuck, and R. Hague, "3D printing of Aluminium alloys: Additive Manufacturing of Aluminium alloys using selective laser melting," *Prog Mater Sci*, vol. 106, no. August 2018, p. 100578, 2019, doi: 10.1016/j.pmatsci.2019.100578.
[23] A. Leicht, *Laser powder bed fusion of 316L stainless steel Microstructure and mechanical properties as a function of process*. 2020.
[24] N. Nadammal *et al.*, "Critical role of scan strategies on the development of microstructure, texture, and residual stresses during laser powder bed fusion additive manufacturing," *Addit Manuf*, vol. 38, no. December 2020, p. 101792, 2021, doi: 10.1016/j.addma.2020.101792.
[25] H. Lee, C. H. J. Lim, M. J. Low, N. Tham, V. M. Murukeshan, and Y. J. Kim, "Lasers in additive manufacturing: A review," *International Journal of Precision Engineering and Manufacturing - Green Technology*, vol. 4, no. 3, pp. 307–322, 2017, doi: 10.1007/s40684-017-0037-7.
[26] A. V. Gusarov *et al.*, "On productivity of laser additive manufacturing," *J Mater Process Technol*, vol. 261, no. March, pp. 213–232, 2018, doi: 10.1016/j.jmatprotec.2018.05.033.
[27] EOS GmbH, "EOS Aluminium AlSi10Mg Material Data Sheet EOS Aluminium AlSi10Mg Good Strength & Dynamic Load Bearing Capacity," 2022.
[28] A. Leicht, M. Fischer, U. Klement, L. Nyborg, and E. Hryha, "Increasing the Productivity of Laser Powder Bed Fusion for Stainless Steel 316L through Increased Layer Thickness," *J Mater Eng Perform*, vol. 30, no. 1, pp. 575–584, 2021, doi: 10.1007/s11665-020-05334-3.
[29] K. Riener, S. Oswald, M. Winkler, and G. J. Leichtfried, "Influence of storage conditions and reconditioning of AlSi10Mg powder on the quality of parts produced by laser powder bed fusion (LPBF)," *Addit Manuf*, vol. 39, no. February, p. 101896, 2021, doi: 10.1016/j.addma.2021.101896.
[30] D. Buchbinder, W. Meiners, N. Pirch, K. Wissenbach, and J. Schrage, "Investigation on reducing distortion by preheating during manufacture of aluminum components using selective laser melting," *J Laser Appl*, vol. 26, no. 1, p. 012004, 2014, doi: 10.2351/1.4828755.
[31] J. P. Oliveira, A. D. LaLonde, and J. Ma, "Processing parameters in laser powder bed fusion metal additive manufacturing," *Mater Des*, vol. 193, pp. 1–12, 2020, doi: 10.1016/j.matdes.2020.108762.
[32] W. Hearn, *Development of Structural Steels for Powder Bed Fusion – Laser Beam*. 2023. [Online]. Available: https://research.chalmers.se/publication/534092%0Ahttps://research.chalmers.se/publication/534092/file/534092_Fulltext.pdf
[33] K. Georgilas, R. H. U. Khan, and M. E. Kartal, "The influence of pulsed laser powder bed fusion process parameters on Inconel 718 material properties," *Materials Science and Engineering A*, vol. 769, no. June 2019, p. 138527, 2020, doi: 10.1016/j.msea.2019.138527.
[34] A. Martucci, E. L. Tam, A. Aversa, M. Lombardi, and L. Nyborg, "The effect of powder reuse on the surface chemical composition of the Scalmalloy powder in Powder Bed Fusion – Laser

Beam process," *Surface and Interface Analysis*, no. May 2022, pp. 388–395, 2022, doi: 10.1002/sia.7176.

[35] B. Brandau, A. Da Silva, C. Wilsnack, F. Brueckner, and A. F. H. Kaplan, "Absorbance study of powder conditions for laser additive manufacturing," *Mater Des*, vol. 216, p. 110591, 2022, doi: 10.1016/j.matdes.2022.110591.

[36] A. Aversa *et al.*, "New aluminum alloys specifically designed for laser powder bed fusion: A review," *Materials*, vol. 12, no. 7, 2019, doi: 10.3390/ma12071007.

[37] S. Kirihara and K. Nakata, *Multi-dimensional Additive Manufacturing*. 2020. doi: 10.1007/978-981-15-7910-3.

[38] R. S. Mishra and S. Thapliyal, "Design approaches for printability-performance synergy in Al alloys for laser-powder bed additive manufacturing," *Mater Des*, vol. 204, p. 109640, 2021, doi: 10.1016/j.matdes.2021.109640.

[39] A. Durga *et al.*, "Grain refinement in additively manufactured ferritic stainless steel by in situ inoculation using pre-alloyed powder," *Scr Mater*, vol. 194, p. 113690, 2021, doi: 10.1016/j.scriptamat.2020.113690.

[40] S. Kou, *Welding Metallurgy*, 2nd ed., no. 2. Hoboken, New Jersey, 2002. [Online]. Available: http://www.i-scholar.in/index.php/IWJ/article/view/150243

[41] S. Ly, A. M. Rubenchik, S. A. Khairallah, G. Guss, and M. J. Matthews, "Metal vapor micro-jet controls material redistribution in laser powder bed fusion additive manufacturing," *Sci Rep*, vol. 7, no. 1, pp. 1–12, 2017, doi: 10.1038/s41598-017-04237-z.

[42] T. DebRoy *et al.*, "Additive manufacturing of metallic components – Process, structure and properties," *Prog Mater Sci*, vol. 92, pp. 112–224, 2018, doi: 10.1016/j.pmatsci.2017.10.001.

[43] A. Raza *et al.*, "Degradation of AlSi10Mg powder during laser based powder bed fusion processing," *Mater Des*, vol. 198, 2021, doi: 10.1016/j.matdes.2020.109358.

[44] C. Schwerz, A. Raza, X. Lei, L. Nyborg, E. Hryha, and H. Wirdelius, "In-situ detection of redeposited spatter and its influence on the formation of internal flaws in laser powder bed fusion," *Addit Manuf*, vol. 47, no. October, p. 102370, 2021, doi: 10.1016/j.addma.2021.102370.

[45] K.E.Easterling and D.A.Porter, *Phase Transformations in Metals and Alloys*, Second. London: Chapman & Hill, 1992.

[46] B. MEHTA, "High Performance Aluminium Alloys for Laser Powder Bed Fusion: Alloy Design and Development," p. 48, 2021, [Online]. Available: https://www.chalmers.se/sv/institutioner/ims/kalendarium/Sidor/High-Performance-Aluminium-Alloys-for-Laser-Powder.aspx%0Ahttps://research.chalmers.se/publication/527075/file/527075_Fulltext.pdf

[47] H. Gong, K. Rafi, H. Gu, G. D. Janaki Ram, T. Starr, and B. Stucker, "Influence of defects on mechanical properties of Ti-6Al-4V components produced by selective laser melting and electron beam melting," *Mater Des*, vol. 86, pp. 545–554, 2015, doi: 10.1016/j.matdes.2015.07.147.

[48] B. Mehta, L. Nyborg, K. Frisk, and E. Hryha, "Al–Mn–Cr–Zr-based alloys tailored for powder bed fusion-laser beam process: Alloy design, printability, resulting microstructure and alloy properties," *J Mater Res*, vol. 3, pp. 1–13, 2022, doi: 10.1557/s43578-022-00533-1.

[49] A. A. Martin *et al.*, "Ultrafast dynamics of laser-metal interactions in additive manufacturing alloys captured by in situ X-ray imaging," *Mater Today Adv*, vol. 1, p. 100002, 2019, doi: 10.1016/j.mtadv.2019.01.001.

[50] A. du Plessis and S. Beretta, "Killer notches: The effect of as-built surface roughness on fatigue failure in AlSi10Mg produced by laser powder bed fusion," *Addit Manuf*, vol. 35, Oct. 2020, doi: 10.1016/j.addma.2020.101424.

[51] A. Sola and A. Nouri, "Microstructural porosity in additive manufacturing: The formation and detection of pores in metal parts fabricated by powder bed fusion," *J Adv Manuf Process*, vol. 1, no. 3, pp. 1–21, 2019, doi: 10.1002/amp2.10021.

[52] O. Poncelet *et al.*, "Critical assessment of the impact of process parameters on vertical roughness and hardness of thin walls of AlSi10Mg processed by laser powder bed fusion," *Addit Manuf*, vol. 38, Feb. 2021, doi: 10.1016/j.addma.2020.101801.

[53] S. Kou, "A criterion for cracking during solidification," *Acta Mater*, vol. 88, pp. 366–374, 2015, doi: 10.1016/j.actamat.2015.01.034.

[54] J. H. Martin, B. D. Yahata, J. M. Hundley, J. A. Mayer, T. A. Schaedler, and T. M. Pollock, "3D printing of high-strength aluminium alloys," *Nature*, vol. 549, no. 7672, pp. 365–369, 2017, doi: 10.1038/nature23894.

[55] E. Scheil, "Bemerkungen zur schichtkristallbildung," *Zeitschrift für Metallkunde*, 1942.

[56] P. J. Withers and H. K. D. H. Bhadeshia, "Residual stress part 2 - Nature and origins," *Materials Science and Technology*, vol. 17, no. 4, pp. 366–375, 2001, doi: 10.1179/026708301101510087.

[57] J. L. Bartlett and X. Li, "An overview of residual stresses in metal powder bed fusion," *Addit Manuf*, vol. 27, no. February, pp. 131–149, 2019, doi: 10.1016/j.addma.2019.02.020.

[58] P. Mercelis and J. P. Kruth, "Residual stresses in selective laser sintering and selective laser melting," *Rapid Prototyp J*, vol. 12, no. 5, pp. 254–265, 2006, doi: 10.1108/13552540610707013.

[59] D. G. Rogich and G. R. Matos, "The Global Flows of Metals and Minerals," 2008. Accessed: Aug. 01, 2022. [Online]. Available: https://pubs.usgs.gov/of/2008/1355/

[60] J. G. Kaufman, "Properties and Applications of Wrought Aluminum Alloys," *Properties and Selection of Aluminum Alloys*, vol. 2, no. Table 2, pp. 202–275, 2019, doi: 10.31399/asm.hb.v02b.a0006543.

[61] J. G. Kaufman, "Properties and Selection of Cast Aluminum Alloys," *Properties and Selection of Aluminum Alloys*, vol. 2, no. Ref 2, pp. 465–506, 2019, doi: 10.31399/asm.hb.v02b.a0006548.

[62] J. R. Davis, Ed., "Light Metals and Alloys," *Alloying: Understanding the Basics*. ASM International, p. 0, Dec. 01, 2001.

[63] J. T. Al-haidary, N. J. Petch, and E. R. de los Rios, "The plastic deformation of polycrystals I. Aluminium between room temperature and 400°C," *Philosophical Magazine A: Physics of Condensed Matter, Structure, Defects and Mechanical Properties*, vol. 47, no. 6, pp. 869–890, 1983, doi: 10.1080/01418618308243126.

[64] Z. C. Cordero, B. E. Knight, and C. A. Schuh, "Six decades of the Hall–Petch effect – a survey of grain-size strengthening studies on pure metals," *International Materials Reviews*, vol. 61, no. 8, pp. 495–512, 2016, doi: 10.1080/09506608.2016.1191808.

[65] R. L. Fleischer, "Substitutional solution hardening," *Acta Metallurgica*, vol. 11, no. 3, pp. 203–209, 1963, doi: 10.1016/0001-6160(63)90213-X.

[66] R. Labusch, "A Statistical Theory of Solid Solution Hardening," *Physica Status Solidi (B)*, vol. 41, no. 2, pp. 659–669, 1970, doi: 10.1002/pssb.19700410221.

[67] T. Uesugi and K. Higashi, "First-principles studies on lattice constants and local lattice distortions in solid solution aluminum alloys," *Comput Mater Sci*, vol. 67, pp. 1–10, 2013, doi: 10.1016/j.commatsci.2012.08.037.

[68] M. A. Meyers and K. K. Chawla, *Mechanical Behavior of Materials*. Cambridge University Press, 2008. doi: 10.1017/CBO9780511810947.

[69] H. J. Frost and M. F. Ashby, *Deformation-mechanism Maps: The Plasticity and Creep of Metals and Ceramics*. Franklin Book Company, Incorporated, 1982. [Online]. Available: https://books.google.se/books?id=s9BRAAAAMAAJ

[70] E. O. Hall, "The Deformation and Ageing of Mild Steel: III Discussion of Results," *Proceedings of the Physical Society. Section B*, vol. 64, no. 9, pp. 747–753, Sep. 1951, doi: 10.1088/0370-1301/64/9/303.
[71] N. J. Petch, "The cleavage strength of polycrystals," *J.Iron Steel Inst.*, vol. 174, pp. 25–28, 1953.
[72] Michael F. Ashby, *Materials selection in mechanical design*. 2005.
[73] R. F. Decker, "Alloy Design, Using Second Phases.," *Metall Trans*, vol. 4, no. 11, pp. 2495–2518, 1973, doi: 10.1007/BF02644252.
[74] E. Nembach, "Order strengthening: recent developments, with special reference to aluminium-lithium-alloys," *Prog Mater Sci*, vol. 45, no. 4, pp. 275–338, 2000, doi: 10.1016/S0079-6425(99)00009-2.
[75] P. H. L. Souza, C. A. S. de Oliveira, and J. M. do V. Quaresma, "Precipitation hardening in dilute Al–Zr alloys," *Journal of Materials Research and Technology*, vol. 7, no. 1, pp. 66–72, 2018, doi: 10.1016/j.jmrt.2017.05.006.
[76] K. E. Knipling, D. N. Seidman, and D. C. Dunand, "Ambient- and high-temperature mechanical properties of isochronally aged Al-0.06Sc, Al-0.06Zr and Al-0.06Sc-0.06Zr (at.%) alloys," *Acta Mater*, vol. 59, no. 3, pp. 943–954, 2011, doi: 10.1016/j.actamat.2010.10.017.
[77] W. Lefebvre, N. Masquelier, J. Houard, R. Patte, and H. Zapolsky, "Tracking the path of dislocations across ordered Al3Zr nano-precipitates in three dimensions," *Scr Mater*, vol. 70, no. 1, pp. 43–46, 2014, doi: 10.1016/j.scriptamat.2013.09.014.
[78] A. J. Ardell, "Precipitation hardening," *Metallurgical Transactions A*, vol. 16, no. 12, pp. 2131–2165, 1985, doi: 10.1007/BF02670416.
[79] E. Nembach, "Precipitation hardening caused by a difference in shear modulus between particle and matrix," *Physica Status Solidi (a)*, vol. 78, no. 2, pp. 571–581, 1983, doi: 10.1002/pssa.2210780223.
[80] D. N. Seidman, E. A. Marquis, and D. C. Dunand, "Precipitation strengthening at ambient and elevated temperatures of heat-treatable Al(Sc) alloys," *Acta Mater*, vol. 50, no. 16, pp. 4021–4035, 2002, doi: 10.1016/S1359-6454(02)00201-X.
[81] E. P. George, J. A. Horton, W. D. Porter, and J. H. Schneibel, "Brittle cleavage of L1 2 trialuminides," *J Mater Res*, vol. 5, no. 8, pp. 1639–1648, Aug. 1990, doi: 10.1557/JMR.1990.1639.
[82] G. Bergerhoff, I. D. Brown, and F. Allen, "Crystallographic data bases," *International Union of Crystallography*, vol. 360, pp. 77–95, 1987.
[83] K. E. Knipling, D. C. Dunand, and D. N. Seidman, "Precipitation evolution in Al-Zr and Al-Zr-Ti alloys during isothermal aging at 375-425 °C," *Acta Mater*, vol. 56, no. 1, pp. 114–127, 2008, doi: 10.1016/j.actamat.2007.09.004.
[84] K. E. Knipling, D. C. Dunand, and D. N. Seidman, "Precipitation evolution in Al-Zr and Al-Zr-Ti alloys during aging at 450-600 °C," *Acta Mater*, vol. 56, no. 6, pp. 1182–1195, 2008, doi: 10.1016/j.actamat.2007.11.011.
[85] J. M. Silcock, T. J. Heal, and H. K. Hardy, "STRUCTURAL AGEING CHARACTERISTICS OF BINARY ALUMINIUM-COPPER ALLOYS," vol. Vol: 82, 1954, [Online]. Available: https://www.osti.gov/biblio/4400209
[86] M. F. Ashby, "The deformation of plastically non-homogeneous materials," *Philosophical Magazine*, vol. 21, no. 170, pp. 399–424, 1970, doi: 10.1080/14786437008238426.
[87] M. J. Starink, A. Deschamps, and S. C. Wang, "The strength of friction stir welded and friction stir processed aluminium alloys," *Scr Mater*, vol. 58, no. 5, pp. 377–382, 2008, doi: 10.1016/j.scriptamat.2007.09.061.
[88] G. Wang *et al.*, "The origin of high-density dislocations in additively manufactured metals," *Mater Res Lett*, vol. 8, no. 8, pp. 283–290, 2020, doi: 10.1080/21663831.2020.1751739.

[89] D. Riabov, A. Leicht, J. Ahlström, and E. Hryha, "Investigation of the strengthening mechanism in 316L stainless steel produced with laser powder bed fusion," *Materials Science and Engineering A*, vol. 822, no. May, 2021, doi: 10.1016/j.msea.2021.141699.

[90] X. X. Zhang *et al.*, "Quantifying internal strains, stresses, and dislocation density in additively manufactured AlSi10Mg during loading-unloading-reloading deformation," *Mater Des*, vol. 198, pp. 1–9, 2021, doi: 10.1016/j.matdes.2020.109339.

[91] F. Roters, D. Raabe, and G. Gottstein, "Work Hardening In Heterogeneous Alloys—A Microstructural Approach Based on Three Internal State Variables," *Acta Mater*, vol. 48, pp. 4181–4189, 2000.

[92] J. L. Cann *et al.*, "Sustainability through alloy design: Challenges and opportunities," *Prog Mater Sci*, vol. 117, no. July 2020, p. 100722, 2021, doi: 10.1016/j.pmatsci.2020.100722.

[93] L. Thijs, K. Kempen, J. P. Kruth, and J. Van Humbeeck, "Fine-structured aluminium products with controllable texture by selective laser melting of pre-alloyed AlSi10Mg powder," *Acta Mater*, vol. 61, no. 5, pp. 1809–1819, 2013, doi: 10.1016/j.actamat.2012.11.052.

[94] L. Kaufman and H. Bernstein, *Computer calculation of phase diagrams With special reference to refractory metals*. United States: Academic Press Inc, 1970. [Online]. Available: http://inis.iaea.org/search/search.aspx?orig_q=RN:02004171

[95] P. J. Spencer, "A brief history of CALPHAD," *CALPHAD*, vol. 32, no. 1, pp. 1–8, 2008, doi: 10.1016/j.calphad.2007.10.001.

[96] Thermo-Calc, "Precipitation Module (TC-PRISMA) User Guide," pp. 1–158, 2020, [Online]. Available: www.thermocalc.com

[97] S. Thapliyal *et al.*, "An integrated computational materials engineering-anchored closed-loop method for design of aluminum alloys for additive manufacturing," *Materialia (Oxf)*, vol. 9, no. December 2019, p. 100574, 2020, doi: 10.1016/j.mtla.2019.100574.

[98] A. Dreano, J. Favre, C. Desrayaud, P. Chanin-Lambert, A. Wimmer, and M. F. Zaeh, "Computational design of a crack-free aluminum alloy for additive manufacturing," *Addit Manuf*, vol. 55, Jul. 2022, doi: 10.1016/j.addma.2022.102876.

[99] N. Moelans, A. Miroux, E. Anselmino, S. Van Der Zwaag, B. Blanpain, and P. Wollants, "Phase-field simulations of coarsening of Al6Mn precipitates located on grain boundaries in AL alloys," *TMS Annual Meeting*, pp. 303–310, 2009.

[100] H. L. Chen, Q. Chen, and A. Engström, "Development and applications of the TCAL aluminum alloy database," *CALPHAD*, vol. 62, no. February, pp. 154–171, 2018, doi: 10.1016/j.calphad.2018.05.010.

[101] J. Allison, D. Backman, and L. Christodoulou, "Integrated computational materials engineering: A new paradigm for the global materials profession," *Jom*, vol. 58, no. 11, pp. 25–27, 2006, doi: 10.1007/s11837-006-0223-5.

[102] D. Riabov, *Laser-based powder bed fusion of stainless steels*. 2022.

[103] D. Riabov, L. Cordova, E. Hryha, and S. Bengtsson, "Effect of powder variability on laser powder bed fusion processing and properties of 316L," *European Journal of Materials*, vol. 2, no. 1, pp. 202–221, 2022, doi: 10.1080/26889277.2022.2064772.

[104] R. Tamura *et al.*, "Machine learning-driven optimization in powder manufacturing of Ni-Co based superalloy," *Mater Des*, vol. 198, p. 109290, 2021, doi: 10.1016/j.matdes.2020.109290.

[105] A. Ünal, "Effect of processing variables on particle size in gas atomization of rapidly solidified aluminium powders," *Materials Science and Technology (United Kingdom)*, vol. 3, no. 12, pp. 1029–1039, 1987, doi: 10.1179/mst.1987.3.12.1029.

[106] J. A. Slotwinski, E. J. Garboczi, P. E. Stutzman, C. F. Ferraris, S. S. Watson, and M. A. Peltz, "Characterization of metal powders used for additive manufacturing," *J Res Natl Inst Stand Technol*, vol. 119, pp. 460–493, 2014, doi: 10.6028/jres.119.018.

[107] A. Strondl, O. Lyckfeldt, H. Brodin, and U. Ackelid, "Characterization and Control of Powder Properties for Additive Manufacturing," *JOM*, vol. 67, no. 3, pp. 549–554, 2015, doi: 10.1007/s11837-015-1304-0.
[108] A. ÜNal, "Production of rapidly solidified aluminium alloy powders by gas atomisation and their applications," *Powder Metallurgy*, vol. 33, no. 1, pp. 53–64, 1990, doi: 10.1179/pom.1990.33.1.53.
[109] E. J. Lavernia, J. D. Ayers, and T. S. Srivatsan, "Rapid solidification processing with specific application to aluminium alloys," *International Materials Reviews*, vol. 37, no. 1, pp. 1–44, 1992, doi: 10.1179/imr.1992.37.1.1.
[110] H. Jones, "Chapter 3 Rapid solidification," *Pergamon Materials Series*, vol. 2, no. C, pp. 23–45, 1999, doi: 10.1016/S1470-1804(99)80049-2.
[111] T. Pinomaa, A. Laukkanen, and N. Provatas, "Solute trapping in rapid solidification," *MRS Bull*, vol. 45, no. 11, pp. 910–915, 2020, doi: 10.1557/mrs.2020.274.
[112] S. J. Griffiths, "Seth James GRIFFITHS," 2020.
[113] M. Buttard *et al.*, "Evidence that the liquid structure affects the nucleation of the primary metastable L12-Al3Zr in additive manufacturing," *Scr Mater*, vol. 226, no. November 2022, 2023, doi: 10.1016/j.scriptamat.2022.115212.
[114] H. H. König *et al.*, "Solidification modes during additive manufacturing of steel revealed by high-speed X-ray diffraction," *Acta Mater*, vol. 246, no. June 2022, 2023, doi: 10.1016/j.actamat.2023.118713.
[115] P. Liu and G. L. Dunlop, "Microstructural characterization of rapidly solidified Al-Mn-Cr alloys," *Materials Science and Engineering A*, vol. 134, no. 25, pp. 1182–1187, 1991, doi: 10.1007/BF02647021.
[116] P. Liu, G. L. Dunlop, and L. Arnberg, "Microstructural development in a rapidly solidified Al5Mn2.5Cr alloy," *Materials Science and Engineering*, vol. 98, no. C, pp. 437–441, 1988, doi: 10.1016/0025-5416(88)90202-9.
[117] H. Jones, "Development in aluminium alloys by solidification at higher cooling rates," Sheffield, UK, 1978.
[118] Y. Du *et al.*, "Diffusion coefficients of some solutes in fcc and liquid Al: Critical evaluation and correlation," *Materials Science and Engineering A*, 2003, doi: 10.1016/S0921-5093(03)00624-5.
[119] K. E. Knipling, D. C. Dunand, and D. N. Seidman, "Criteria for developing castable, creep-resistant aluminum-based alloys - A review," *International Journal of Materials Research*, vol. 97, no. 3, pp. 246–265, 2006.
[120] N. A. Belov, D. G. Eskin, and A. A. Aksenov, "Alloys with Transition Metals," *Multicomponent Phase Diagrams*, pp. 287–340, 2005, doi: 10.1016/b978-008044537-3/50009-3.
[121] B. Mehta *et al.*, "Microstructure, mechanical properties and fracture mechanisms in a 7017 aluminium alloy tailored for powder bed fusion – laser beam," *Mater Des*, vol. 226, p. 111602, 2023, doi: 10.1016/j.matdes.2023.111602.
[122] T. H. E. Major and A. Alloy, "Heat Treatment Practices of Age-Hardenable Aluminum Alloys *," vol. 4, no. c, 2016, doi: 10.31399/asm.hb.v04e.a0006288.
[123] B. Mehta, K. Frisk, and L. Nyborg, "Advancing Novel Al-Mn-Cr-Zr Based Family of Alloys Tailored for Powder Bed Fusion-Laser Beam Process," *J Alloys Compd*, vol. 967, p. 171685, Aug. 2023, doi: 10.1016/j.jallcom.2023.171685.
[124] B. Mehta, A. Svanberg, and L. Nyborg, "Laser powder bed fusion of an al-mg-sc-zr alloy: Manufacturing, peak hardening response and thermal stability at peak hardness," *Metals (Basel)*, vol. 12, no. 1, 2022, doi: 10.3390/met12010057.

[125] A. Svanberg, “Structure-, Properties- Performance- correlation in Aluminium Alloy Design Tailored for Additive Manufacturing,” 2021.
[126] B. Mehta, K. Frisk, and L. Nyborg, “Effect of Precipitation Kinetics on Microstructure and Properties of Novel Al-Mn-Cr-Zr Based Alloys Developed for Powder Bed Fusion – Laser Beam Process,” *J Alloys Compd*, 2022, [Online]. Available: https://doi.org/10.1016/j.jallcom.2022.165870
[127] K. A. Unocic, M. J. Mills, and G. S. Daehn, “Effect of gallium focused ion beam milling on preparation of aluminium thin foils,” *J Microsc*, vol. 240, no. 3, pp. 227–238, 2010, doi: 10.1111/j.1365-2818.2010.03401.x.
[128] Y. Xiao, V. Maier-Kiener, J. Michler, R. Spolenak, and J. M. Wheeler, “Deformation behavior of aluminum pillars produced by Xe and Ga focused ion beams: Insights from strain rate jump tests,” *Mater Des*, vol. 181, p. 107914, 2019, doi: 10.1016/j.matdes.2019.107914.
[129] I. Ansara, A. T. Dinsdale, and M. H. Rand, *Thermochemical database for light metal alloys*, vol. 2. 1998.
[130] K. D. Vernon-Parry, “Scanning electron microscopy: an introduction,” *III-Vs Review*, vol. 13, no. 4, pp. 40–44, Jul. 2000, doi: 10.1016/S0961-1290(00)80006-X.
[131] E. J. Payton and G. Nolze, “The backscatter electron signal as an additional tool for phase segmentation in electron backscatter diffraction,” *Microscopy and Microanalysis*, vol. 19, no. 4, pp. 929–941, 2013, doi: 10.1017/S1431927613000305.
[132] D. Stojakovic, “Electron backscatter diffraction in materials characterization,” *Processing and Application of Ceramics*, vol. 6, no. 1, pp. 1–13, 2012, doi: 10.2298/pac1201001s.
[133] T. Manninen *et al.*, *Electron Backscatter Diffraction in Materials Science*, vol. 86, no. 1. Boston, MA: Springer US, 2009. doi: 10.1007/978-0-387-88136-2.
[134] Y. P. Hong *et al.*, “Alignment of low-dose X-ray fluorescence tomography images using differential phase contrast,” *J Synchrotron Radiat*, vol. 21, no. 1, pp. 229–234, 2014, doi: 10.1107/S1600577513029512.
[135] P. Detector, “Rococo detector,” 2023. https://pndetector.de/products-applications/multi-cell-sdds/ (accessed Jul. 11, 2023).
[136] S. Vogt and M. Ralle, “Opportunities in multidimensional trace metal imaging: Taking copper-associated disease research to the next level,” *Anal Bioanal Chem*, vol. 405, no. 6, pp. 1809–1820, 2013, doi: 10.1007/s00216-012-6437-1.
[137] Y. Fam *et al.*, “A versatile nanoreactor for complementary in situ X-ray and electron microscopy studies in catalysis and materials science,” *J Synchrotron Radiat*, vol. 26, pp. 1769–1781, 2019, doi: 10.1107/S160057751900660X.
[138] H. Markötter, M. Sintschuk, R. Britzke, S. Dayani, and G. Bruno, “Upgraded imaging capabilities at the BAMline (BESSY II),” *J Synchrotron Radiat*, vol. 29, no. 5, pp. 1292–1298, Sep. 2022, doi: 10.1107/S1600577522007342.
[139] Radbound University, “ICP-OES.” https://www.ru.nl/science/gi/facilities-activities/elemental-analysis/icp-oes/ (accessed Jun. 20, 2023).
[140] ASTM E384-17, “Standard Test Method for Microindentation Hardness of Materials,” *ASTM International*, vol. E384, pp. 1–40, 2017, doi: 10.1520/E0384-17.
[141] ASTM E8, “ASTM E8/E8M standard test methods for tension testing of metallic materials 1,” *Annual Book of ASTM Standards 4*, no. C, pp. 1–27, 2010, doi: 10.1520/E0008.
[142] K. Frisk, S. Bengtsson, L. Nyborg, and B. Mehta, “New powder, method for additive manufacturing of components made from the new powder and article made therefrom,” WO2022122670A1 [Online]. Available: https://patents.google.com/patent/WO2022122670A1/en?inventor=karin+frisk&oq=karin+frisk

[143] T. Ohashi, L. Dai, and N. Fukatsu, “DECOMPOSITION CHARACTERISTICS OF Al-Mn-Zr ALLOYS RAPIDLY-QUENCHED FROM THE MELT.,” *Metallurgical transactions. A, Physical metallurgy and materials science*, vol. 17, no. 5, pp. 799–806, 1986, doi: 10.1007/BF02643855.

[144] L. Deillon, F. Jensch, F. Palm, and M. Bambach, “A new high strength Al–Mg–Sc alloy for laser powder bed fusion with calcium addition to effectively prevent magnesium evaporation,” *J Mater Process Technol*, vol. 300, p. 117416, 2022, doi: 10.1016/j.jmatprotec.2021.117416.

[145] K. Schmidtke, F. Palm, A. Hawkins, and C. Emmelmann, “Process and mechanical properties: Applicability of a scandium modified Al-alloy for laser additive manufacturing,” in *Physics Procedia*, 2011. doi: 10.1016/j.phpro.2011.03.047.

[146] Q. Jia *et al.*, “Selective laser melting of a high strength Al[sbnd]Mn[sbnd]Sc alloy: Alloy design and strengthening mechanisms,” *Acta Mater*, vol. 171, pp. 108–118, Jun. 2019, doi: 10.1016/j.actamat.2019.04.014.

[147] A. Martucci, B. Mehta, M. Lombardi, and L. Nyborg, “The Influence of Processing Parameters on the Al-Mn Enriched Nano-Precipitates Formation in a Novel Al-Mn-Cr-Zr Alloy Tailored for Power Bed Fusion-Laser Beam Process,” *Metals (Basel)*, vol. 12, no. 8, 2022, doi: 10.3390/met12081387.

[148] S. Cui and I. H. Jung, “Thermodynamic Modeling of the Al-Cr-Mn Ternary System,” *Metall Mater Trans A Phys Metall Mater Sci*, vol. 48, no. 3, pp. 1383–1401, 2017, doi: 10.1007/s11661-016-3894-8.

[149] B. Grushko, W. Kowalski, D. Pavlyuchkov, S. Balanetskyy, and M. Surowiec, “On the constitution of the Al-rich part of the Al-Cr-Mn system,” *J Alloys Compd*, vol. 468, no. 1–2, pp. 87–95, 2009, doi: 10.1016/j.jallcom.2007.12.069.

[150] S. Bengtsson, B. Mehta, K. Frisk, and L. Nyborg, “New Aluminium Alloy Tailored For Powder Bed Fusion – Laser Beam Process,” *WorldPM 2022 Congress & Exhibition : Conference Proceedings*, 2022.

[151] B. Mehta, K. Frisk, L. Nyborg, S. Bengtsson, and E. Hryha, “Thermal Stability In Al-Mn-Cr-Zr Based Aluminium Alloys Tailored For Powder Bed Fusion – Laser Beam,” *WorldPM 2022 Congress & Exhibition : Conference Proceedings*, 2022.

[152] J. G. Kaufman, “Fatigue of Aluminum Alloys,” *Properties and Selection of Aluminum Alloys*, vol. 2, pp. 52–78, 2019, doi: 10.31399/asm.hb.v02b.a0006549.

[153] A. B. Spierings, K. Dawson, K. Kern, F. Palm, and K. Wegener, “SLM-processed Sc- and Zr-modified Al-Mg alloy: Mechanical properties and microstructural effects of heat treatment,” *Materials Science and Engineering A*, vol. 701, no. June, pp. 264–273, 2017, doi: 10.1016/j.msea.2017.06.089.